Characterization and Modeling of H^- Primary Stripper Foils for the Spallation Neutron Source

A Dissertation Presented for the
Doctor of Philosophy
Degree
The University of Tennessee, Knoxville

Leo Vernon Saturday III
May 2022

Copyright © 2022 by Leo Vernon Saturday III.
All rights reserved.

ACKNOWLEDGEMENTS

I would like to acknowledge my advisor, Philip Rack, for his help and guidance during this work. Additionally I would also like to acknowledge my mentors at SNS, Nicholas Evans, and CNMS, Nickolay Lavrik, for the time and guidance they have invested in me. I would not have been able to complete this work without the expertise of my advisor and mentors. Special thanks go out to Chris Luck for his help with the Foil Test Stand and Leslie Wilson for her assistance with foil fabrication. Lastly, I would like to thank my family for their continued support throughout this endeavor.

ABSTRACT

The Spallation Neutron Source (SNS) is currently preparing for a Proton Power Upgrade project that will increase the operating power of the beamline. Due to this increase in power, a major concern is whether the current stripper foils will be able to withstand the higher power beam. Here, we analyze the current nanocrystalline diamond as well as microcrystalline diamond stripper foils in order to assess their ability to withstand the higher power beamline. In this work we assess the samples' room temperature thermal conductivity, as well as other material constants, develop a method for in situ analysis of stripper foil failure, and compare the micro and nanocrystalline diamond samples for their viability in the SNS beamline. In the first chapter the mechanical properties of the samples are assessed. Bilayer cantilever are manufactured and photothermally excited to obtain excitation and relaxation curves due to induced deformation. The relaxation curves are fit to COMSOL simulations and the room temperature thermal conductivity is determined. The second chapter outlines the foil test stand electron beam mimic. This consists of testing the nanocrystalline diamond sample by irradiating spots with a 30 keV electron beam. Correlations are found between foil failure and measurements taken in the foil test stand. Lastly, the third chapter overviews the comparison between the micro and nanocrystalline diamond samples in the foil test stand. Both samples are irradiated using the same beam parameters and assessed to determine relative thermal robustness of the samples.

TABLE OF CONTENTS

INTRODUCTION 1
Motivation 1
1.1 Spallation Neutron Source (SNS) 2
1.2 Proton Power Upgrade 3
1.3 Stripper Foils 6
1.4 NCD Foil Fabrication 7
1.4.1 CVD Growth 8
1.4.2 Substrate Effects 9
1.4.3 Gas Composition 10
1.4 Previous Work on NCD Foils 13
1.4.1 NCD Emissivity 15
1.4.2 Raman Spectra of PD 15
1.4.3 Thermal Studies of NCD 20
1.4.4 NCD Simulation 26
CHAPTER I Thermal Conductivity of Nano- and Micro-Crystalline Diamond Films Studied by Photothermal Excitation of Cantilever Structures 30
Author's Contribution 31
Abstract 31
Introduction 32
Experimental 34
MPCVD growth of polycrystalline diamond films 34
Fabrication of microcantilevers 36
Raman microscopy and SEM characterization 38
Thermal conductivity measurements 38
Finite element analysis (COMSOL modeling) 41
Results and Discussion 45
Conclusions 53
Acknowledgements 53
CHAPTER II Experimental and simulated heating in nanocrystalline diamond charge exchange injection films using an electron beam to mimic SNS conditions 55
Author's Contribution 56
Abstract 56
Introduction 57
Methods 59
FTS Hardware 60
FTS Measurements 62
SNS Equivalent Current 63
Post Mortem Testing 64
Simulation 65
Results and Discussion 67
Conclusion 81

Acknowledgements 82
Supplemental 82
CHAPTER III Comparison of μCD and NCD stripper Foils 87
Abstract 88
Introduction 88
Methods 90
Measurements 95
Simulation 96
Results and Discussion 97
Conclusion 120
Acknowledgements 121
REFERENCES 122
CONCLUSION 131
VITA 134

LIST OF TABLES

Table 1: COMSOL model input and output parameters. The parameters with an asterisk have been experimentally calculated or measured. The parameters without an asterisk were pulled from literature. 44
Table 2: Sensitivity analysis for COMSOL simulation parameters 80
Table 3: MPCVD growth conditions for the various samples. 91

LIST OF FIGURES

Figure 1: Schematic showing the interactions at the injection region of the SNS beamline presented in [1]. 4
Figure 2: SNS standard primary stripper foil. Photo courtesy of Chris Luck. 5
Figure 3: The diamond film growth process from a CH_4/H_2 gas mixture presented in [29]. Step 1 shows disassociated H creating a reactive site on the substrate surface where a CH_3 can bond in step 2. This process repeats in steps 3 and 4 for a neighboring site. An H atom strikes a CH_3 in step 5 turning it into a reactive CH_2 as shown in step 6. Step 7 shows the neighboring CH_2 and CH_3 forming a C-C bond which completes the ring structure.....12
Figure 4: Plan view SEM images of MPCVD grown diamond films with various Ar percentages presented in [20]. The CH_4 was kept at 1% of the total pressure while the percentage of Ar is shown in each picture with H_2 making up the rest of the 99%.....14
Figure 5: The temperature and emissivity of a NCD foil under increasing electron beam current density presented in [35]. SNS equivalent power is also associated with current density.....16
Figure 6: The pre and post electron beam exposure Raman spectra presented in [35] using both 514 nm (a) and 257 nm (b) light. The blue curve in both plots shows the spectra before exposure while the red curve shows the foil post electron beam exposure. 18
Figure 7: Fracture strength vs. annealing temperature of samples presented in [37]. #86 is a 488 µm thick sample while #88 is 274 µm thick. The NS denotes the measurement being taken on the nucleation side of the film while GS denotes the measurement being taken on the growth side. 19
Figure 8: a) The direction of the cut and placement of resistive heaters presented in [11]. b) The thermal conductivity as a function of cut length (orientation shown in part a) and corresponding grain sizes and SEM presented in [11]. c) The thermal conductivity and grain size relationship plotted from multiple sources presented in [40]. 21
Figure 9: Thermal conductivity's relation to grain size as presented in [18]. The dotted lines show the simulated curves given the stated grain boundary conductance. 24
Figure 10: In plane thermal conductivity of polycrystalline diamond vs. temperature made with H/CH_4 gas compositions presented in [44]. b) In plane thermal conductivity of µCD (poly), undoped NCD (NCD_0), and N doped NCD (NCD_25) vs. temperature presented in [45]. c) Thermal conductivity vs. temperature of as-indicated hydrogen impurity measured in ppm presented in [43]. d) Thermal conductivity as a function of annealing temperature presented in [37].....25
Figure 11: The thermal simulation results for Liaw et al. using a simplified and complex model presented in [48].....28

Figure 12: Schematic of the MWPECVD tool used in the present study. 35
Figure 13: Wafer level processing sequence used to fabricate microcantilevers using PD films as a structural material. 37
Figure 14: Setup for photothermal excitation and optical readout of the microcantilevers fabricated in the present study. 40
Figure 15: SEM of µCD (set a) and NCD (set b) film. Accompanying Raman spectra of µCD (c) and NCD (d) samples. 46
Figure 16: Transient deflection of bimaterial cantilevers measured in response to pulsed photothermal excitation. 48
Figure 17: Schematic representations of the µCD and NCD samples. 50
Figure 18: Figure 1. a) Photograph and b) schematic of the Foil Test Stand. Example outputs from the c) residual gas analyzer, d) FLIR camera and Faraday cup, e) Faraday cup and electron gun emission current. 61
Figure 19: Normalized Faraday cup current versus time demonstrating a steeper slope at higher emission current, which is indicative of a higher carbon sublimation rate. 68
Figure 20: a) Temperature and normalized Faraday cup current versus time for 3 different runs (left). b) Photograph of the foil after the 3 runs (right). 70
Figure 21: SEM image of an exposed spot (left) and the corresponding Raman spectra (right). Example of holes in the foil (boxed in yellow). 72
Figure 22: Temperature data for the 1.4 MW, 1.0 GeV SNS beam (black) and the 750 µA FTS electron beam (red). 74
Figure 23: A) 200 µA continuous electron beam experimental and simulated comparisons. Inset graph shows simulated heat profile on foil. B) 750 µA pulsed electron beam experimental and simulated data. C) 1 mA pulsed electron beam experimental and simulated data. 77
Figure 24: Supplemental: a) Specific Heat capacity function used in simulations. b) Thermal conductivity function used in simulations. 85
Figure 25:Supplemental: Simulated thermal decay of various size spots each fixed at the same peak temperature, but varying decay curves where larger areas decay more slowly. 86
Figure 26: Raman spectra for un-graphitized portions on the samples. 93
Figure 27: SEM images of the samples NCD (a), µCD-1 (b), µCD-2 (c), and µCD-3 (d). 94
Figure 28: The percent of emitted beam captured by the limiting aperture after penetrating a foil versus foil thickness. This simulation was conducted with G4 Beamline for a graphite material tilted at 30^{o}. 99
Figure 29: The NCD Faraday Cup (a) and temperature (b) measurements versus time for the 520, 690, and 870 µA exposed spots. 100
Figure 30: The µCD-1 Faraday Cup (a) and temperature (b) measurements versus time for the 520, 690, and 870 µA exposed spots. 102
Figure 31: The µCD-2 samples' Faraday Cup (a) and temperature (b) measurements versus time for the 520, 690, and 870 µA exposed spots. 104

Figure 32 : The µCD-3 samples' Faraday Cup (a) and temperature (b) measurements versus time for the 520, 690, and 870 µA exposed spots. 106
Figure 33 : Emissivity vs Temperature data for the various samples. 108
Figure 34: Raman spectra of the graphitized portions of each sample. 110
Figure 35: SEM images of the NCD sample's un-graphitized (a) and graphitized (b) regions.....111
Figure 36: SEM images of the µCD-1 sample's un-graphitized (a) and graphitized (b) regions.....112
Figure 37: SEM images of the µCD-2 sample's un-graphitized (a) and graphitized (b) regions.....113
Figure 38: SEM images of the µCD-3 sample's un-graphitized (a) and graphitized (b) regions.....114
Figure 39: Continuous wave 200 µA experimental and simulated curves for NCD (a) and µCD-1 (b).....117
Figure 40: NCD experimental and simulated temperature vs time for 520 µA (a) and 870 µA (b) electron beams. 118
Figure 41: µCD-1 experimental and simulated temperature vs time for 520 µA (a) and 870 µA (b) electron beams. 119

INTRODUCTION

Motivation

The motivation for this project comes from the Proton Power Upgrade project that is currently underway at Spallation Neutron Source. In this project, the beam power will be increased from 1.4 to 2.8 MW and approximately 10% more energy will be deposited into the stripper foil. There is concern about the current stripper foil being able to withstand the increased beam power without rapidly failing. The overall motivation of this research is to determine whether the current stripper foils will withstand the higher power beamline, and to assess an alternative foil for the purpose of increasing the foil's heat dissipation.

Carbon is the most common choice for stripper foils due to its desirable properties such as high sublimation point, low atomic number, and high thermal conductivity in many of its forms. The SNS foil is made of nanocrystalline diamond and has an improved mechanical stability when compared to amorphous carbon. In this research we also assess microcrystalline diamond. The microcrystalline foils should have similarly improved mechanical stability while increasing the grain size of the diamond and improving the thermal conductivity. This could lead to a longer lasting foil that will be useful at any beamline that utilizes charge exchange injection.

1.1 Spallation Neutron Source (SNS)

Materials discovery and analysis has become increasingly important in recent years with many areas, such as nuclear power production and semiconductor materials development, being reliant on material improvement for future advances. User facilities that provide resources for materials research are an integral part of the material exploration process. Spallation Neutron Source (SNS) is one of these user facilities and uses neutron scattering to examine differing material properties. It is the first megawatt class pulsed proton source and operates at 1.4 megawatts with a kinetic energy of 1.0 GeV. Information obtained from the SNS neutron scattering instruments is useful in many fields including materials science, biology, and physics.

The SNS is a complex facility that accelerates an H^- ion, converts it to a proton, strikes a liquid mercury target, and produces neutrons for neutron scattering. The injection region of the SNS beam line is where the H^- beam is transferred from the linear accelerator to the storage ring. The injected beam is pulsed at 60 Hz with a duty cycle of 6% and power of 1.4 MW with 1.0 GeV of kinetic energy. During injection the H^- beam strikes a stripper foil at 30^o from orthogonal. The purpose of the stripper foil is to separate the electrons from the proton in the H^- ions. This process can result in unstripped H^-, partially stripped H^0, and stripped H^+. The stripped electrons are collected in an electron collector while the protons continue into the storage ring. The remaining H^- and H^0 beams are then guided into the injection dump and constitute approximately 60 kW of

the injected beam. This process can be seen schematically in fig. 1[1]. This process where an ion interacts with a material and separates the electrons from the protons is called charge exchange injection (CEI). SNS uses a nanocrystalline diamond (NCD) foil with an areal density of approximately 400 $\mu g/cm^2$ for CEI. A photo of a standard SNS NCD stripper foil can be seen in fig. 2.

1.2 Proton Power Upgrade

The SNS is currently in the process of being upgraded under the Proton Power Upgrade (PPU) project. This project will increase the power in the beamline from 1.4 megawatts to 2.8 megawatts This project will enable SNS to stay at the leading edge of neutron science by allowing for a second target station as well as improving the performance of the current instruments[2]. Multiple changes will need to take place to the SNS facility during the PPU project, mainly adding additional cryomodules to the linear accelerator in order to accelerate the H^- beam from 1.0 GeV accelerating voltage to 1.3 GeV. To reach 2.8 MW beam power, the energy and current will be increased while the optics and pulse structure will remain unchanged. This will cause the power density the foil sees to go up. With the higher beam power, other considerations for the beamline need to be considered. One of these considerations is if the stripper foil will be able to withstand the higher beam power. In the current 1.4 megawatt setup the NCD foils do not fail due to sublimation. Currently mechanical failure is the main reason that a foil stops being used, however, with the increased beam

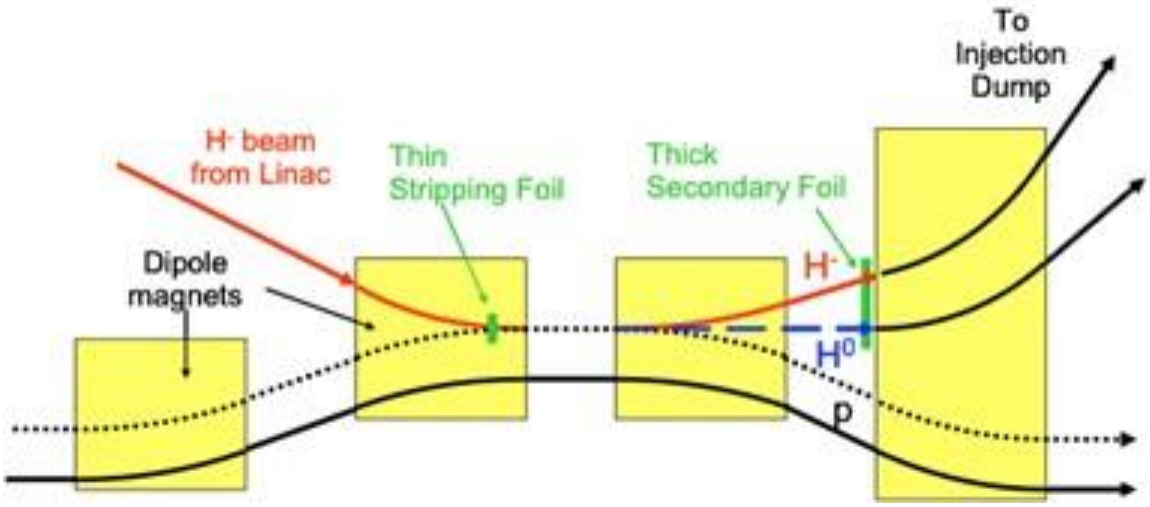


Figure 1: Schematic showing the interactions at the injection region of the SNS beamline presented in [1]**.**

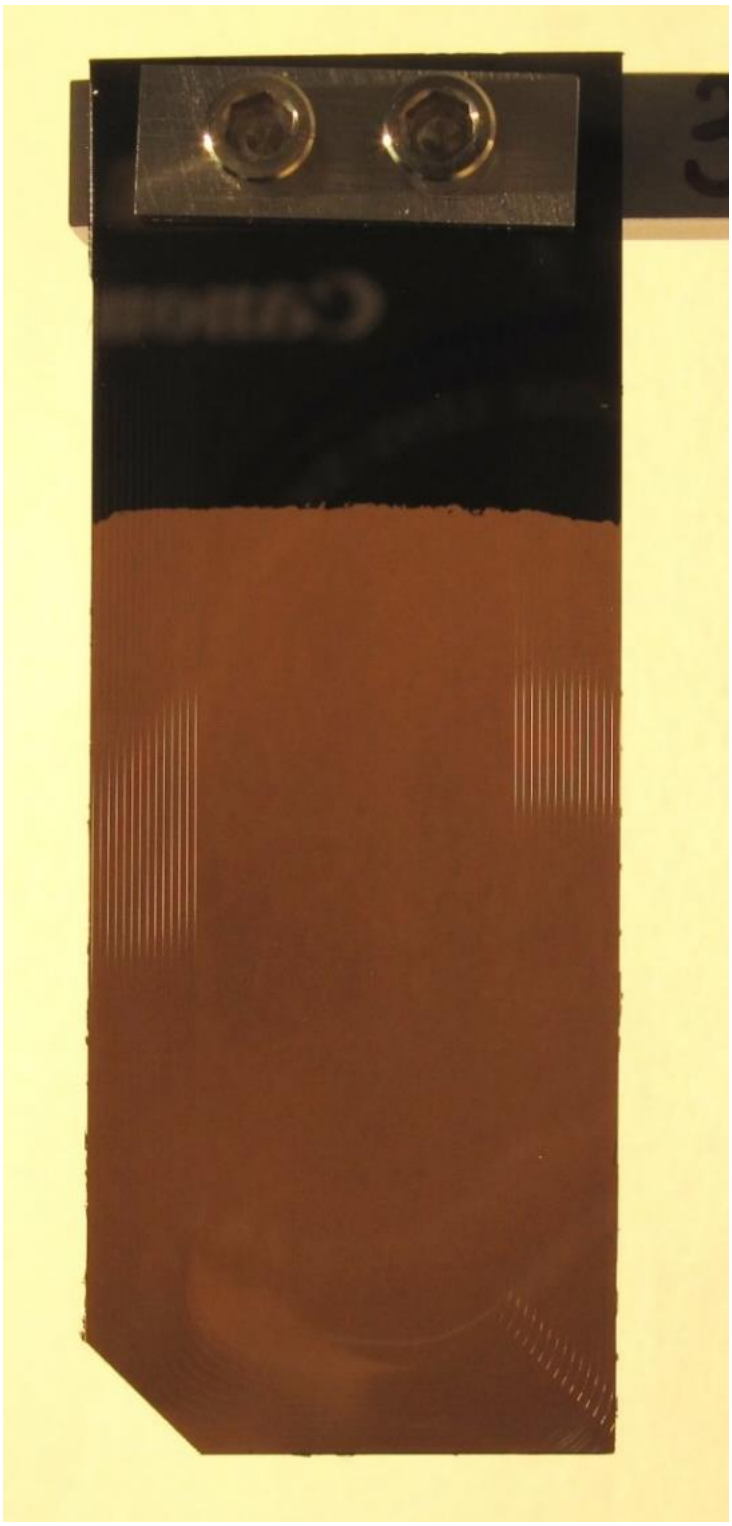


Figure 2: SNS standard primary stripper foil. Photo courtesy of Chris Luck.

power this could potentially change and sublimation might become a problem. If this is the case, an alternative to the NCD stripper foils would need to be implemented or larger changes to the beamline would need to occur.

1.3 Stripper Foils

When considering materials for stripper foils, one of the primary concerns is scattering. Scattering angles in stripper foils increase with both the atomic number of the element used and the thickness of the foil.[3] This makes lower atomic number elements more desirable for stripper foil purposes. The first material used as a stripper foil was a 500 nm thick polyparaxylene foil used by Argonne National Lab in 1969.[4] Additionally, aluminum oxide,[5] graphene,[6] and nanocrystalline diamond[7] have been used for CEI as well as He gas[8] and liquid Li[9]. A stripper foil alternative is laser stripping[10]; however, this technology is still in the R&D stage. Carbon type stripper foils are the most common for CEI purposes due to having a low atomic number, being safe to use, cheap to manufacture, and having a high melting and sublimation temperature.

Due to the high temperature that stripper foils experience, thermal properties of the foil are important. Diamond has a high thermal conductivity and low sublimation rates at high temperature, which are beneficial to stripper foils. The thermal conductivity is reduced in polycrystalline diamond (PD) form due to grain boundary scattering,[11] which diminishes the foil's ability to distribute heat. However, PD also shows heavy graphitization in the 1200 – 1400 ^{o}C range[12]

which increases the foil emissivity allowing increased heat radiation to the surrounding chamber walls. Additionally, the mechanical properties of PD make it much more robust as a thin film compared to some of the other materials, like graphite. The combination of heat dissipation properties and mechanical stability are important for stripper foils.

1.4 NCD Foil Fabrication

Over the past several decades polycrystalline and, in particular, nanocrystalline diamond (NCD) films[13] have drawn a great deal of attention due to their unique properties, such as high thermal conductivity and desirable mechanical properties, that are useful for applications in numerous areas including industrial tools, nano-magnetometry, and lubrication [14]. These fundamental properties of polycrystalline diamond thin films can be drastically different compared to macroscopic single crystal diamond samples, and are highly dependent upon the grain structure of the films. This is particularly true for nanocrystalline diamond that exhibit substantial optical absorption, low thermal conductivity and high density of defects, such as nitrogen vacancy (NV) centers.

The history of nanodiamond synthesis is traced back to 1963 when Volkov *et al.* discovered that detonation of carbon based materials yielded ultrafine dispersions of diamond crystals [15]. However, it was not until the 1980s, that low cost methods for growing polycrystalline films on cheap substrates became available [16]. Polycrystalline diamond films with grain sizes ranging from the micro- to nano-scale can be grown by various modifications of chemical vapor

deposition (CVD) techniques [17], in particular hot filament CVD [18] and microwave plasma assisted CVD (MPCVD) [19–22]. Other methods include high pressure high temperature (HPHT) and [23] detonation nanodiamond [24].

While there are other ways to facilitate CEI, such as the above mentioned laser and liquid Li methods, stripper foils are the most common method. In order to make the SNS standard NCD stripper foils, MPCVD is used for fabrication. The specific deposition method, growth parameters, and gas composition can all drastically alter the material parameters of the resultant growth.

1.4.1 CVD Growth

CVD diamond fabrication has the benefit of being able to conformally coat a surface, which neither HPHT nor detonation diamond are capable. In order for deposition to occur, a heating element is needed to disassociate hydrogen molecules. Varying heating elements lead to the different forms of CVD diamond growth: hot filament, arc jet, DC arc, and microwave plasma.[25] We will focus on MPCVD as it is the process used for SNS foils. The disassociated H atoms have multiple purposes in the CVD process including terminating dangling C bonds on the substrate surface, creating reactive radicals from the methane that bond to the surface creating sp^2 or sp^3 bonds, and preventing graphite growth by preferentially etching graphite.[26] The microwave plasma CVD (MPCVD) process usually involves flowing H_2 and CH_4 for nano to micro range diamond grains. Argon is introduced to the system when going from nanodiamond to ultrananocrystalline and creates C_2 dimers that act as the primary diamond

growth mechanism. Many factors in MPCVD have to be taken into account during film growth. The composition of the substrate, substrate pretreatment, gas composition, plasma temperature, plasma location, and pressure are all important factors that dictate the resultant film.

1.4.2 Substrate Effects

Substrate composition and pretreatment play an important role in MPCVD diamond growth and nucleation density.[27] For noticeable deposition to occur, there must be surface defects or dangling carbon bonds for the CH_4 radicals to bond with. This necessitates substrate pretreatment in the form of seeding or scratching, which is a critical process for the substrate before deposition can occur. Seeding is the process of sonicating a substrate in a suspension of roughly nm sized diamond particles. This abrades the surface of the substrate and allows the diamond particles to stick to the surface, creating initial nucleation points from both the diamond particle and the abrasions. Additionally, mechanical scratching with diamond pastes can also be used to create nucleation points.[28] Scratching and seeding both have a nucleation density of 10^6 to 10^{10} cm^{-2} while a nucleation density of 10^3 to 10^5 cm^{-2} can be expected for a substrate with no pretreatment.[29] While seeding and scratching aren't the only methods for substrate pretreatment, they are the most commonly used as well as the methods that have been used for the SNS foils.

The composition of the substrate also influences the growth mechanics of MPCVD diamond. Many different substrates have been used with varying

amounts of success; however, the most commonly used substrates are molybdenum, tungsten carbide, silicon nitride [26], and silicon [29]. Additionally, diamond, titanium, silicon, and materials with low carbon solubility can be used during MPCVD diamond growth.[25] The substrate's reactivity with carbon is very important due to carbon being needed for surface deposition. Additionally, the thermal expansion coefficient of the substrate is important. The expansion mismatch can cause stress in the film, which will influence it strength.[30] The substrate used in MPCVD of the ORNL SNS foils is Si as it is the most studied substrate material for diamond growth [29].

1.4.3 Gas Composition

Gas composition is a key influencer on grain size, grain boundaries, and diamond purity in MPCVD PD growth. Three gas combinations that are of particular interest are H_2/CH_4, Ar/ CH_4, and Ar/H_2/CH_4. Each of these gas combinations have slightly different growth mechanisms that dominate. This portion of the review will go into detail on each of these combinations and how the grain size changes depending on their relative gas ratios.

The H_2/CH_4 gas combination is able to vary the grain size from the micrometer to nanometer range by adjusting the H_2 concentration. As described previously, the growth in this combination is driven by the hydrocarbon radicals created by the interaction with the disassociated H atoms. This facilitates both sp^2 and sp^3 growth; however, the disassociated H preferentially etches the graphite at a rate of roughly 50 times the rate it etches diamond leading to

intergranular voids and poor surface morphology in microcrystalline films.[31] In this combination a CH_4 percentage of 1% results in microcrystalline diamond, while a nanocrystalline diamond, in the range of 10 – 100 nm, can be achieved by adjusting the CH_4 percentage up to 4%.[31] Figure 3 shows schematically the growth process for this gas composition. This composition has a broad range of grain sizes it can grow; however, this gas combination has difficulties producing smooth surfaces as a result of the H rich plasma.[20]

A combination of Ar and CH_4 has also been used to deposit ultrananocrystalline diamond[32] and graphite like diamond films. This process generates C_2 dimers from CH_4 in a two-step process while releasing hydrogen that contributes to roughly 1.5% of the steady state gas concentration. A combination of C_2 and hydrocarbon radicals are the main growth products in this method. The resultant films can be created at low temperatures, 350-400 ^oC, and have a very smooth surface morphology.[31] However, the growth process using C_2 dimers also result in films that are predominantly graphite and amorphous carbon.[33] This is a detriment as you lose some of the beneficial properties of diamond by having a mostly graphite and amorphous carbon film.

A combination $Ar/CH_4/H_2$ is the method currently used to produce the stripper foils used at the ORNL SNS. Usually only a small concentration, ~1%, of the total pressure is CH_4 while the H_2 and Ar combined make up the rest of the total pressure. This gas recipe includes production of both C_2 and hydrocarbon radicals that cause the film growth. As H_2 increases, the C_2 concentration

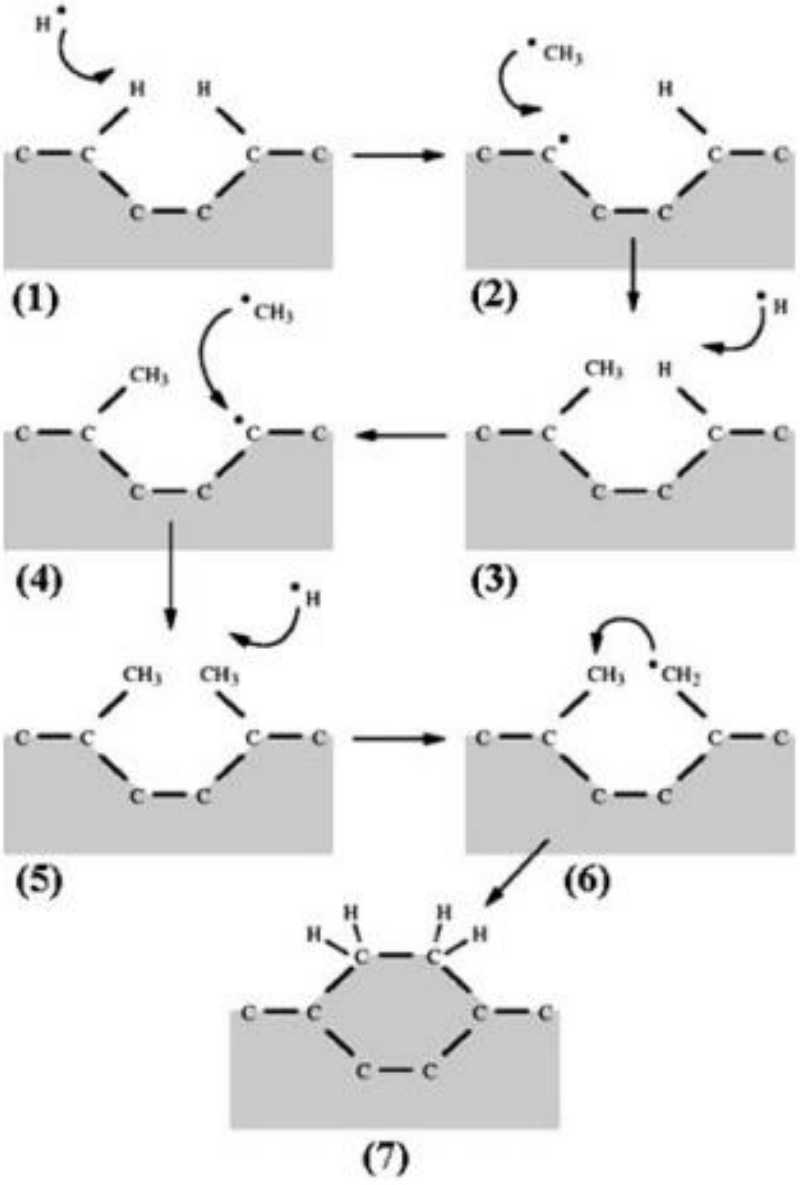


Figure 3: The diamond film growth process from a CH_4/H_2 gas mixture presented in [29]**. Step 1 shows disassociated H creating a reactive site on the substrate surface where a CH_3 can bond in step 2. This process repeats in steps 3 and 4 for a neighboring site. An H atom strikes a CH_3 in step 5 turning it into a reactive CH_2 as shown in step 6. Step 7 shows the neighboring CH_2 and CH_3 forming a C-C bond which completes the ring structure.**

reduces due to interaction with disassociated H to form C_2H.[22] As the Ar percentage increases, C_2 production is enhanced [20] and the grain size generally decreases. This trend continues and at approximately 90% Ar nanocrystalline diamond starts to form and the grain sizes decreases up to 97% Ar.[20] Plan view SEM images of various Ar percentages can be seen in fig. 4. The current SNS standard foils use a gas combination of 2% CH_4, 90% Ar, and 8% H_2.[34] This recipe results in nanocrystalline diamond films. The Ar/CH_4/H_2 gas composition has also been shown to be useful in creating ultrananocrystalline diamond.[19]

The total pressure during deposition also has to be taken into account. The pressure for MPCVD can range from roughly the 180 torr range to around 90 torr. The growth rate increases at higher pressures due to having more reactive radicals for growth. However, the nucleation density suffers at high pressure due to the increased H etching of the surface C bonds.[29] This suggests that when choosing a total pressure the importance of nucleation density needs to be leveraged against growth speed to find an optimal pressure.

1.4 Previous Work on NCD Foils

The previous research that has been performed on NCD, specifically for stripper foil purposes, has mainly been from SNS or the University of Tennessee students doing research at SNS. One of the more comprehensive studies was Eric Barrowclough's dissertation where he studied the temperature, emissivity, and graphitization transformation observed in an electron beam mimic of the

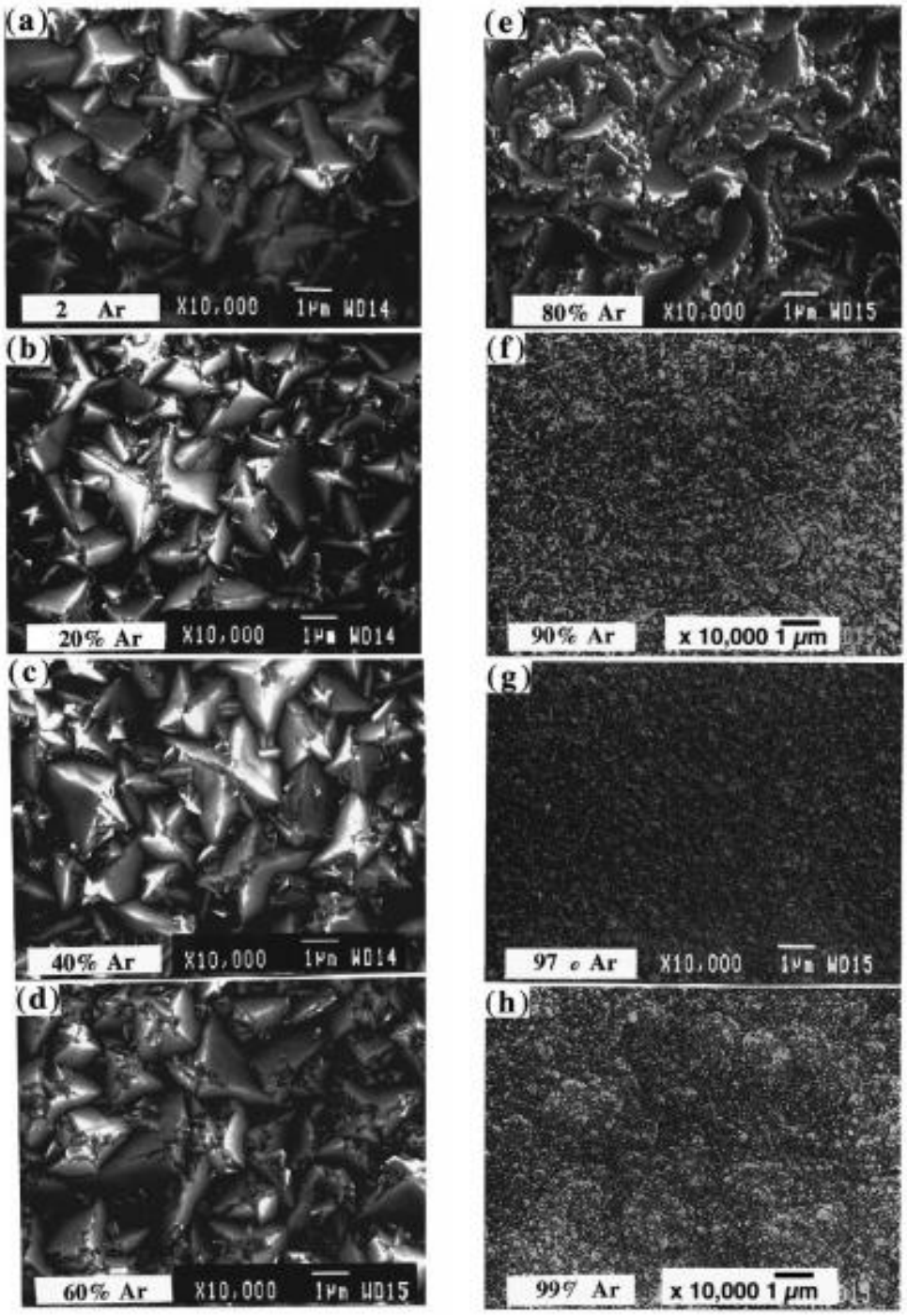


Figure 4: Plan view SEM images of MPCVD grown diamond films with various Ar percentages presented in [20]**. The CH_4 was kept at 1% of the total pressure while the percentage of Ar is shown in each picture with H_2 making up the rest of the 99%.**

SNS beam line. The goal of this mimic was to emulate the heat load that is created in the SNS beam line. This allowed for pre and post beam exposure Raman spectra and emissivity measurements to be taken, giving an insight into the high temperature transformations of NCD.[35]

1.4.1 NCD Emissivity

In Barrowclough's experiment, emissivity was measured by using an exposed, or graphitized, spot on a NCD foil as a filter between a known black body source and a FLIR camera. Because the black body source's temperature is known, the transmission of the NCD exposed spot can be calculated from the FLIR's shift in measured temperature. The emissivity was then calculated by taking 1 minus the transmission. This was performed on a number of spots on the same foil, where each spot was held at 5 minutes at 0.272 mA and 30 keV then linearly or stepwise ramped to the desired current. This resulted in the graph shown in fig. 5. Note that the emissivity rapidly changed with increasing current/temperature until it plateaued at a current density of 1.069 mA per mm^2 and a temperature of approximately 1600 K.[35]

1.4.2 Raman Spectra of PD

Raman spectra are used in CVD PD deposition to identify the phases present in the grown films. In addition to emissivity measurements, the Raman spectra for a NCD pre and post exposure to an electron beam have also been reported. Using the same linear and stepwise current ramping described in the

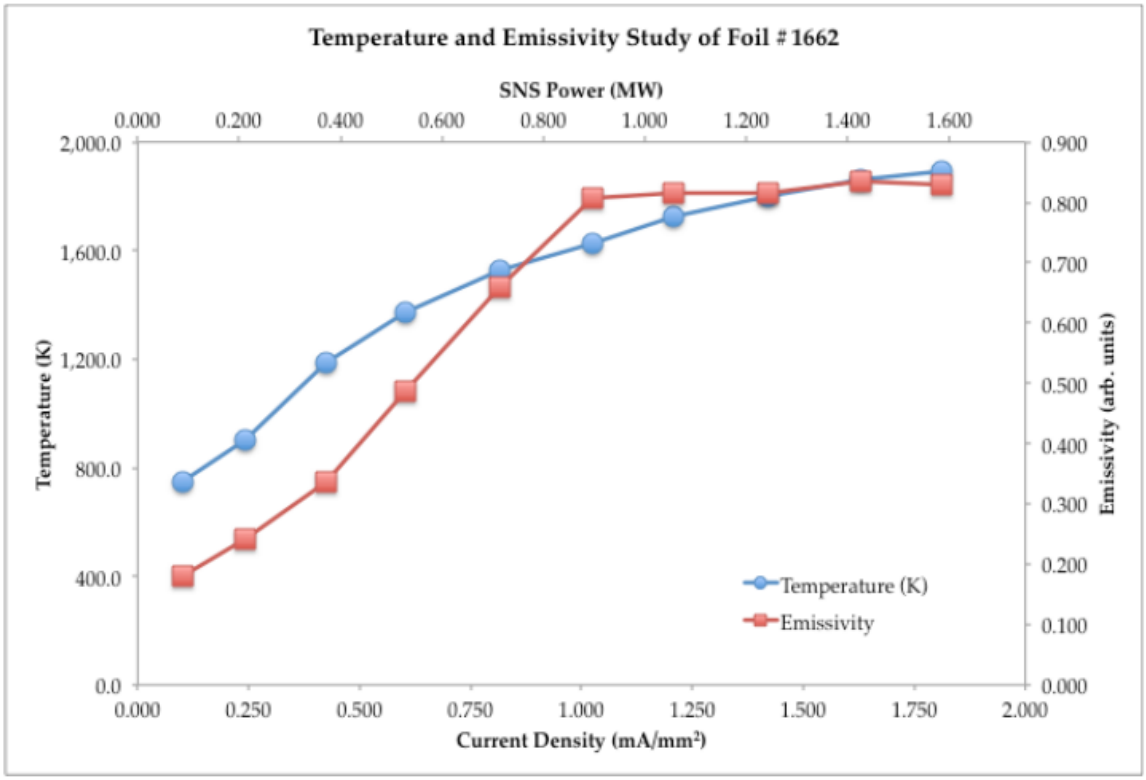


Figure 5: The temperature and emissivity of a NCD foil under increasing electron beam current density presented in [35]**. SNS equivalent power is also associated with current density.**

previous section, samples were prepared with increasing current spots and examined with Raman using both visible (514 nm) and UV (257 nm) light. This allowed for in depth examination of both the graphite and diamond. Due to graphite peaks being dominant in higher wavelength stimulation,[36] the visible light gives a smaller diamond reading than the UV stimulated spectra. Figure 6 shows the pre and post electron beam exposure for both the UV and visible spectra. It can be observed from these spectra that the graphite peak begins to dominate at higher beam currents and temperatures.[35] This agrees with the results of Khomich et al., where graphite peaks are observed following the high temperature annealing on CVD diamond was observed.[37]

In Khomich et al., MPCVD grown PD films were annealed at temperatures up to 1700 ^{o}C and analyzed using electron microscopy and Raman spectroscopy. Graphitic material was discovered via high resolution TEM to have transformed along the grain boundaries. Raman spectra also reveal two main peaks (diamond and graphite) after annealing with graphite being the dominant peak, following closely with the results reported from Barrowclough. Additionally, the fracture strengths were correlated to annealing temperature as shown in fig. 7. However, it is important to note that the PD used in this study was CH_4 and H_2 and did not include Ar like the films SNS use for stripper foils. The films used in this study are also hundreds of times thicker than the SNS films. These differences could potentially cause SNS films to have different fracture strength to annealing temperature relationships.

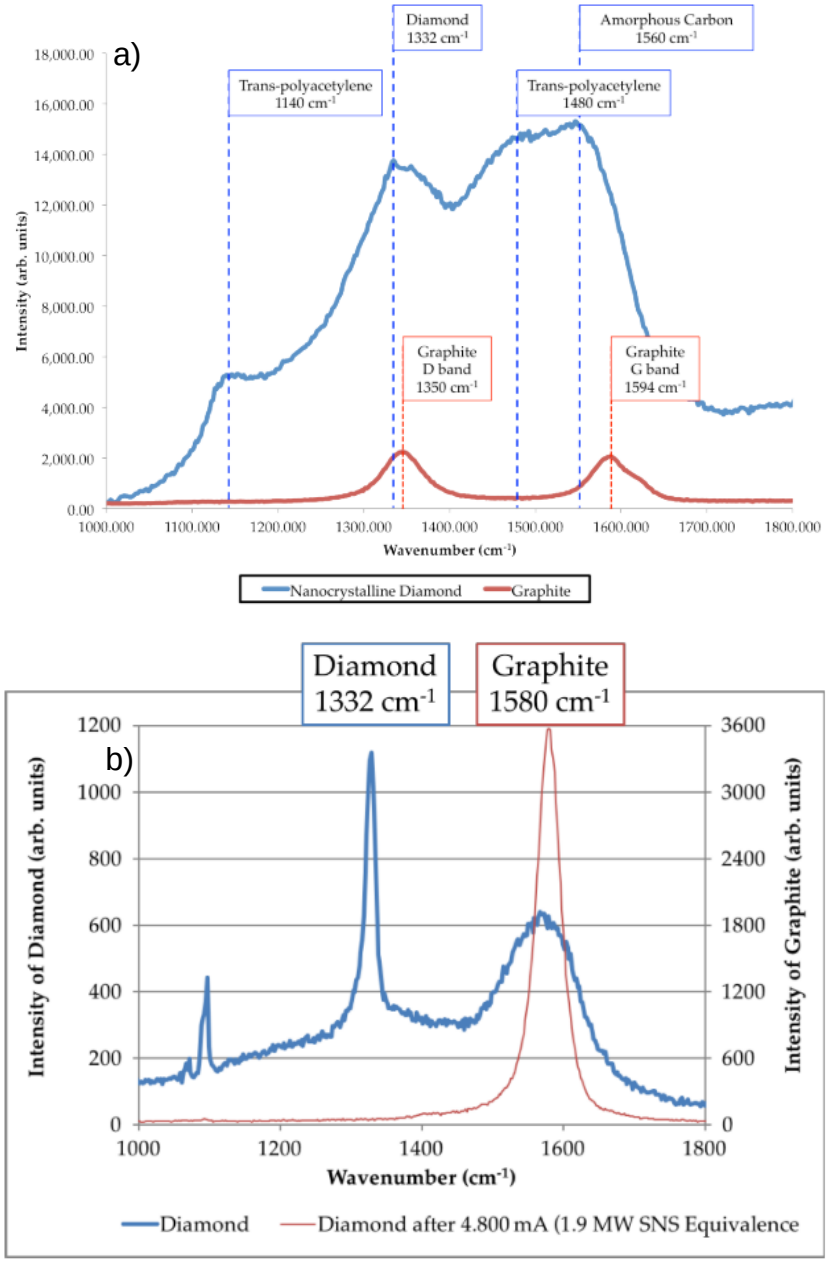


Figure 6: The pre and post electron beam exposure Raman spectra presented in [35] **using both 514 nm (a) and 257 nm (b) light. The blue curve in both plots shows the spectra before exposure while the red curve shows the foil post electron beam exposure.**

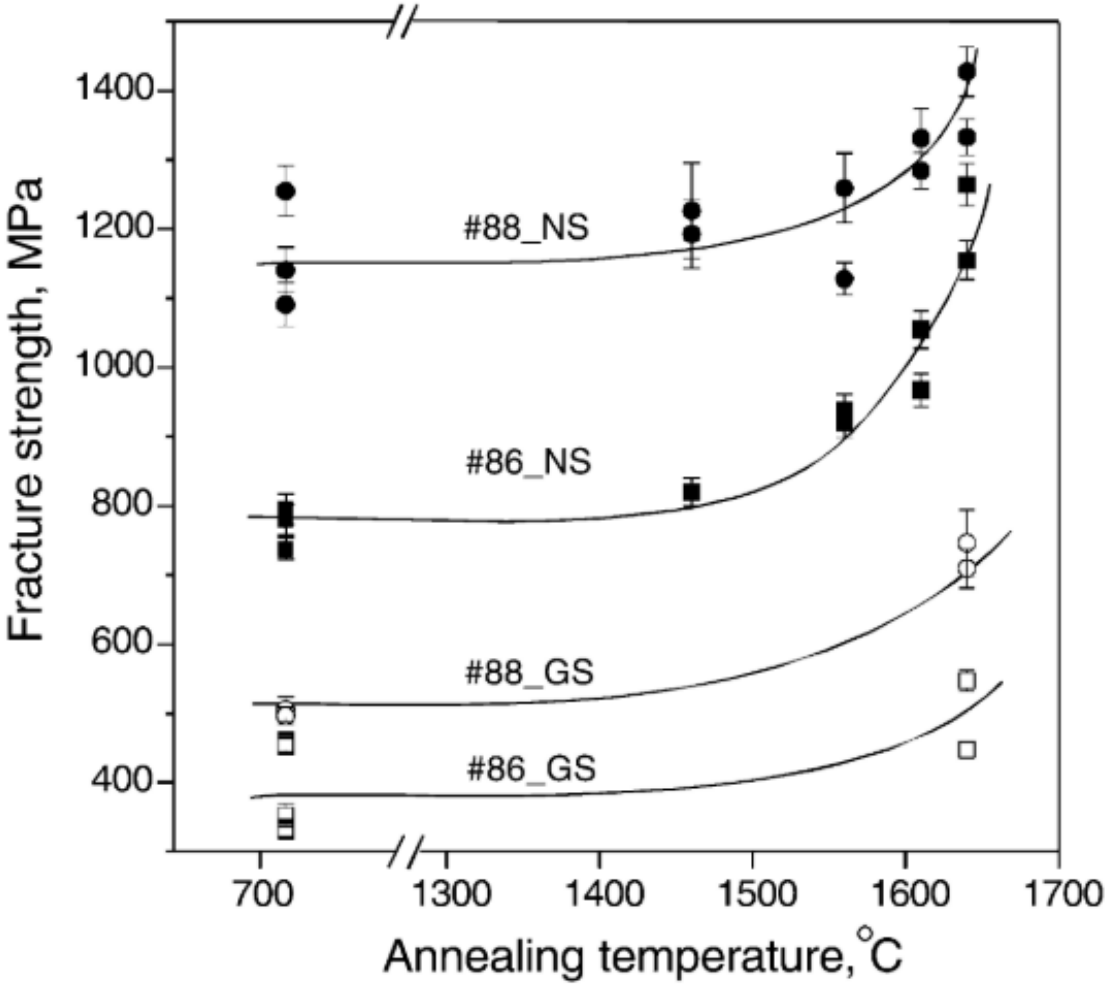


Figure 7: Fracture strength vs. annealing temperature of samples presented in [37]**. #86 is a 488 μm thick sample while #88 is 274 μm thick. The NS denotes the measurement being taken on the nucleation side of the film while GS denotes the measurement being taken on the growth side.**

1.4.3 Thermal Studies of NCD

Interest in PD as a material for MEMS use has resulted in many studies over PD's ranging thermal properties. Thermal diffusivity is often discussed as it can be directly measured instead of thermal conductivity. Thermal diffusivity is governed by the equation $K(T) = \alpha(T) \cdot Cp \cdot \rho$, where K(T) is the thermal conductivity, Cp is the specific heat, α(T) is the thermal diffusivity, and ρ is the material's density. One research of note is by Chae et al., which examines the thermal conductivity mechanics of PD with special interest in the μCD regime.[38] In this study thermal diffusivity is shown to scale negatively with the PD's graphite/diamond Raman peak ratios. Chae et al. maintained that this parameter was deposition style independent and relates the PD's crystal quality to thermal conductivity or diffusivity. Additionally in their study, it was observed that PD samples require a certain minimum thickness to obtain a high cross plane thermal conductivity. This thickness dependence is also noted by Philip et al. and is attributed to anisotropy across the thickness of the sample. The anisotropy is a result of the grain growth conditions changing with growth time.[39]

Simon et al. also investigated the changing thermal conductivity due to grain size.[11] In the study, PD samples were grown via CVD up to a thickness of approximately 290 μm. These samples were then cut at a 5.9 degree angle in the orientation shown in fig. 8a and resistive heaters were connected so 3 omega measurements of thermal conductivity could be taken. Since the CVD growth

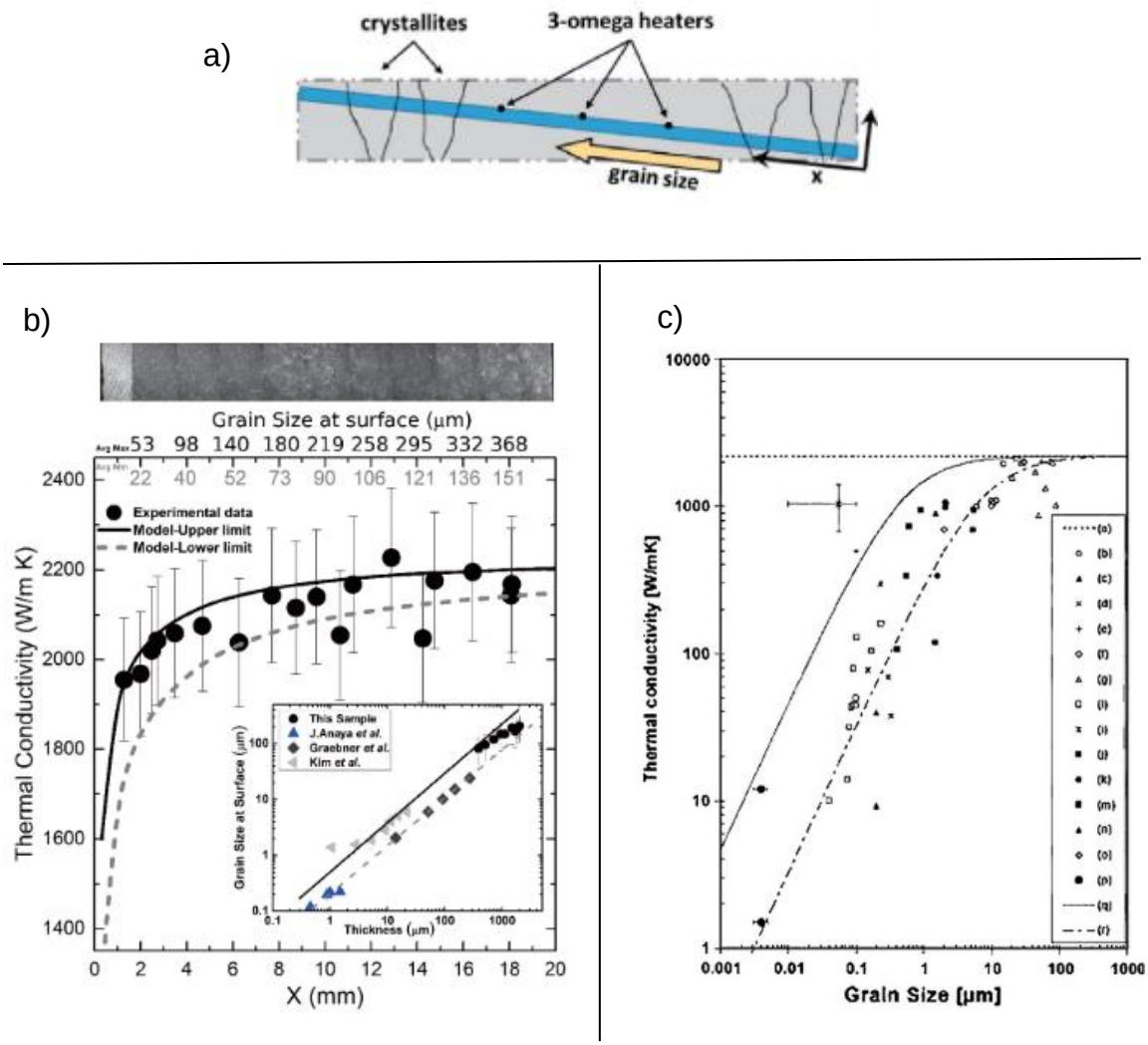


Figure 8: a) The direction of the cut and placement of resistive heaters presented in [11]**. b) The thermal conductivity as a function of cut length (orientation shown in part a) and corresponding grain sizes and SEM presented in** [11]**. c) The thermal conductivity and grain size relationship plotted from multiple sources presented in** [40]**.**

results in columnar diamond that increases grain size with the thickness of the foil, the foil thickness versus grain size was able to be examined. Additionally, the thermal conductivity as a function of thickness was also able to be examined and is plotted in fig. 8b. This plot shows that CVD diamond's surface gain size, when in the µCD range, can be controlled by adjusting the total film thickness. This study also examined film removal and found that the best thermal conductivity was obtained when 220 µm of diamond was removed from the nucleation side. Although for CEI this is not important, as stripper foils are in a much thinner regime, it has applications in other fields for heat dispersion.

A more recent study by Mohr et al. examined the effects of grain boundaries on the thermal conductivity of NCD films. In this study, films with cuboidal grains were grown with grain sizes ranging from 6 to 15 nm. The gas parameters were varied for the different films by adjusting H_2, CH_4, Ar, and He. Thermal conductivities were measured from the samples via the 3 omega method, and then grain boundary conductance was calculated from the grain boundary models.[18] These models started with from the equation $K = K_0/(1 + K_0/G_k d)$ where K is the sample's thermal conductivity, K_0 is the bulk sample's thermal conductivity, d is the grain size, and G_k is the grain boundary conductance. This is a general equation for nanocrystalline material. Mohr then added in considerations for intragranular thermal conductivity with the equation $K_{intra} = K_0/(1 + I_0/d^{.75})$ where I_0 is the phonon mean free path in the bulk sample. Combining the NCD and intragranular equations Mohr arrived at. $K =$

$(K_0/(1+I_0/d^{.75}))/(1+(K_0/1+I_0/d^{.75})/(d\cdot G_k))$. The grain boundaries are assumed to have the same approximate thickness across all samples. Through this method, grain boundary contributions to the PD's thermal conductivity were calculated and correlated the Young's modulus and thermal conductivity versus grain size. Figure 9 illustrates that thermal conductivity scales linearly with grain size which is correlated to a decrease in the GB thermal resistance. This study showed that NCD films have increased Young's modulus and thermal conductivity as their grain sizes become larger.

The relationship between PD thermal conductivity and temperature has been investigated by multiple sources.[41–44] Additionally, the effects that annealing at high temperatures has on thermal conductivity were also examined.[37] Figure 10 shows the results from several studies. At low temperatures there is a noticeable increase in in-plane thermal conductivity as seen in fig. 10a. From 200 K into the 400 K range the thermal conductivity slope plateaus or slightly declines (shown in fig. 10 plots a, b, and c). In the annealing test, the thermal conductivity stays relatively constant until the temperature regime where graphitization occurs, ~1300 K, and the thermal conductivity significantly drops. The thermal conductivity continues to drop sharply at around 1600 K (shown in fig. 10 part d). It is important to note that this high temperature annealing experiment measured the cross plane and not the in plane thermal conductivity. This causes the collimated grains to give a thermal conductivity of near pure diamond, whereas values this high are not observed in the in plane

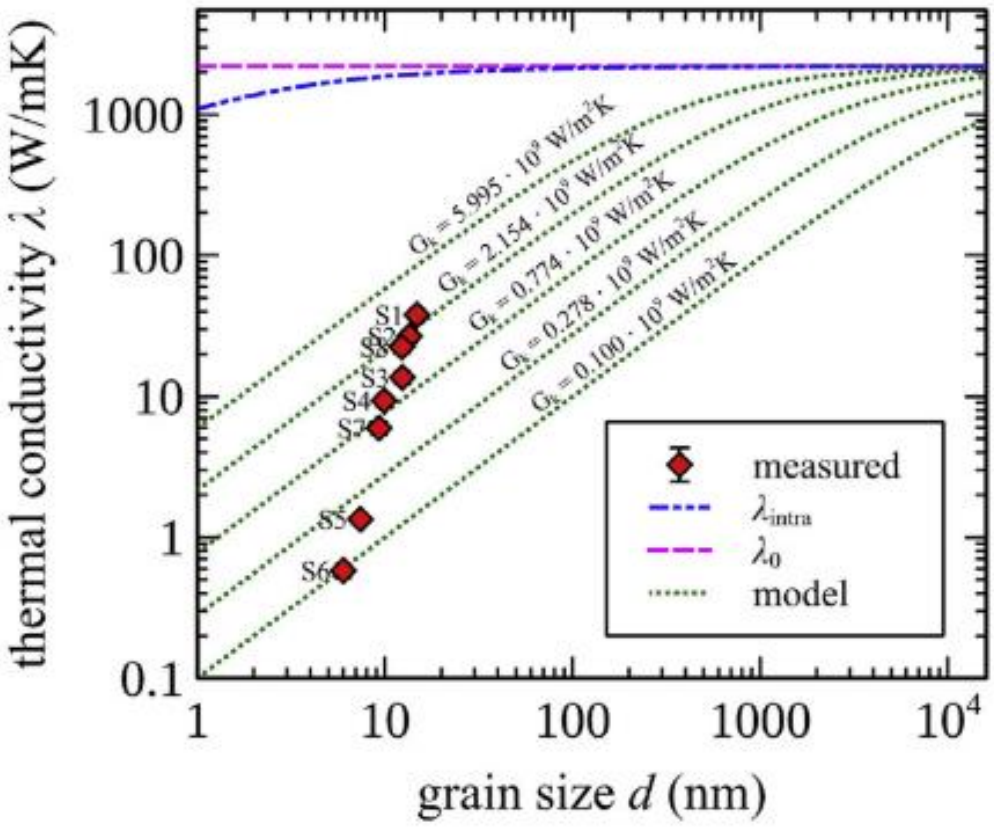


Figure 9: Thermal conductivity's relation to grain size as presented in [18]**. The dotted lines show the simulated curves given the stated grain boundary conductance.**

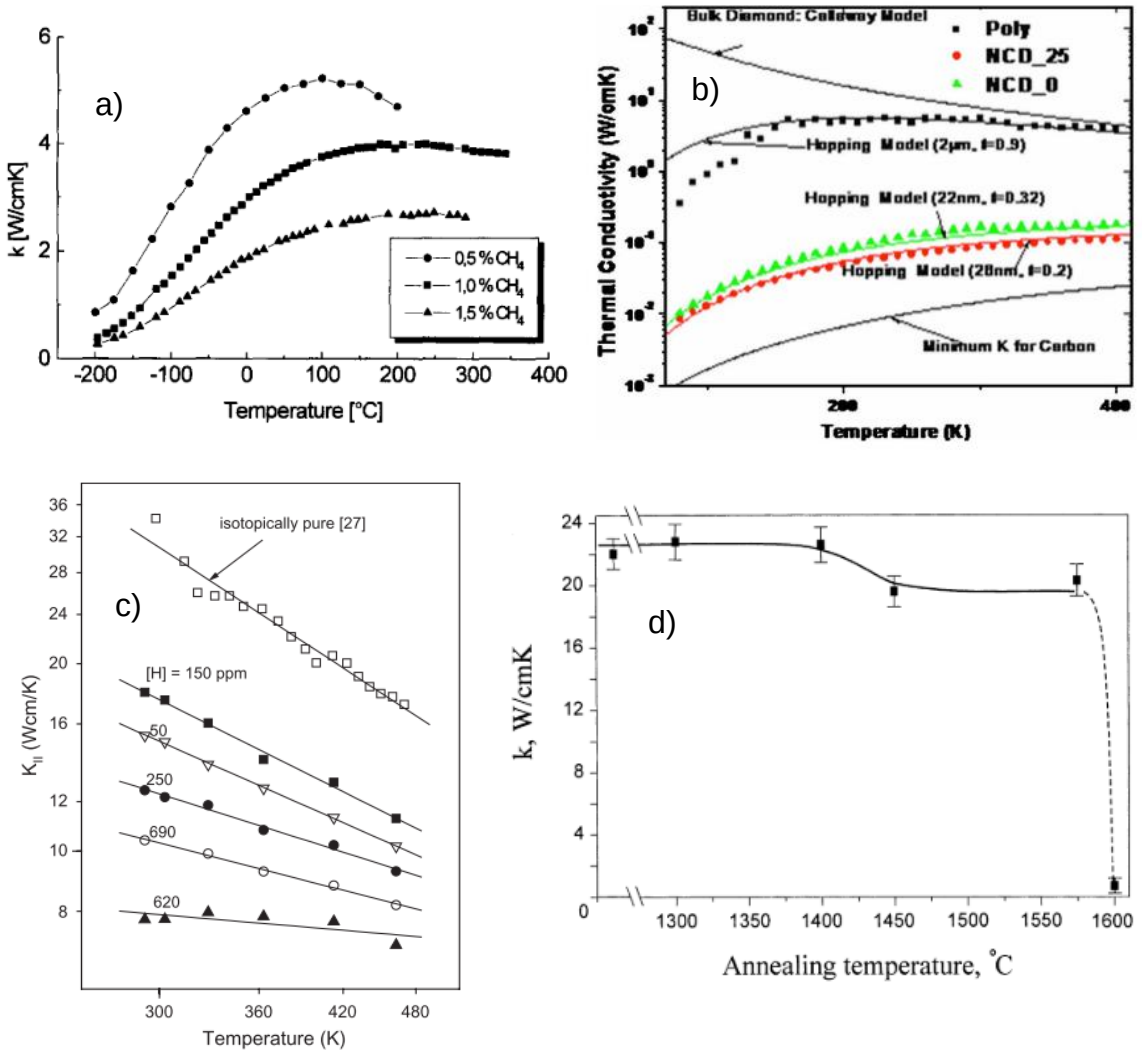


Figure 10: In plane thermal conductivity of polycrystalline diamond vs. temperature made with H/CH_4 gas compositions presented in [44]**. b) In plane thermal conductivity of μCD (poly), undoped NCD (NCD_0), and N doped NCD (NCD_25) vs. temperature presented in** [45]**. c) Thermal conductivity vs. temperature of as-indicated hydrogen impurity measured in ppm presented in** [43]**. d) Thermal conductivity as a function of annealing temperature presented in** [37]**.**

thermal conductivity measurements. Although the above studies are not exhaustive, regarding the research in the field of CVD diamond thermal properties, they do serve as an overview of the work pertinent to PD stripper foils.

1.4.4 NCD Simulation

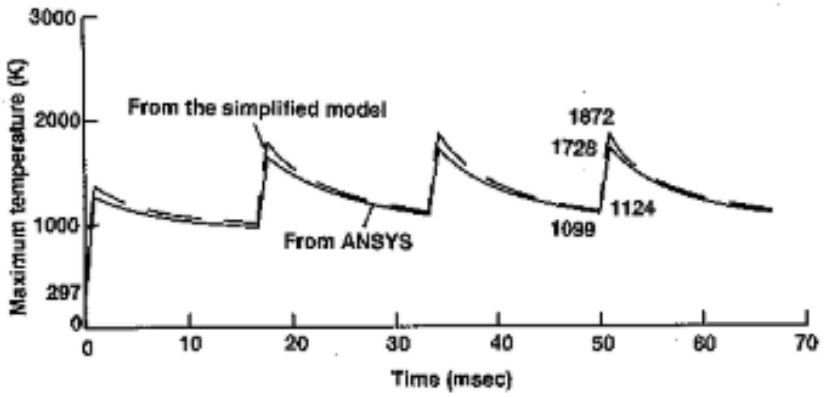
Attempts have been made to predict and simulate the resultant temperatures and failure points for NCD stripper foils[46–48]. NCD stripper foil failure is qualified as thinning or foil change that causes large changes in stripping efficiency. Stripper foil thermal simulation is important because it allows for predictions about how a foil will operate in the beamline before exposure and potential foil failure. Additionally, methods have been developed to measure in situ temperature on the stripper foil [49,50]. Simulations and predictive foil failure can work together with real time stripper foil temperature measurements to prevent or mitigate foil failure in the SNS beam line.

One of the first attempts to simulate the SNS stripper foil temperature occurred in 1999 by Liaw et al[48]. The authors used ANSYS to model the heat flow and generation in the SNS foil. They take two different approaches, the first is a simplified model that has a heat generation term and accounts for energy loss through thermal radiation with the surrounding beam pipe set at a constant value. The second model accounts for thermal losses through conduction in the foil and an evolving thermal profile on the beam line pipe. They calculated beam temperatures for foils with an areal density of 400 and 220 μg/cm^2. The 400

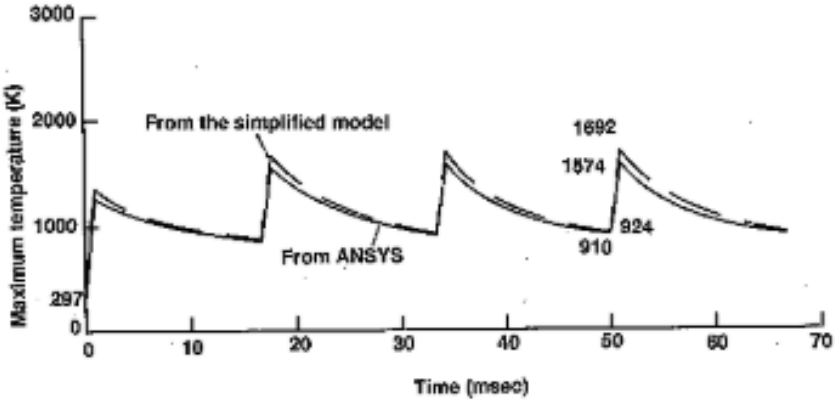
μg/cm^2 foil was calculated to be from 1099 to 1728 K, with the simplified model producing a slightly higher temperature range. Liaw's simulation results with the simplified and ANSYS models can be seen in fig. 11. Additionally, they tested for if the foil would fail within 10 minutes of exposure by measuring the power density of an exposed beam and equating it with corresponding temperatures from simulation. These results corresponded well carbon's melting temperature. There is no mention of long term instability due to sublimation from these results.

In 2008 Lebedev and Lebedev published an article on the calculated lifetimes of thin stripper foils under irradiation from pulsed ions[46]. In this study they examined foil failure due to two different mechanisms. Equations were derived for the lifetime of a stripper foil based on sublimation and radiation damage. From these equations they concluded that below 2500 K radiation damage becomes the dominant factor in deciding the lifetime of the SNS stripper foils and above 2500 K sublimation become the dominant factor. However, it is worth noting that the predicted lifetimes of the foils in this paper are noticeably different than what is seen in the beamline. Lebedev and Lebedev predict a foil lifetime of .5 to 1 hr at 1 GeV, unlike observed SNS foil lifetimes that can be up to months.

In 2013 a study by Takeda et al. was published where they simulated the heat load on stripper foils made of diamond, graphite, boron, boron carbide, h-boron nitride, and c-boron nitride using the program ANSYS[47]. In their study, they found that diamond had the highest resultant temperature of the different



The maximum temperatures on the carbon foil verse time in SNS (area density: 400 μg/cm^2)



The maximum temperatures on the foils verse time (area density: 220 μg/cm^2)

Figure 11: The thermal simulation results for Liaw et al. using a simplified and complex model presented in [48]**.**

simulated foils. It is worth mentioning that while the study listed the material parameters used, they only did so at room temperature and made no indication if thermal conductivity and heat capacity scaled with temperature. Additionally, there was no mention of a changing emissivity or accounting for graphitization of the diamond foil. This can make a big difference as heat radiation scales with emissivity and diamond has an emissivity of .3 compared to graphite's value of .8 to .9.

CHAPTER I
THERMAL CONDUCTIVITY OF NANO- AND MICRO-CRYSTALLINE DIAMOND FILMS STUDIED BY PHOTOTHERMAL EXCITATION OF CANTILEVER STRUCTURES

A version of this chapter was originally published by Leo Saturday, Leslie Wilson, Scott Retterer, Nicholas Evans, Dayrl Briggs, Philip Rack, and Nickolay Lavrik[51]:

L. Saturday, L. Wilson, S. Retterer, N.J. Evans, D. Briggs, P.D. Rack, N. Lavrik, Thermal conductivity of nano- and micro-crystalline diamond films studied by photothermal excitation of cantilever structures, Diam. Relat. Mater. 113 (2021) 108279. https://doi.org/10.1016/j.diamond.2021.108279

Author's Contribution

The author's contribution included the fabrication, testing, simulation, and writing of the paper. The author fabricated the bilayer cantilevers and tested them on using a photothermal excitation and reading setup created by Nickolay Lavrik. SEM images were taken by the author and Nickolay Lavrik. The paper was written predominantly by the author with the CVD section being written by Leslie Wilson. The manuscript was not changed from the published version.

Abstract

Polycrystalline diamond films have unique structural and thermal properties that make them suitable for use in extreme environments. Recently, they have been utilized in accelerator beamlines for electron stripping due to their unique combination of mechanical and thermal properties. Thermal conductivities of nanocrystalline diamond (NCD) and microcrystalline diamond (μCD) films were characterized using photothermally actuated bimaterial cantilevers.

Approximately one micrometer thick NCD and μCD cantilevers were fabricated from microwave plasma enhanced chemical vapor deposition grown polycrystalline diamond (PD) films. A layer of gold was sputtered on the diamond film surfaces to make bilayer cantilevers and the thermal response time was measured by photothermally exciting the bilayer cantilevers, causing them to deflect. Finite element thermomechanical modeling of the deflection dynamics in response to photothermal actuation was performed to determine the NCD and μCD thermal diffusivities and conductivities. By fitting the simulated and experimentally observed response times, thermal conductivities of 10 and 60 W/(m-K) were extracted for the NCD and μCD samples, respectively. Expected changes in thermal conductivity of PD in higher temperature regimes are also discussed. In addition to applications of PD films as electron stripping foils, these findings also have implication in fields such as micro/nano-electromechanical systems.

Introduction

Over the past several decades polycrystalline and, in particular, nanocrystalline diamond (NCD) films [13] have drawn a great deal of attention due to their unique properties, such as high thermal conductivity and desirable mechanical properties, that are useful for applications in numerous areas including industrial tools, nano-magnetometry, and lubrication [14]. These fundamental properties of polycrystalline diamond thin films can be drastically different compared to macroscopic single crystal diamond samples, and are

highly dependent upon the grain structure of the films. This is particularly true for nanocrystalline diamond that exhibit substantial optical absorption, low thermal conductivity and high density of defects, such as nitrogen vacancy (NV) centers.

The history of nanodiamond synthesis is traced back to 1963 when Volkov *et al.* discovered that detonation of carbon based materials yielded ultrafine dispersions of diamonds crystals [15]. However, it was not until the late 1990s, that methods for growing continuous polycrystalline films became available. Polycrystalline diamond films with grain sizes ranging from the micro- to nano-scale can be grown by various modifications of chemical vapor deposition (CVD) techniques [17], in particular hot filament CVD [18] and microwave plasma assisted CVD (MPCVD) [19–22].

Our present study is motivated primarily by applications of nanodiamond films used in harsh environments as electron stripping foils in accelerators and spallation neutron sources [52–54], where a combination of long-term mechanical and chemical stability under extreme conditions is of paramount importance. To this point, we focus on the thermal conductivity of two dissimilar types of polycrystalline diamond (PD) films prepared by MPCVD on silicon wafers and subsequently lithographically patterned as a microscale singly clamped beam/cantilever. Using the photothermal excitation and optical readout technique developed for characterization of micromechanical IR detectors [55] we show that the in-plane thermal conductivity of microcrystalline diamond films is six times higher than that of nanocrystalline diamond films. The data obtained

in the present study are compared to the findings reported by other groups [18]. The insights yielded through the development of the techniques used to shape these cantilevers and testing in a micromechanical platform will enable refining of films optimized for use as larger scale stripping foils. Additionally this study can act as data points for comparison with PD film studies that range the various parameters involved in thin film creation.

Experimental

MPCVD growth of polycrystalline diamond films

Polycrystalline diamond films were grown in the DiamoTek 700-6 Microwave Plasma CVD system (Fig.12) from Microwave Enterprises, Ltd. In brief, single side polished single crystal (100) silicon substrates ranging in size from 1” x 1” chips to 2” wafers with approximately 500 µm thickness were seeded with diamond slurry using sonication procedures described previously [34]. Samples were sonicated in a solution of .005 g diamond nano-powder with approximate diamond sizes of 3.2 nm. The surface coverage of the film after 5 minutes of growth was previously shown to be ~ 90%. After loading the substrates into the processing chamber, the PD film growth was initiated by igniting a microwave plasma (6kW, 2.45 GHz) in a mixture of H_2, CH_4, and Ar feeding gasses at a pressure in the range of 40 to 105 Torr. The gas ratios, power, and pressures were the main variable parameters that enabled control of

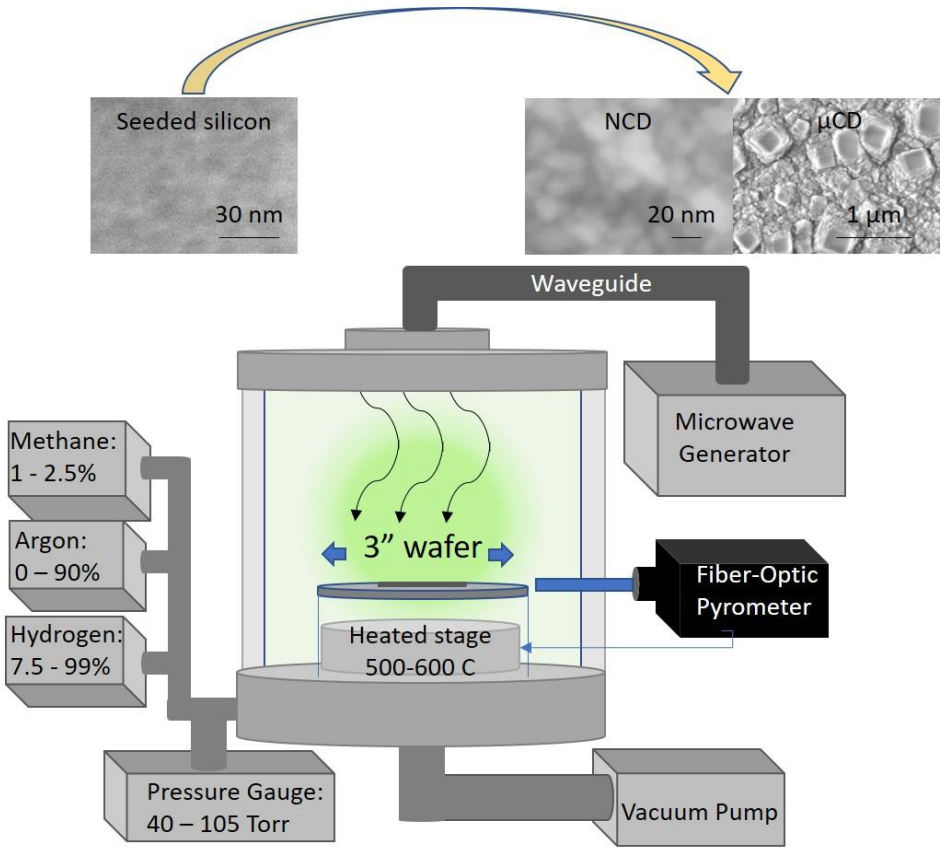


Figure 12: Schematic of the MWPECVD tool used in the present study.

the grain size in the resulting films. The microcrystalline diamond (µCD) was grown with 1% CH_4 and 99% H_2 at a pressure of 40 Torr and power of 1620 Watts. The NCD was grown with 2.45% CH_4, 90% Ar, and 7.55% H_2 at a pressure of 105 Torr and power of 1330 Watts.

While there are other gas chemistries that result in PD growth, only the µCD and NCD recipes listed earlier were chosen. The NCD recipe was chosen due to it being the current Spallation Neutron Source standard stripper foil recipe [7], as well as recent interest in similar recipes for ultranano crystalline diamond and nanocrystalline diamond research [56]. The µCD recipe was chosen due the CH_4/H_2 combination being one of the better researched methods for polycrystalline diamond CVD deposition [21,57–59].

Fabrication of microcantilevers

Cantilever structures were fabricated using the processing sequence overviewed in Fig. 13. After the PD layer was grown, a 300 nm layer of SiO_2 was deposited on top of the PD layer via Oxford Instruments Plasmalab System 100 PECVD to act as a hard mask during subsequent reactive ion etching (RIE) steps. The photoresist S1813 was spin coated and baked for approximately 60 seconds. The photoresist was then patterned in a Suss MicroTec MA6/BA6 Gen3 mask aligner. CD-26 developer was used to develop the exposed photoresist layer. After drying, the sample was baked on a hotplate for 5 minutes at 115 C. The pattern was successively transferred to the SiO_2 and PD layers using a

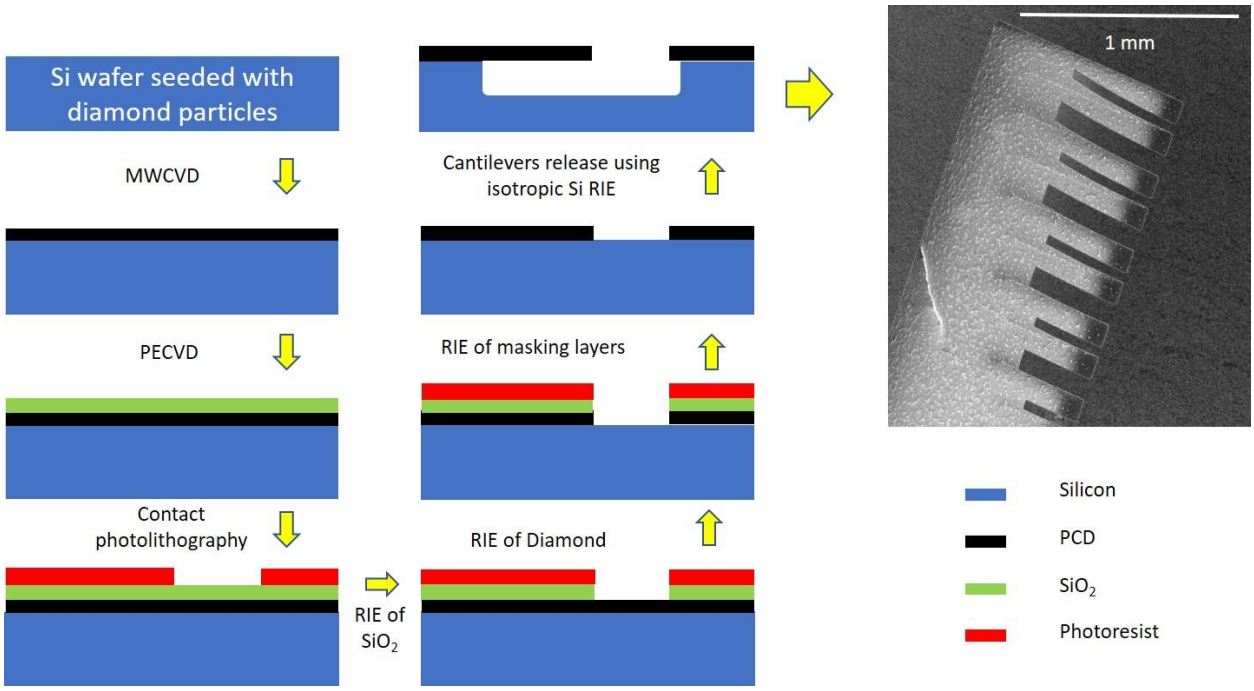


Figure 13: Wafer level processing sequence used to fabricate microcantilevers using PD films as a structural material.

sequence of two anisotropic RIE steps in an Oxford Instruments PlasmaLab System 100 plasma dry etcher.

Before releasing the cantilevers, a final RIE step was performed to remove any residual photoresist and SiO_2 film. An isotropic Si dry etch was used to etch the underlying silicon wafer and undercut the PD patterns, which fully released the cantilevers from the Si chip. Lastly, a 50 nm layer of gold was sputter deposited onto the PD film/cantilevers using an AJA International ATC 2400 sputtering system.

Raman microscopy and SEM characterization

Raman spectroscopy is a commonly used tool for identifying the different phases and quality of diamond films. Thus Raman spectroscopy measurements were taken using Renishaw InVia Raman microscope with 633 nm light. Scanning electron microscope images of the gold coated diamond films were also taken to compare the film morphologies and to confirm the diamond film thickness. The SEM images were taken with a Thermo Fischer Scientific Nova 600 NanoLab and the Carl Zeiss Merlin FE-SEM.

Thermal conductivity measurements

There are multiple ways to measure thermal diffusivity, such as transient hot wire, 3-omega, transient plane source, and the laser flash method. Each of these methods has differing limitations on the temperature range and the range of thermal conductivity values they are able to measure [20]. Many of these

methods require heat sources to be in contact with the sample and rely on macroscale machining not compatible with thin films. The implemented bilayer cantilever photothermal excitation method is most suitable for studying thin films with applications in micro/nano devices and chip-level systems. Compared to other previously demonstrated thermal conductivity measurements compatible with chip level systems, the advantage of the technique demonstrated in the present study is that it does not require fabrication of resistive heating elements. When compared to methods that rely on contact heat sources, such as the 3-omega method, photothermal heating can potentially enable measurements at much higher temperatures not limited by the thermal stability of the heater material. Additionally, this method has the advantage of measuring thermal conductivity in-plane instead of across the film. When looking at various thermal conductivity measurements it is important to keep track of the direction of heat propagation. Anisotropic thin films can lead to drastic differences between the in-plane and cross-plane thermal flows. For stripper foils and applications like microelectromechanical systems (MEMS) the thermal conductivity in-plane can be more critical than across the film. This is due to heat being confined to the suspended film and flowing along the film to the lower temperature base.

The thermal conductivity measurements used the methodology depicted in Fig. 14 that was developed previously for characterization of bimaterial cantilever thermal detectors [60]. Specifically, two diode lasers were focused on the bimaterial (Au/PD) cantilevers inside of a vacuum cell through an optically

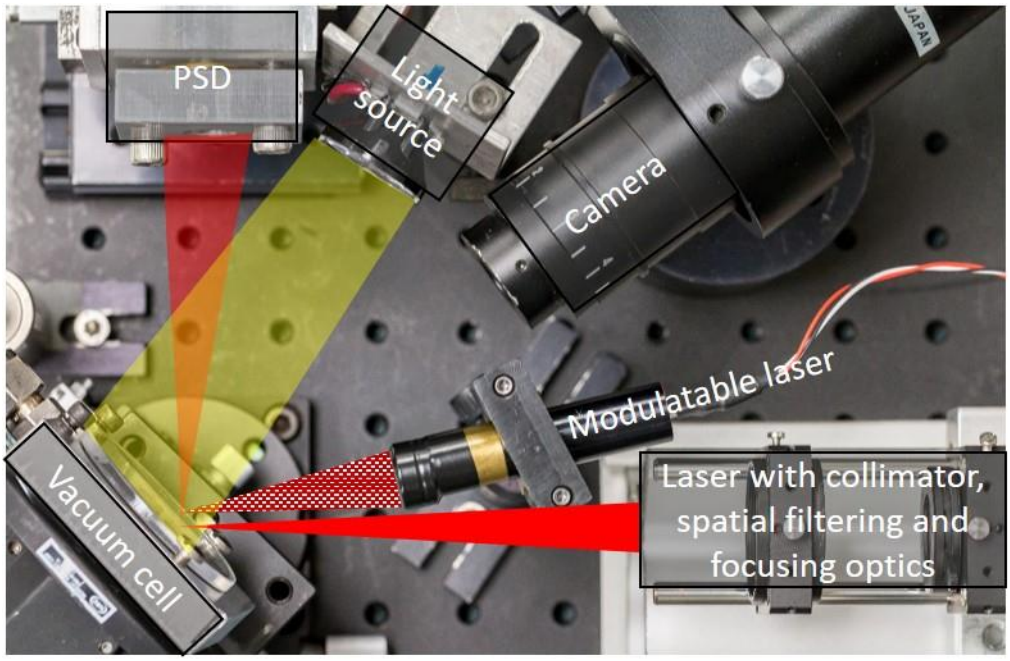


Figure 14: Setup for photothermal excitation and optical readout of the microcantilevers fabricated in the present study.

transparent window. The first laser enabled an “optical lever” readout similar to the ones commonly used in atomic force microscope (AFM) tools and was focused towards the tip of the cantilever. The light reflected off the cantilever is read by a position sensitive detector adjacent to the vacuum cell. A second laser, modulated in time with a square wave pulse sequence, was focused near the base of the cantilever in order to provide photothermal excitation, which causes the cantilever to bend due to the bimaterial difference in the coefficients of thermal expansion [61]. It is important to note that, although the magnitude of the bimaterial cantilever’s deflection in its steady state is dependent on the cantilever length, coefficients of thermal expansion of material 1 and 2, and their thermal conductivities, our method relies on transient response of the cantilevers and is not affected by the steady state deflection amplitude. The measured cantilever deflection time constants (rise and fall) determine the thermal conductivity, independent of the magnitude of the deflection. Additionally, the mechanical resonances of the cantilevers were measured using the optical lever readout. The output of the position sensitive detector was analyzed using a spectrum analyzer.

Finite element analysis (COMSOL modeling)

The structural mechanics part of our finite element analysis (FEA) model is based on a singly clamped beam geometry comprised of two stacked materials. The linear elastic material approximation was used since the expected deformations under the conditions of photothermal excitation are typically very

small and within the linear elastic range of the stress-strain curve. The fixed constraint boundary condition was imposed on the edge of the bimaterial cantilever. The linear elasticity model was coupled to the thermal expansion and heat propagation models by using appropriate modules and the multi-physics solver in COMSOL.

The heat load boundary condition within a circular area along the cantilever centerline was used to account for the photothermal excitation of the cantilever beam using a focused laser beam. The value of the heat load was selected to be 50% of the incident laser beam power, which assumes 50% optical absorption by the bimaterial cantilever. Although this is a reasonable approximation, it is important to emphasize that the exact value of the heat load does not affect the resulting thermal response time due to the linear nature of the thermal and elastic processes. This was confirmed in the model by doubling the beam power and observing only a 1% shift in the cantilever response time. Additionally, our simulations show a maximum of 25 K increase in cantilever temperature during photothermal excitation with 0.1 mW power. The estimated 0.1mW of applied power is based on the known power of the laser beam (approximately 1 mW at the cantilever plane) and the reflectivity of the gold coated cantilevers (approximately 90%). Therefore, the cantilever experiences only a modest temperature increase for the given laser power of our experiment.

Material parameters for gold from COMSOL materials database were used for the top layer of the bimaterial cantilever with the exception of thermal

conductivity. Due to the gold layer thickness (~ 50 nm), its thermal conductivity is anticipated to be somewhat lower than the reference bulk value. Therefore, an assumed thermal conductivity of 170 W/(m K) for a 50 nm gold layer as reported by Lugo *et al.* was used [62]. For the main PD structural layer of the bimaterial cantilevers, the Young's modulus, and thermal conductivity were variable parameters while its density was measured experimentally, and Poisson's ratio and thermal capacitance were set according to COMSOL materials database and with the previously published studies, respectively [63]. Additionally, the cantilever thickness, length, and width were set to the actual cantilever geometries determined from optical and SEM images (Table 1). The transient deflection of the cantilever in response to the photothermal heat load was analyzed using a time dependent solver. The cantilever tip position was tracked versus time in order to compare to the measured photothermal response time.

A sensitivity analysis was performed to examine error propagation in the model. This was performed by adjusting the heat capacity, heating laser position, PD density, Au thermal conductivity, laser power, and cantilever thickness individually. Each parameter was adjusted by 10% and the resultant shift in the response time was simulated. Heat capacity and density were the most sensitive sources of error propagation each shifting the response time by 16%. All other parameters resulted in a 3.5% or lower shift in simulated response time. According to our best estimates, input parameters have an uncertainty of

Table 1: COMSOL model input and output parameters. The parameters with an asterisk have been experimentally calculated or measured. The parameters without an asterisk were pulled from literature.

model input parameters																	model output	
sample PD type	thermal response time*, t (sec)	pc-D structural layer							Au coating									
		thickness*, t_D (m)	width*, w_D (m)	length*, l_D (m)	density*, ρ_D (kg m^{-3})	specific heat capacity, c_D (J K^{-1} kg^{-1})	young's modulus, E_D (N m^{-2})	poisson ratio, ν_D	thickness*, t_{Au} (m)	width*, w_{Au} (m)	length*, l_{Au} (m)	density, ρ_{Au} (kg m^{-3})	specific heat capacity, c_{Au} (J K^{-1} kg^{-1})	young's modulus, E_D (N m^{-2})	poisson ratio, ν_D	thermal Conductivity k_{Au} (W m^{-1} K^{-1})	thermal diffusivity*, (m^2 s^{-1})	thermal conductivity* (W m^{-1} K^{-1})
µCD	8.50E-04	1.00E-06	5.00E-05	3.00E-04	3420	540	8.00E+11	0.1	5.00E-08	5.00E-05	3.00E-04	19300	129	7.00E+10	0.44	145	1.80E+07	50
NCD	1.40E-03	1.10E-06	5.00E-05	3.00E-04	2900	690	7.50E+11	0.1	5.00E-08	5.00E-05	3.00E-04	19300	129	7.00E+10	0.44	145	2.00E+06	10

approximately 10%. This leads to a total uncertainty in the deduced thermal conductivity of 24%. Additionally, the structural mechanics module of the FEA model was used for eigenfrequency analysis to predict cantilever fundamental mechanical resonances as a function of the cantilever thickness, length, and Young's modulus of its structural material.

Results and Discussion

Raman spectra of the NCD sample show graphite and disordered graphite peaks at 1579 and 1348 cm^{-1}, respectively and can be seen in Fig. 15. Due to the Raman laser wavelength of 633 nm, the D and G peaks are substantially larger than the diamond peak, which is maximized with wavelengths closer to the UV range [36]. Additionally, the peak at 1195 cm^{-1} suggests C-N vibrations, while the peak at 1488 cm^{-1} indicates distorted sp^3 in the sample [64]. The µCD Raman spectra has a visible diamond peak at around 1330 cm^{-1} due to smaller signal contributions from both the D and G groups. The monotonically increasing background signal in the µCD Raman spectra has been attributed to photoluminescence from C-H bonds [65].

Densities of the µCD and NCD samples were calculated to be 3.4 and 2.9 g/cm^3, respectively. These values were calculated from the change in mass of the sample before and after PD deposition as well as the measured thickness and calculated area of the PD layer. The PD layer thickness was determined to be approximately 1.1 µm for the NCD sample and 1 µm for the µCD sample via

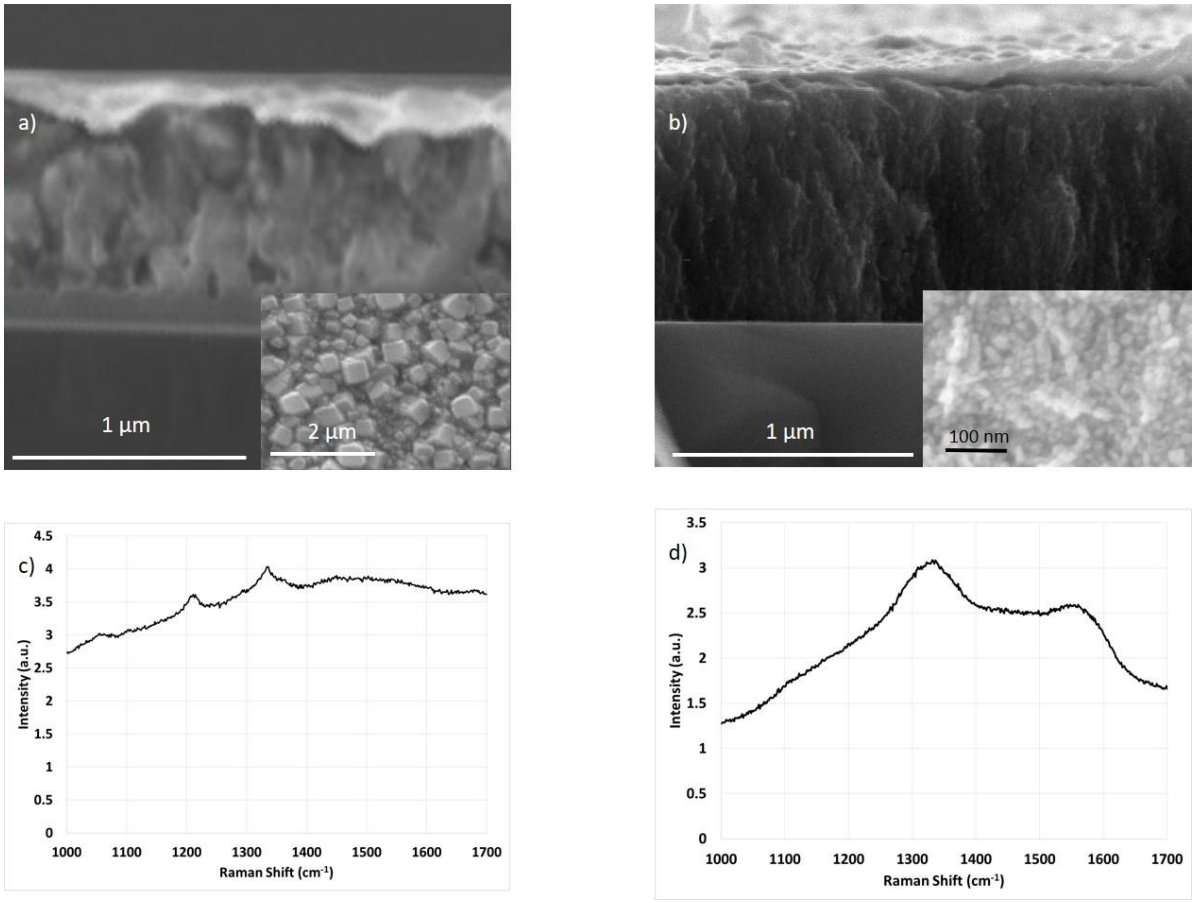


Figure 15: SEM of µCD (set a) and NCD (set b) film. Accompanying Raman spectra of µCD (c) and NCD (d) samples.

SEM imaging shown in Fig. 4. Additionally, SEM imaging confirmed that, the gold layer was ~50 nm thick, furthermore the grain sizes of the diamond films were approximated. The NCD sample has an estimated grain size of 14 nm with a roughly cubic shape. The µCD sample grains had a more rectanguloid shape with the long edge spanning the full 1 µm height of the film. The shorter edges were approximately 300 nm in width and length.

Due to the isotropic silicon dry etch, the base of the cantilevers were undercut approximately 25 µm for the NCD and 85 µm for the µCD. To accommodate for the undercutting, the cantilever length was extended for both the eigenfrequencies simulations as well as the photothermal excitation simulations. According to our analysis of the experimental data, µCD and the NCD films have a similar Young's modulus of approximately 800 and 750 GPa, respectively, which is in good agreement to the previous results of Mohr *et al.* for a NCD sample [18].

The Young's modulus values were subsequently used in the photothermal excitation model to get excitation curves based on differing thermal conductivities for the µCD and the NCD samples, while holding their respective thermal capacitance constant. These simulations were then compared to the experimental deflection readings shown in Fig. 16. In plane thermal conductivity of approximately 60 W/(m K) for µCD and 10 W/(m K) for NCD are estimated based on the best fit to the experimental data. These thermal conductivity values are close to previously reported thermal conductivities for similar grain sizes [66].

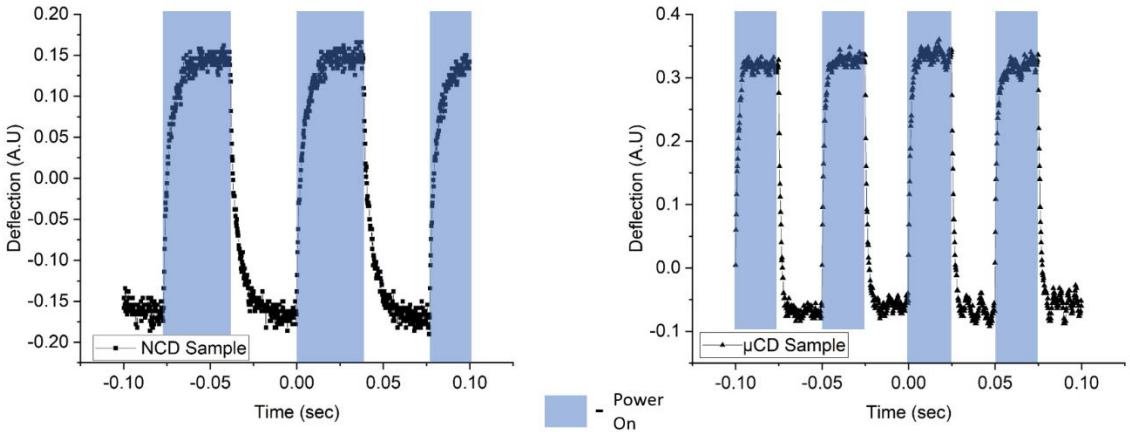


Figure 16: Transient deflection of bimaterial cantilevers measured in response to pulsed photothermal excitation.

Additionally, grain boundary thermal conductivity for the NCD sample was calculated to be 0.83 * 10^9 W/(m^2K) based on the approach described by Mohr *et al.* [18]. Since the µCD sample had columnar shaped grains, the grain boundary thermal conductance was estimated in the plane direction by using the 300 nm side edges. This approximation resulted in a grain boundary conductance of 0.29 * 10^9 W/(m^2K), suggesting more phononic impedance in the µCD sample.

It is important to note that the grain boundary conductance approximations might not be accurate for our samples. Mohr *et al.* used isotropic cubic shaped grains with a set grain boundary thickness in their estimations and, while this may be an accurate representation for NCD samples, it could vary drastically for the µCD samples. Additionally, more aggressive etching of non-diamond phases in the H_2 rich CVD processes makes intergranular voids more abundant in the µCD sample. The abundance of voids, coupled with variability in grain boundary thickness and composition, make the assumptions used in Mohr's study not necessarily valid in the µCD regime.

A schematic representation of the µCD and NCD microstructures can be seen in Fig. 17. For the µCD structure we expect the space between grains to be dominated by voids. This would lead to a much lower grain boundary conductance, which agrees with the grain boundary conductance calculations. For the NCD we expect the grains to be more closely packed with much less contribution from voids. Extra emphasis is being put on the void distribution in this analysis due to it being one of the heaviest contributors to phononic

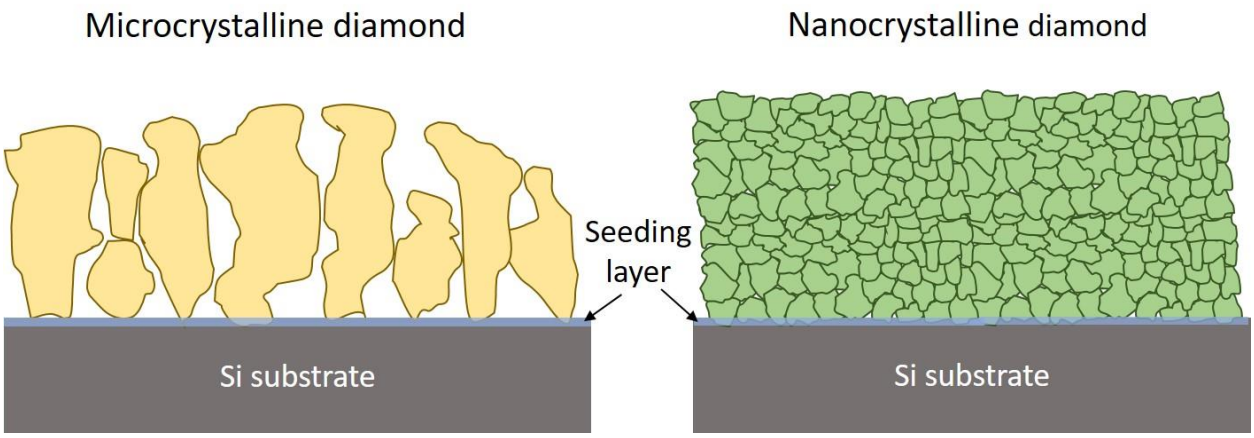


Figure 17: Schematic representations of the µCD and NCD samples.

impedance in these systems. This means that decreasing the void fraction in the μCD sample could raise the thermal conductivity significantly. It is reasonable to expect that an increased void fraction in the grain boundaries should reduce the effective Young's modulus of the PD materials. Additionally, increased void fraction lowers the density of the material. The grain boundary volume in the μCD sample is much smaller than for the NCD sample, which correlates with the higher density relative to the NCD but lower relative than single crystal diamond's density (3.51 g/cm^3). Assuming the majority of the grains consist of voids and the μCD's density, the sample could be up to 3% voids. NCD's density, however, also reflects the relationship between the proportion of diamond and graphite or amorphous C content in the film. Using the NCD's density and assuming graphite dominated grain boundaries, the grain boundaries constitute up to 49% of the sample. Increased void density also effectively lowers thermal conductivity in the PD samples by limiting the areas of interaction between the grain and grain boundaries.

Multiple studies have shown that PD thermal conductivity depends significantly on grain size [11,18,66]. Grain boundaries and voids act as barriers for phonon propagation, which lower the effective thermal conductivity of a material. In general, as grain sizes increase in PD materials, thermal conductivity increases, which is consistent with the difference between the two samples reported in this study.

An important factor for PD, especially in uses such as a stripper foil material [7,34,52,67], is the change in thermal conductivity due to temperature. There are two types of changes that occur in the material's thermal conductivity, reversible and irreversible. Irreversible thermal conductivity changes mainly take place as graphitization in PD samples. Nebel *et al.* demonstrated that graphitization initiates in PD anywhere from 1200 C to 1400 C [12]. This graphitization process can be expected to lower the overall thermal conductivity of a sample due to a resistance effect as demonstrated by Khomic *et al* [37]. Reversible temperature dependence of PD's thermal conductivity has been studied previously in select temperature regions [42–44]. These studies have shown PD's thermal conductivity generally increases with temperature below room temperature and starts to flatten out above ambient temperature. While there have been some thermal conductivity measurements done for PD, these are at only slightly elevated temperatures that do not approach the high temperatures (>1000 ^{o}C) used in stripper foils. At higher temperatures, heat radiation becomes a dominant factor. Heat radiation coupled with material restraints at elevated temperatures make high temperature thermal conductivity measurements challenging. The thermal conductivity at ambient temperature acts as a baseline parameter that determines heat flow around localized high temperature spots, as well as a basis to gauge high temperature measurements of thermal conductivity. Future work will investigate high-temperature thermal conductivity measurements, which the method described here is suitable for.

Conclusions

Two different PD samples were grown with differing gas chemistries and fabricated into bilayer cantilever structures in order to determine the PD layer's thermal conductivity. The thermal conductivity of the NCD film was determined to be 10 W/(m-K) and the μCD film was determined to be 60 W/(m-K) by comparing FEA and experimentally measured thermal response times of photothermal heating of bimaterial cantilevers. These values are consistent with similarly sized NCD and μCD films [66]. Young's moduli for both samples were calculated based on Eigenfrequency cantilever measurements and does not significantly vary (800 versus 750 GPa). It is expected that the thermal conductivity will decrease as temperature increases from room temperature to ~1200 ^{o}C where graphitization occurs. The graphitization is expected to cause an increase in phononic impedance, which will lower the thermal conductivity of the sample. While this could be of concern for stripper foil purposes, the graphite has a higher Stefan-Boltzmann's constant and thus competing radiation must also be considered for high-temperature applications.

Acknowledgements

This work was supported by the DOE office of Science User Facilities. LS, LW, and NE are supported through funding for the Spallation Neutron Source Stripper Foil Research and Development program, which is a DOE Office of Science User facility. Thin film synthesis, cantilever fabrication, material characterization and

modeling were conducted at the Center for Nanophase Materials Sciences, which is also a DOE Office of Science User Facility.

CHAPTER II
EXPERIMENTAL AND SIMULATED HEATING IN NANOCRYSTALLINE DIAMOND CHARGE EXCHANGE INJECTION FILMS USING AN ELECTRON BEAM TO MIMIC SNS CONDITIONS

A version of this chapter was originally published by Leo Saturday, Leslie Wilson, Scott Retterer, Nicholas Evans, Chris Luck, and Philip Rack[68]:

L. Saturday, C. Luck, L. Wilson, J.D. Fowlkes, P.D. Rack, N.J. Evans, Experimental and simulated heating in nanocrystalline diamond charge exchange injection films using an electron beam to mimic SNS conditions, Nucl. Instruments Methods Phys. Res. Sect. A Accel. Spectrometers, Detect. Assoc. Equip. 1027 (2021) 166226. https://doi.org/10.1016/j.nima.2021.166226.

Author's Contribution

The author's contribution included the testing, simulation, and writing of the paper. Leslie Wilson fabricated the nanocrystalline diamond foils. SEM images were taken by the author and Nickolay Lavrik. The paper was written predominantly by the author. Chris Luck assisted with gathering data and photography of the foils. The manuscript was not changed from the published version.

Abstract

Nanocrystalline diamond (NCD) foils have been in use at the Spallation Neutron Source as primary stripper foils for charge exchange injection since the machine's inception. NCD's low atomic number leads to reduced beam scattering while still being easy to handle, as opposed to even lighter elements. NCD foils also have the benefit of being free-standing, and rigid when grown under the right conditions to minimize residual stresses. This study overviews a method to mimic

the Spallation Neutron Source (SNS) beam and characterize thermally driven failure of NCD foils. To do this, a foil test stand was developed with in situ diagnostics that tracks signs of foil sublimation and thinning. The foil test stand's electron beam is equated to the SNS beamline by comparing peak deposited energy densities for both beams. Post-mortem testing is also conducted to help elucidate changes the NCD foils undergo during exposure to the beam. A COMSOL simulation was also developed as a method to assess potential future changes to the NCD film and predict how changes to beam conditions will affect foil temperatures. This method allows for examination of the NCD foil's thermal limits and can be used to assess future changes to SNS stripper foils.

Introduction

Charge exchange injection (CEI) is a process where a beam of H- ions are converted to H+ ions to increase the phase space density of a beam for the operation of high-power proton sources such as the Spallation Neutron Source (SNS) at Oak Ridge National Laboratory. This charge conversion is traditionally achieved through the interaction of the H- beam with either a solid material called a stripper foil, or a jet of gas, or liquid[9]. Beam scattering due to CEI scales with both atomic number and thickness of the stripping medium[3]. Carbon based materials are frequently used as stripper foils for the CEI process[69]. Carbon's low atomic number results in reduced scattering of the interacting charged particle beam compared to higher atomic number alternatives. Additionally, many forms of carbon have high thermal conductivity and enable better heat

dispersion. Carbon stripper foils are generally limited by their lifetime when exposed to beam, which is shortened by a combination of thermal and mechanical failure. In order to extend the stripper foil lifetime and help mitigate some of these failure mechanisms, SNS has developed a nanocrystalline diamond foil[34] with improved mechanical and thermal stability compared to amorphous carbon foils. Though foils usually perform very well, and are often removed from service before failure, when foils do fail, graphitization and subsequent deformation of the SNS foils are the primary failure mechanism. This deformation typically leads to higher beam loss, or unpredictable behavior related to small changes in foil positioning that is unacceptable for operations, rather than catastrophic failure. However, sublimation has been observed during SNS operation under non-ideal beam conditions, and as beam power density increases with future SNS upgrades, sublimation is expected to occur and could potentially be a problem for reliable operation. While sublimation of the SNS nanocrystalline diamond foils has been observed, an explicit examination of the limits of the SNS NCD foils has not been thoroughly conducted.

Previous work has been done to examine the lifetimes and temperatures for carbon stripper foils. Stripper foil lifetime estimates have been proposed in other works with regards to radiation and evaporation [46] as well as foil thickness [70]. Additionally, the temperatures generated during charge exchange injection on the foil has been simulated [5,47,48,71] and experimentally measured [49]. Electron beams have also been utilized to mimic and examine

the heating effects on stripper foils [70,72]. Recently, diagnostics were developed and implemented for in situ monitoring of pinhole formation and thinning of stripper foils [73]. In this work we examine the thermal limits of the SNS NCD stripper foils.

One of the limiting factors in electron stripper foil research is the ability to dedicate beam time to test and change out stripper foils in the SNS beam line. In order to expedite testing, an electron beam Foil Test Stand (FTS) was developed to emulate the heating caused by the SNS beam[74]. The FTS mimics the energy deposition into the foil by equating the stopping power of the SNS H^- beam to an equivalent electron beam stopping power. This method does not mimic the radiation damage caused by high energy protons, however, from SNS operational experience, foil lifetime is believed to be limited by sublimation due to heat. Several *in situ* diagnostics have been added to the system for *in operando* monitoring to elucidate critical steps in the foil failure. Here we overview the FTS system and correlate *in situ* diagnostics and post-mortem characterization to the thermomechanical failure of nanocrystalline diamond foils under electron beam conditions that mimic the SNS beam.

Methods

Nanocrystalline diamond (NCD) films were first fabricated for testing at the Center for Nanophase Materials Sciences. Samples were deposited in DiamoTek 700-6 Microwave Plasma CVD system using parameters as described in previous literature[51]. Experimentally, the deposited material usually varies

around 0.1 mg. When accounting for the exposed surface area of the silicon chip, this deposition corresponds to an areal density of 357 to 372 µg/cm2 and a thickness ranging between 1.23 and 1.28 µm for the FTS samples and a representative SNS stripper foil. After diamond synthesis and the subsequent etching/release from the substrate, the ~ 1µm thick nanocrystalline diamond samples were mounted in the foil test stand (FTS) for testing. An overview of the FTS along with the associated hardware and measurements are illustrated in figure 18.

FTS Hardware

Foils are first mounted to the vertical and rotational multi-motion feedthrough that is illustrated in the photograph in figure 18 a) and schematic in b). Up to four foils can be mounted in the system and the samples are able to be rotated 360^{o}. This allows the foil to be positioned 30^{o} from normal to the electron beam, emulating the interaction angle of the SNS H^- beam with the stripper foil. The electron beam is generated with a Kimball Physics electron source that generates an approximately Gaussian beam profile. The end of the electron gun is positioned approximately 120 mm from the foil. Along the electron gun diameter a Faraday cup is mounted on the other side of the chamber that has a 3 mm diameter current limiting aperture. A FLIR camera is attached normal to the face of the foil. A gas analyzer is also attached to a port and is shielded by an optically dense baffle. Typical graphs of the gas analyzer, FLIR temperature measurements, emission current, and Faraday cup current are shown in figure

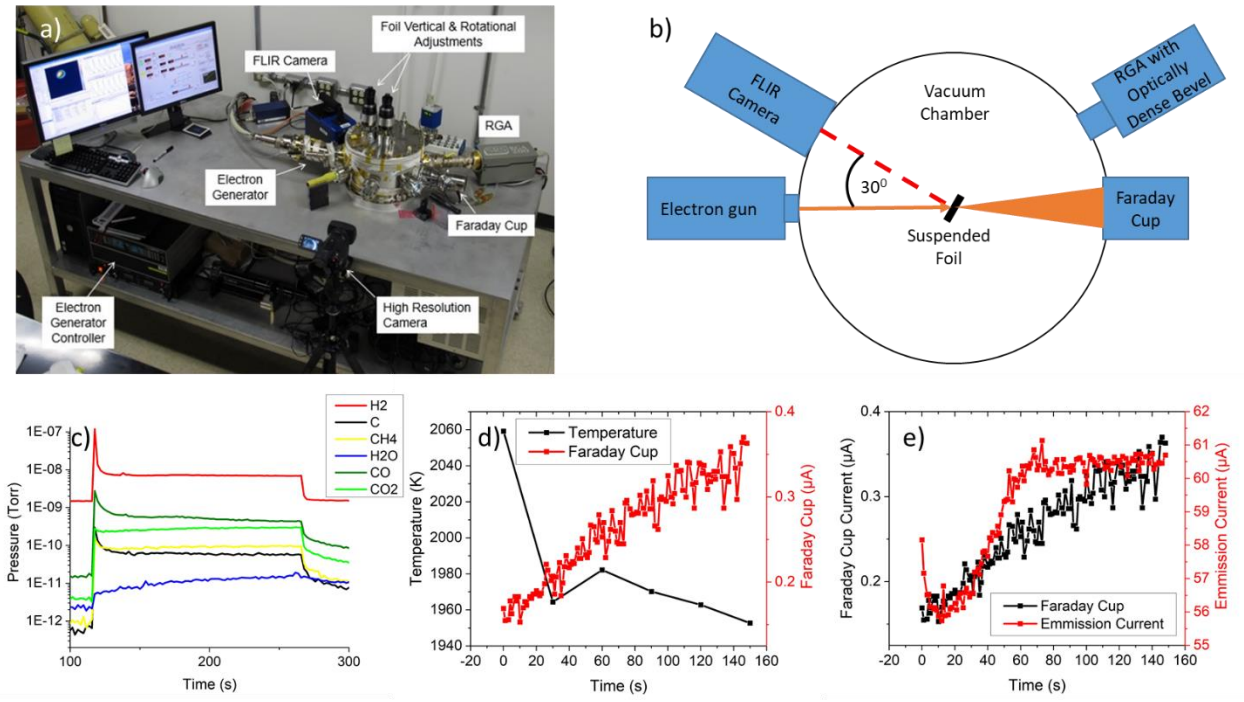


Figure 18: Figure 1. a) Photograph and b) schematic of the Foil Test Stand. Example outputs from the c) residual gas analyzer, d) FLIR camera and Faraday cup, e) Faraday cup and electron gun emission current.

18c, 18d, and 18e for the irradiation of a previously unexposed spot. Lastly a high definition camera is mounted outside of a transparent vacuum window for high resolution imaging of the foil before and after exposure. The vacuum pressure is held in the 10^{-8} to the 10^{-9} torr range and fluctuates during foil tests.

FTS Measurements

Once mounted on the FTS multi-motion feedthrough, the stripper foils are exposed to an electron beam that, as described below, has comparable energy deposition in the carbon foil as the 1.0 GeV, 1.4 MW H^- + H^+ beam. During the electron beam exposure, the FLIR IR camera captures the two dimensional temperature profile of the foil at a calibrated exposure. The FLIR camera has a temperature accuracy of ±1% assuming an accurate object emissivity. Note that to obtain the absolute temperature the image must be calibrated against the spot's emissivity. The temperature profile and maximum temperature is tracked and reported throughout each run. It is important to note that since the emissivity changes during beam exposure, the temperature measurements are slightly inaccurate in the early frames when the electron beam first interacts with the foil. This inaccuracy is due to the emissivity change of the foil during initial graphitization[35]. During beam exposure the residual gas analyzer is set to track specific mass-to-charge ratios (figure 18c)) that are expected to outgas or sublime from the foil. Some of the specific mass-to-charge ratios that are recorded look for H_2O that can desorb from surfaces due to increased temperature, and carbon/carbon byproducts that can be the results of sublimed

free carbon. The Faraday cup is used to monitor the un-scattered beam current which can be correlated to the FLIR camera temperature reading (figure 18d)) and the emission current of the electron gun (figure 18e)). The foil irradiation shown in figure 18c, d, and e is on a previously unirradiated spot. When irradiating a fresh spot, the partial pressure spikes, and the emission current drops by approximately 10%, which subsequently decreases the foil temperature. The drop in emission current and foil temperature is attributed to electron beam and thermally stimulated desorption of physisorbed gas-phase products on the diamond foil, which when released subsequently interact with the electron gun cathode. The high-definition camera is used to image the foil *in situ* as well as collect post irradiation photos of the exposed area. The foil holder is also used as a beam scraper, which is incrementally raised so the measured Faraday cup current change as a function of position could be recorded, which was used to re-construct the beam profile [see supplemental information for details].

SNS Equivalent Current

The equivalent SNS and FTS peak beam currents were estimated by equating the energy deposited in the nanocrystalline diamond foil for both beams via the relative stopping powers of the particles and the beam profiles. As will be described below, the emission current and beam profiles are measured for the 30 keV electrons and the electron stopping power for a 30 keV electron is 8.6290 MeV cm^2/g. The SNS peak energy deposited is estimated using the stopping power of a carbon foil for a proton and 2 electrons at their relative energies

assuming a 1.0 GeV H^- beam. The recirculating proton beam is also accounted for as it strikes the foil on average 4 to 5 additional times. The peak current including recirculating beam is estimated from realistic ORBIT simulations[75] of the entire injection process that includes all relevant effects. Stopping power values for the convoy electrons and protons at their respective energies are 1.761 MeV cm^2/g and 1.946 MeV cm^2/g, respectively. The simulated SNS beam profiles are briefly described in the supplemental information, where it is noted that the H- and H+ distributions are slightly offset. Thus, accounting for the beam profiles, one can approximate the equivalent peak SNS and FTS currents based on the peak energy deposited per area for each beam, where:

$$1.65 \times i(FTS_{e^-}) = i(SNS_{4.5H^+ + H^-})$$

The reader should note that this equivalence assumes the current 1.0 GeV SNS proton beam energy. After the Proton Power Upgrade, SNS will be capable of a 1.3 GeV beam, and the energy deposition of both protons and electrons will decrease by about 5% for foils of similar thickness.

Post Mortem Testing

After the foils are tested in the FTS, post mortem testing was also performed. Raman spectra were taken of the exposed foils in multiple areas (shown later). Polycrystalline diamond is commonly examined and identified using Raman spectroscopy and gives insight to the carbon phases present in the sample [33,76]. Scanning electron microscopy (SEM) was used to take surface images of the exposed areas and gives insight into the potential causes of failure

in the foil. Additionally, a black body source is used to measure the emissivity of the foil's exposed and unexposed area. To do this the foil is used as a filter between the black body source and the FLIR IR camera. This allows us to determine the transmission from the exposed spots and calculate the emissivity[35].

Simulation

Finite element methods were used to model heat flow in the stripper foils. A Monte Carlo simulation was first performed to better estimate the energy deposition profile of the electron beam interacting with a carbon foil at a density of 2.9 g/cm^3 and an areal density of 362.5 µg/cm^2 which corresponds to a foil thickness of 1.25 µm. The Monte Carlo algorithm used to generate individual electron trajectories has been described previously[77] and is based on the algorithm developed by Joy[78]. The simulation of electron exposure was 3D with respect to the electron beam – target interaction. Multiple simulations were executed to study the implications of changes in sample thickness and the sample tilt orientation with respect to the beam. In each study, the inelastic energy loss in the z–coordinate, i.e., parallel to the beam trajectory, was compiled as a function of the z–coordinate (depth). The total stopping power at 30 keV was determined to be 9.24 MeV cm^2/g, which is similar to the value of 8.575 MeV cm^2/g given in the NIST ESTAR database[79], assuming a constant energy loss for 30 keV electrons in carbon. Subsequently, these profiles served as an energy generation term in the heat diffusion partial differential equation that

was solved using a finite element method solver. The energy loss profile was scaled to the FTS current distribution and used as the heat source for the COMSOL model to simulate the thermal evolution of the stripper foils during electron beam exposure[80]. The percentage of inelastic energy contributing to heat by the beam (ε) was adjusted in order to get a correct fit between experiments and simulations. As mentioned above, the electron beam profile was measured using the foil holder, which was progressively moved to measure the collected current. The derivative of this profile was then fit to a 1D integral of a 2D Gaussian ring function and used for the simulated beam profile.

Thermal conductivity and specific heat values are temperature dependent and need to be considered in the thermal model due to the high temperature range experienced under the electron exposure. It should be noted that graphitization occurs in the temperature region above 1473 K [37] and could influence these terms. The specific heat of carbon allotropes seem to be fairly consistent with minimal variance between its forms[81–83]. Therefore specific heat values from previous literature, up to 3000 K, were used to estimate temperature dependent specific heat[83]. Thermal conductivity, however, can vary significantly between different diamond[84] and graphite[6,85,86] samples. This is problematic as the evolution of the NCD graphitization is not specifically known. For this model, a piecewise function was constructed for the thermal conductivity of un-graphitized foils. As NCD has a fairly flat curve at room temperature, thermal conductivity was assumed to be constant and assigned the

previously measured 10 W/(m*K)[51] until it reaches 1300 K. From 1300 to 1500 K the thermal conductivity transitions linearly to an isotropic polycrystalline graphite estimation; at temperatures greater than 1500 K a function that fits high temperature polycrystalline graphite is used. As will be justified below, for the pulsed simulations, the thermal conductivity of the central graphitized spot is assumed to be polycrystalline graphite. See supplemental information for specific heat and thermal conductivity temperature dependent functions used in the simulations.

Results and Discussion

The main signatures of sublimation in the FTS are changes in temperature and Faraday cup current normalized to the emission current. Foil thinning leads to less scattering of the primary electron beam and thus an increase in the measured Faraday cup current. Additionally, as the foil thins due to sublimation, the electron energy deposited in the foil decreases, and consequently the temperature decreases. Thus, the Faraday cup and FLIR IR camera readings are the primary indicators of sublimation *in situ*. However, changes in the electron gun emission current can also occur during the foil testing, thus in order to compensate for changes in the electron gun current, the Faraday cup current is normalized by the emission current. Figure 19 is a plot of the ratio of the Faraday cup current and the emission current versus time for two different pulsed emission beam currents. As the emission current increases, the sublimation rate increases as evidenced by the steeper slope of the normalized Faraday cup

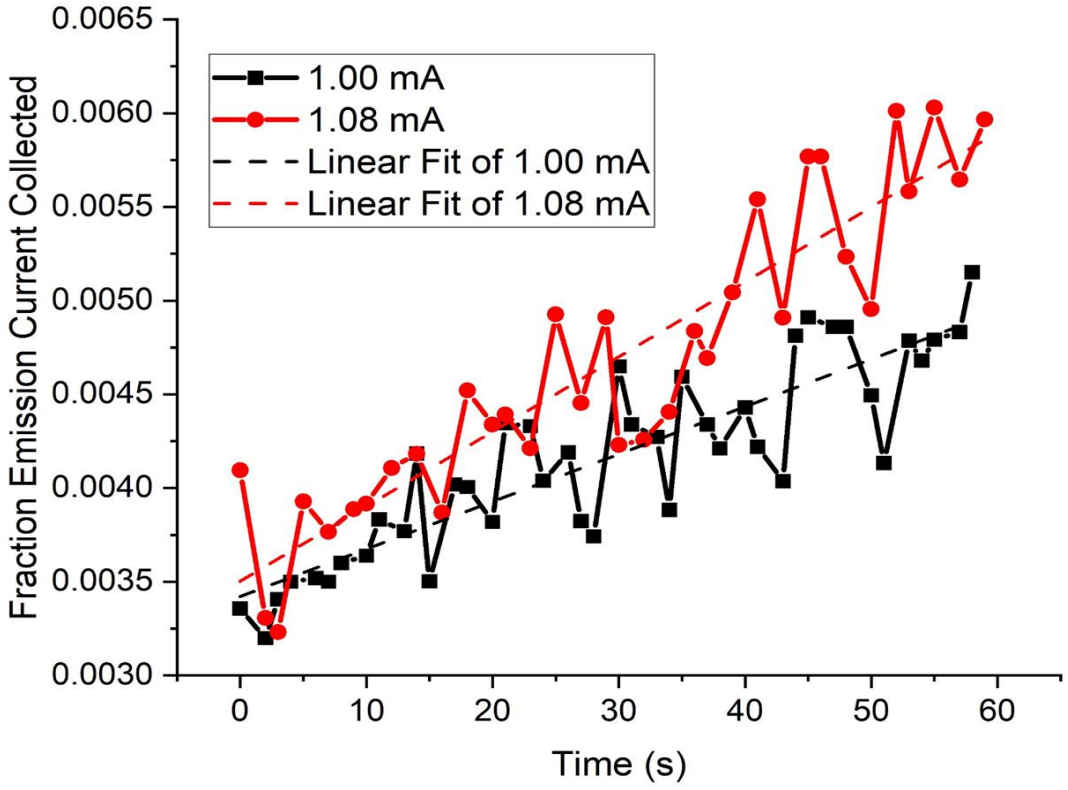


Figure 19: Normalized Faraday cup current versus time demonstrating a steeper slope at higher emission current, which is indicative of a higher carbon sublimation rate.

current versus time plot.

By comparing the temperature and normalized Faraday cup current of various exposure currents, three different regimes for the foils can be observed and are shown in Figure 20a. First we expose a fresh foil to a 200 μA continuous wave (CW) emission current. At this current, the foil rapidly graphitizes and the increased emissivity causes a decrease in temperature. The absolute temperature measurement in this early region isn't reliable due to the changing emissivity. The temperature decrease saturates near 300 seconds and during this stage, the normalized Faraday current only slightly increases. We then increase the emission current to 300 μA, and while the temperature instantly rises ~ 90 K, the normalized Faraday cup current initially equals the final value in region 1 (i.e. the fraction of emission to collected currents for the end of region 1 and beginning of region 2 are the same). The normalized Faraday cup current in region 2 increases and there is a slight concomitant decrease in peak temperature. The slope of the normalized Faraday cup current versus time suggests that sublimation rate is initially high and during the second 300 second exposure begins to taper and nears saturation at 600 s; the thinning in region 2 causes a net change of ~ 65% in the normalized Faraday current and an ~ 10 K decrease in temperature. In the third region, the emission current is increased again to 380 μA, which causes an instantaneous increase of ~ 120 K in temperature. During the 300 s exposure the temperature decreases significantly (~ 90 K) concurrent with an increase in normalized Faraday cup current,

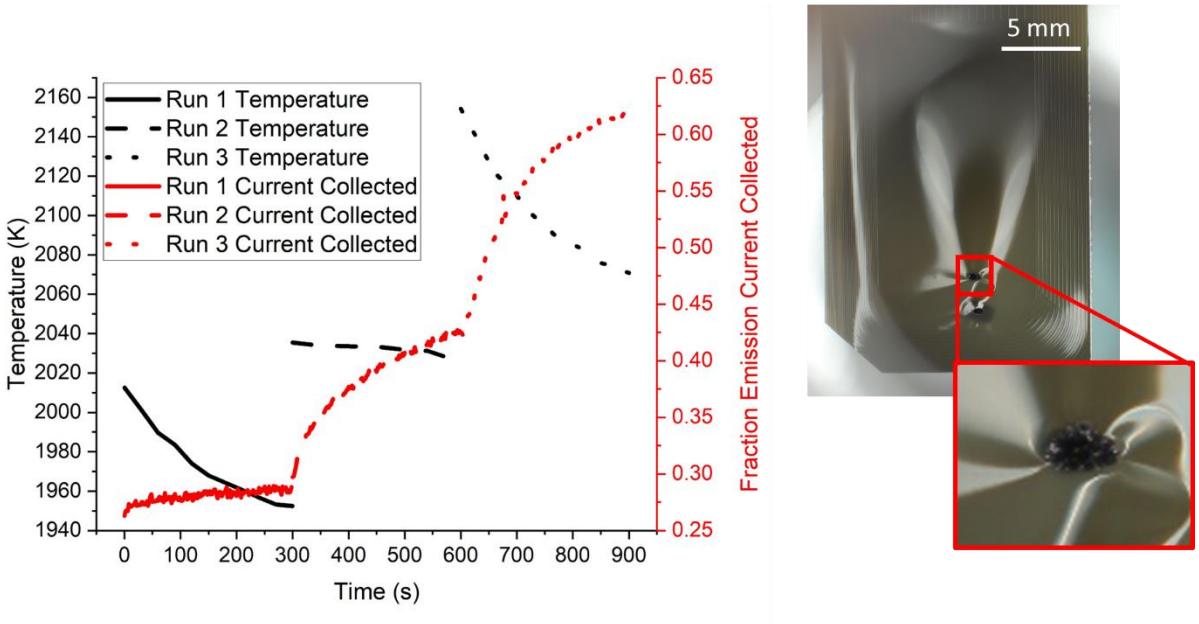


Figure 20: a) Temperature and normalized Faraday cup current versus time for 3 different runs (left). b) Photograph of the foil after the 3 runs (right).

indicating heavy sublimation and a potential hole formation in the film. Note the graphite vapor pressure is ~ $4x10^{-8}$ Torr at 2000 K, thus sublimation of the graphitized foil is reasonable in these electron exposure conditions. Figure 20b shows the NCD foil after irradiation. The graphitized region can be clearly seen along with the deformations caused to the surrounding foil.

Postmortem testing was also conducted to elucidate the changes occurring to the nanocrystalline diamond foils. Emissivity measurements were conducted using a black body source as described in section 3.2.2.2 of Barrowclough's dissertation[35] and used for FLIR measurements. Raman spectra were taken in the relative regions shown in figure 21. The results show the central area 1 has sharp peaks at 1325 and 1585 cm^{-1}, which are associated with strong crystalline graphite and diamond vibrations, respectively. Additionally, peaks around 2700 and 2900 cm^{-1} are observed and are similar to peak patterns found in carbon nano-onions [87]. The second region has discernible peaks at 1335 and 1595 cm^{-1} which are broader than region 1, suggestive of potentially a more disordered material with defects [88] or a shift to smaller grain size of the sample [36]. Region 3 is an unexposed region and has two peaks at 1330 and 1565 cm^{-1}; the peaks are broad and indicative of the nanocrystalline diamond and an amorphous phase of carbon. Additionally, SEM imaging was conducted on these foils in order to directly observe potential failures and can be seen in figure 21. Holes in the foil caused during exposure are seen in the SEM images. This helps to determine that the cause of the failure is sublimation rather

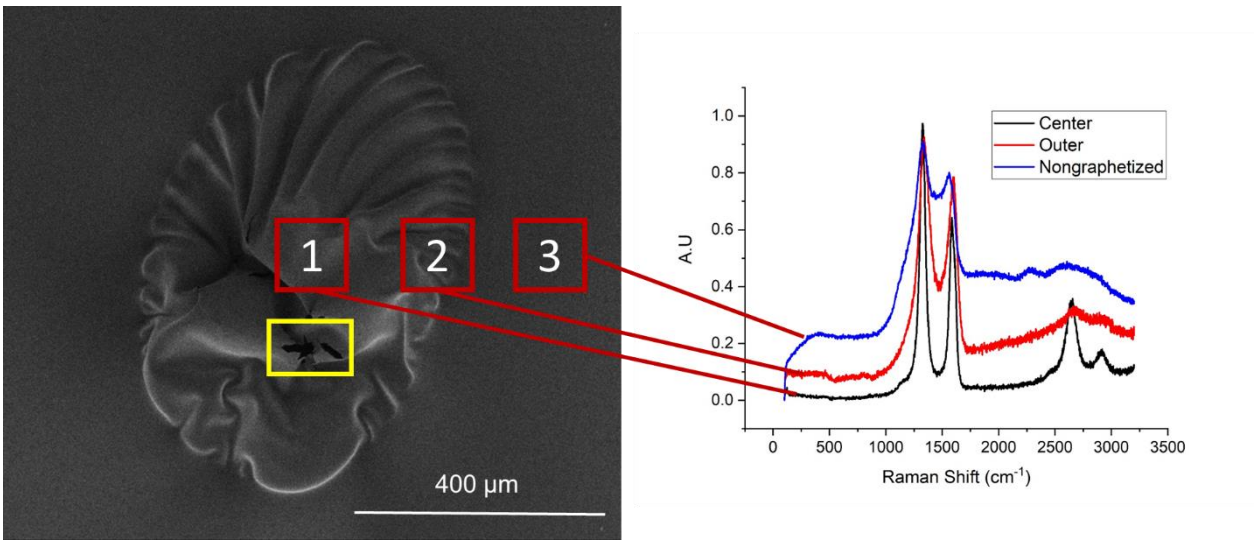


Figure 21: SEM image of an exposed spot (left) and the corresponding Raman spectra (right). Example of holes in the foil (boxed in yellow).

than mechanical failure. Hole formation, noted in the yellow box in the figure 21 SEM, is attributed to excessive sublimation at the hot spots of the electron gun, as there is no visible stress accumulation in the area. However, large wrinkles have also formed along ridge lines in the exposed area. These wrinkles are attributed to mechanical stress accumulation caused during graphitization.

Beam line temperature data was obtained from the SNS with an accuracy of ±2.5%. With a 1.4 MW, 1 GeV beam the peak temperature was measured to be 1750 K. This was taken using a dual band pyrometer and is an emissivity independent reading[49,50]. The beam power was gradually increased in steps up to 1.4 MW. The temperature versus time profile is plotted in figure 22. The data has an artificial dip when the temperature goes below 1200 K, which is an artifact of the measurement method. 1750 K measurements were obtained on the FTS with a current of 750 μA, which is also shown in figure 22. The FTS measurement was conducted during a 10 second exposure on a spot that was first conditioned with 10 s sequential exposures of 250 and 500 μA beams. The cooling curves differ between the two beams and is likely an effect of the difference in the beam profiles and sizes. Thus, while the peak temperature achieved is the same, larger spot sizes can result in a slower thermal decay (see supplemental information for details).

To correctly model the electron beam heating and equate the FTS and SNS beams, we measured the spot size/shape of the electron beam to determine the peak current density. This value was determined by blocking the

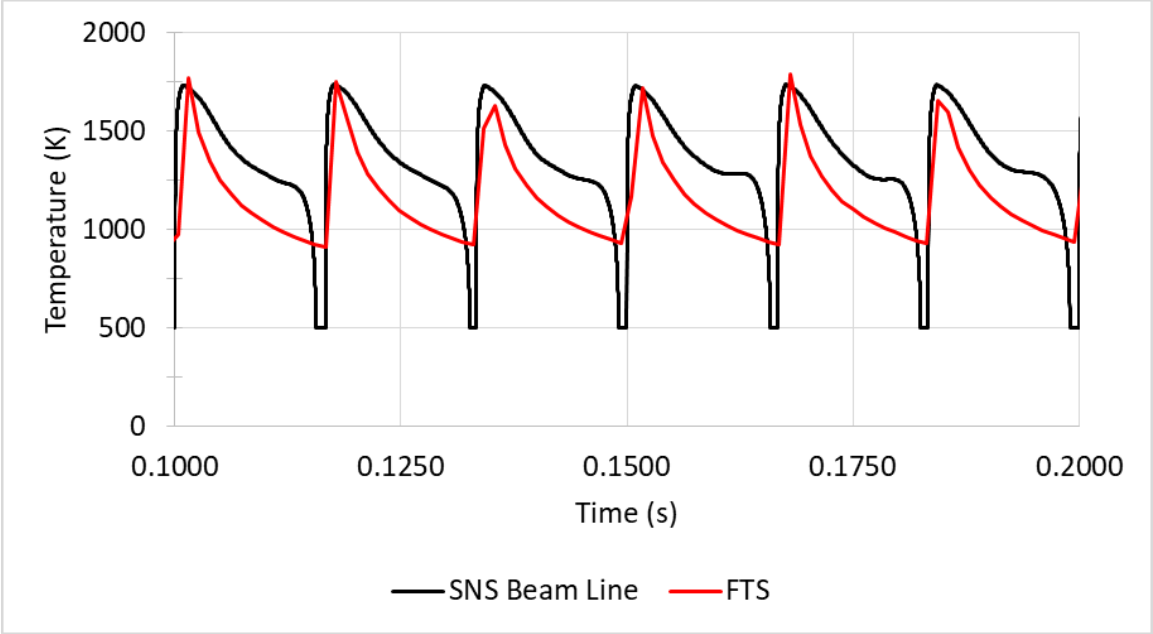


Figure 22: Temperature data for the 1.4 MW, 1.0 GeV SNS beam (black) and the 750 μA FTS electron beam (red).

beam from the Faraday cup with a piece of titanium and slowly raising the titanium in 25 μm steps to progressively expose the beam to the Faraday cup. The derivative of this data was taken with a Savitzky-Golay filter and the projection of a Gaussian ring-shaped beam was used to fit the profile. This determination was made with the assumption of a radially symmetric beam. Radial symmetry is a reasonable assumption based on phosphor screen images taken at low intensity which cannot be used to determine the profile at higher intensities. We used the following model for a Gaussian ring beam profile

$$f(x,y) = \frac{2\sigma^2}{\sqrt{x^2+y^2}}\left(\exp\left(\frac{2R\sqrt{x^2+y^2}-x^2-y^2-R^2}{2\sigma^2}\right) - \exp\left(\frac{-2R\sqrt{x^2+y^2}-x^2-y^2-R^2}{2\sigma^2}\right)\right)$$

where σ is the standard deviation and R is the Gaussian ring radius. This allowed an estimation of the beam shape to be extracted with a ring radius of 220 μm and a standard deviation value of 75 μm. The beam profile peak current densities of the FTS are estimated from this beam shape.

COMSOL simulations were performed by emulating an electron beam at 30 keV, varying current, and the beam shape parameters previously determined. In order to estimate the percentage of deposited beam energy that goes into heating (ε), a continuous wave (CW) experiment was first simulated. A CW beam was chosen to make sure that good correlation was obtained between experimental and simulated data before emulating the pulsed beam. Comparison with a CW beam also verifies the correct thermal conductivity has been assumed

for this temperature range, as shown in figure 23a. Using the temperature dependent physical parameters, electron beam profile discussed above, and an integrated beam current of 200 μA, the CW thermal excitation curve was best fit with a simulation assuming an ε of 74%. An ε of 74% is not unreasonable due to the many inelastic channels through which electrons can lose energy. In a recent study, the heating due to inelastic energy loss was estimated in ultrathin membranes (22-61 nm), and the accuracy of measuring the inelastic energy loss was on the order of 20% consistent with our estimation of ε [89].

Using the determined ε for the CW experiment and simulations, pulsed simulations were conducted using a 750 μA, that matched the SNS peak temperature, and 1 mA beams. Both simulations were pulsed at 1 ms and 60 Hz (6% duty cycle) and compared against experimental data, shown in figure 23b and 23c, respectively. A peak current density of 1.98 mA/mm^2 is realized in the 750 μA and 2.64 mA/mm^2 in the 1 mA experiments based on the beam profiles. In the 750 μA experiment versus simulation comparison the simulated foil has a maximum temperature of 1800 K and is very close to the experimentally observed peak temperature of 1746 K. For these exposures there is no experimentally observed sublimation in agreement with the graphite vapor pressure curve [90]. The 1 mA beam simulation results in a peak temperature of 2160 K, which is also in good agreement with the average peak experimental temperature of 2080 K. This difference between simulation and experiment can be partially due to sublimation that occurs in the foil or, of course, standard error

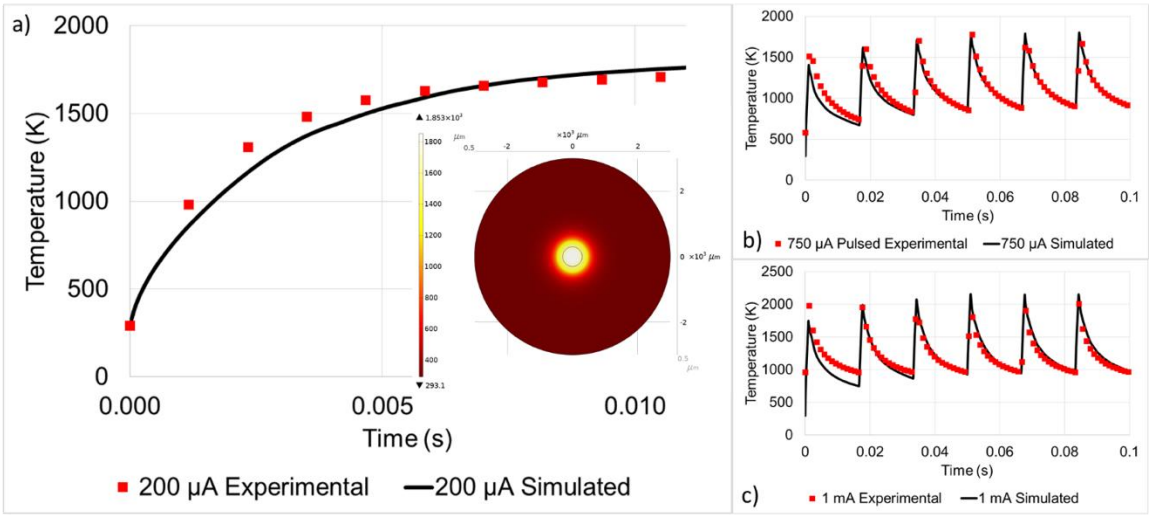


Figure 23: A) 200 µA continuous electron beam experimental and simulated comparisons. Inset graph shows simulated heat profile on foil. B) 750 µA pulsed electron beam experimental and simulated data. C) 1 mA pulsed electron beam experimental and simulated data.

in the experimental versus simulations values used. As the sample sublimes, the thickness decreases and the energy deposited decreases which, as shown in fig. 20, decreases the effective temperature of the foil. The material loss is not accounted for in the simulation and could cause discrepancy with the experimental results.

Foil degradation was observed during the 1 mA experimental FTS runs as the normalized Faraday cup current increased during exposure and as-revealed via post mortem pictures of the foil. The 750 μA beam showed no signs of failure and was determined to be a stable regime. By using the SNS design beam parameters, the 750 μA and 1 mA beams correspond to an SNS peak energy deposition density per pulse of $4.26*10^{10}$ MeV/mm^2 and $5.68*10^{10}$ MeV/mm^2, respectively. We used ORBIT simulations of an optimized injection to estimate the proton and electron hit number density on the foil during well-tuned SNS operation and then use tabulated energy deposition values to estimate the peak energy density per pulse. For a 362 ug/cm^2 foil the predicted peak energy deposition per pulse is $1.75*10^{10}$ MeV/mm^2, 2.43 times lower than the 750 μA case. Based on this, the SNS should safely be able to run 3.36 MW at 1.0 GeV using foils currently used during operation. Simulations of the 2.8 MW, 1.3 GeV scenario assumed for the future upgrades to the facility produce peak energy deposition of $2.93*10^{10}$ MeV/mm^2, 1.45 times lower than the 750 μA case. At 1.3 GeV powers of 4.06 MW should also be comfortable. The 1 mA limit corresponds to powers of 4.55 MW and 5.43 MW at 1.0 GeV and 1.3 GeV

respectively, but this represents the regime where we see foil failure. One should note the foil thickness assumed here is slightly larger than necessary but corresponds roughly to the current operational situation. The thickness could be reduced another 10% or more if more margin is needed. Scaling the power in this way is reasonable, but requires some caveats as the actual peak power deposited depends on many parameters including the injected H^- and recirculating proton beam profiles which can change during tuning of the beam. However, as demonstrated in the FTS data, the equivalent energy deposition density values can be used to determine when the foils are approaching an unstable regime where foil failure will occur.

To understand the sensitivity of the COMSOL simulation results, a sensitivity analysis was conducted. For the baseline of this analysis a 750 μA beam with an ε of 74%, ring radius of 220 μm, Gaussian standard deviation value of 75 μm, and graphitized emissivity of 0.9 was used. The ring radius, Gaussian standard deviation value, current, ε, emissivity, and thermal conductivity were each individually increased by 10% and the resultant peak temperatures were simulated and compared. Table 2 is a summary of the changed simulation parameters and the resultant simulated peak temperature and the change in peak temperature. Of course, changing the current and ε have the same effect of linearly increasing the energy deposited and this had the strongest effect on temperature. The beam's ring radius had the next largest effect. The rest of the changed variables had minimal impact and resulted in less than 23 K (1.3%)

Table 2: Sensitivity analysis for COMSOL simulation parameters

current μA	epsilon	ring radius μm	ring sigma μm	emmissivity	Thermal Conductivity W/(m*K)	Peak T K	Delta Peak T K
750	0.74	220	75	0.9	Normal	1801	0
825	0.74	220	75	0.9	Normal	1908	107
750	0.814	220	75	0.9	Normal	1908	107
750	0.74	242	75	0.9	Normal	1695	-106
750	0.74	220	82.5	0.9	Normal	1778	-23
750	0.74	220	75	0.99	Normal	1779	-22
750	0.74	220	75	0.9	1.1(Normal)	1779	-22

deviation in the peak temperature.

In addition to helping to understand the limits of what SNS standard foils can withstand, the COMSOL model will also be able to assist in future improvements and revisions to foils. By being able to rapidly simulate different geometries and changing physical properties in the charge injection stripper foils, this method can help to direct foil improvements in the most beneficial directions. Fast simulations coupled with previous literature on varying NCD growth recipes and the resultant properties, will hopefully lead to improved future stripper foils.

Conclusion

An electron beam mimic of the charge exchange injection stripper foil has been developed and the equivalent power density of the H- ion and the electron beam has been calculated. An equivalent beam of 30 keV electrons penetrating a nanocrystalline diamond stripper foil has been experimentally measured and simulated via a COMSOL thermal model. The Faraday cup and FLIR IR camera show indications of sublimation that can be tracked throughout the exposure of the foil. Postmortem testing was also conducted in order to give insight into the changes that occurred during the stripper foils' exposure to the electron beam. The methods developed and used in this paper allow for testing of stripper foils on a much faster time scale than would be possible in the main SNS beamline. Utilizing these methods while varying synthesis parameters for the nanocrystalline diamond growth, will lead to a better understanding and potential improvement in stripper foil failure limits.

Acknowledgements

This work was supported by the DOE office of Science User Facilities. LS, LW, and NE are supported through funding for the Spallation Neutron Source. SNS is managed by UT-Battelle, LLC, under contract DE- AC05-00OR22725 for the U.S. Department of Energy. Foil synthesis, certain post-mortem testing, and modeling were conducted at the Center for Nanophase Materials Sciences, which is also a DOE Office of Science User Facility. Additionally, the authors would like to thank Jeff Holmes for simulations of the SNS beam/foil interaction, and Willem Blokland for operational data from the SNS foil pyrometer.

Supplemental

A 3D time dependent model was built in COMSOL of a 1 μm thick cylinder with a radius of 3000 μm to simulate a NCD foil. In the center of the NCD cylinder another cylinder with 350 μm radius was created in order to represent the graphitized interaction region with the electron beam. Two different materials were used in the model for the graphitized and ungraphitized volumes. Both of these materials had the same material properties except for the emissivity and thermal conductivity. A fine physics controlled mesh was generated for the entire volume.

In order to determine the beam shape for COMSOL simulation, a Gaussian ring equation was used. The Gaussian distribution is defined by the equation $f(x,y) = A \cdot \exp\left(-\left(\frac{(x-x_0)^2+(y-y_0)^2}{2\sigma^2}\right)\right)$ with a ring radius R where R =

$\sqrt{x_R^2 + y_R^2}$. In the Gaussian formula σ determines the width of the bell shape while A is a normalizing term that determines the amplitude. The ring equation was then integrated in order to get a summed profile at every point in the 2d grid. This resulted in the equation $f(x,y) = \frac{2\sigma^2}{\sqrt{x^2+y^2}}\left(\exp\left(\frac{2R\sqrt{x^2+y^2}-x^2-y^2-R^2}{2\sigma^2}\right) - \exp\left(\frac{-2R\sqrt{x^2+y^2}-x^2-y^2-R^2}{2\sigma^2}\right)\right)$. The parameters R and σ in this equation were varied to obtain a best fit of the 1D line integral of the resulting function along the y axis taken numerically was to the 1D profile measured with the scraper. The normalized equation was then used in COMSOL.

Multiple global functions were created in order to emulate both the pulse profile and the beam profile. A rectangular function was used from 0 to 1 and periodically repeated to get the desired pulse dwell time and frequency. A function for a 2d Gaussian ring was estimated and normalized based on previous experimental readings of the electron beams profile. Additionally, a depth energy loss function was created from the results of the Monte Carlo simulations. Two different thermal conductivity functions were created. The first was a piecewise function described in the main text and the second was estimated for polycrystalline graphite. Lastly, a temperature dependent heat capacity function was determined from previous literature as described in the main text.

COMSOL's heat transfer in solids was used in order to simulate heat deposition, dispersion, and radiation. Both sides of the foil were set as diffuse surfaces in the model, with the graphitized region having an emissivity of 0.9 and

the rest of the foil having an emissivity of 0.14 (nanocrystalline diamond). The graphitized region was set as a heat source in the model. The heat source was determined by the set beam current, normalized beam profile, and depth energy loss function. The polycrystalline graphite thermal conductivity was used for the inner graphitized cylinder, while the piecewise function was used for the surrounding NCD foil. Lastly, explicit events were input for the duration of every pulse. This is to tell COMSOL rapidly varying events are occurring so the simulation can adjust its time steps accordingly.

To examine the differences between the SNS and FTS thermal profiles, cool down curves were simulated. Three different radius spots were equally heated to 1750 K and allowed to cool. The cooldown curves are shown in figure 25.

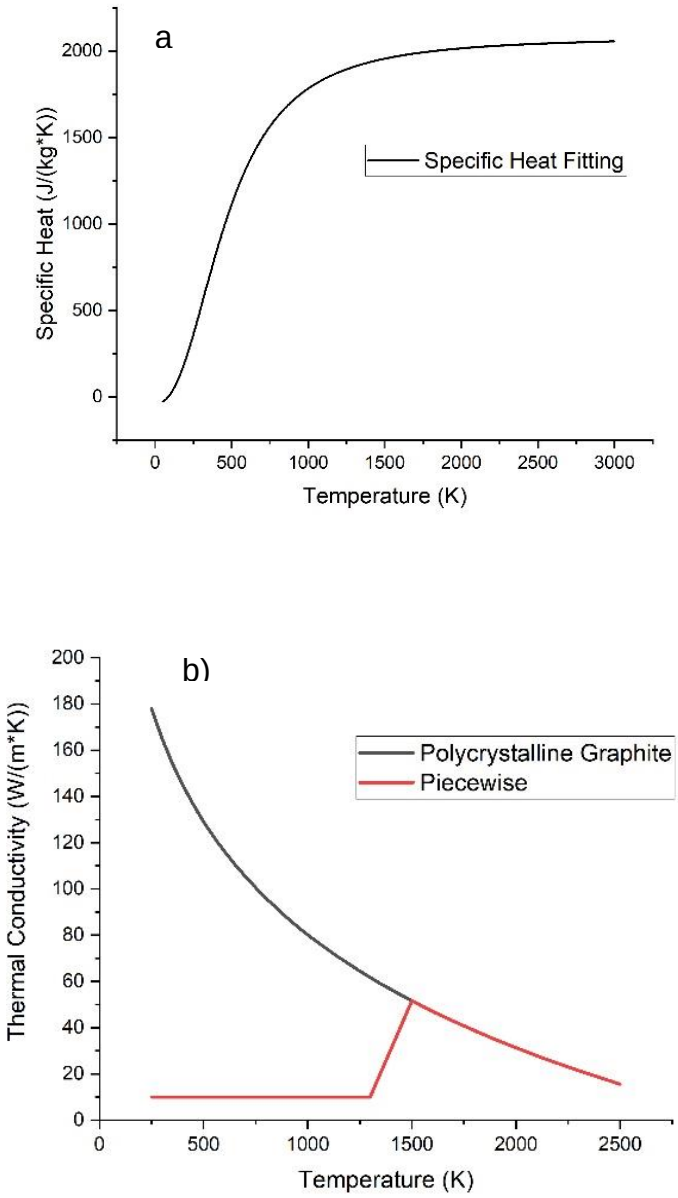


Figure 24: Supplemental: a) Specific Heat capacity function used in simulations. b) Thermal conductivity function used in simulations.

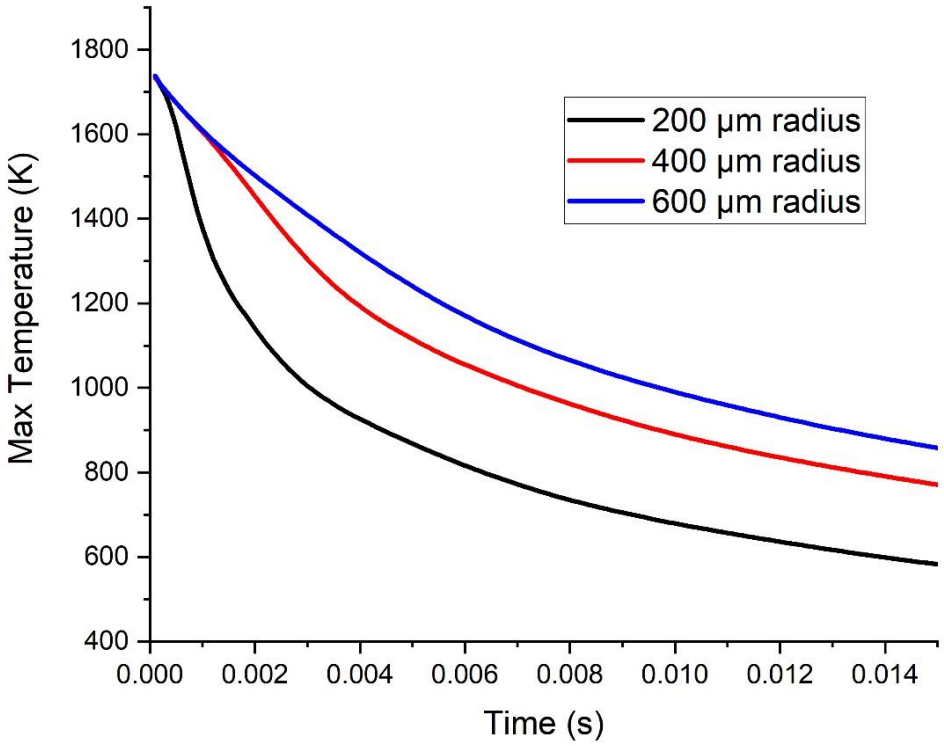


Figure 25:Supplemental: Simulated thermal decay of various size spots each fixed at the same peak temperature, but varying decay curves where larger areas decay more slowly.

CHAPTER III
COMPARISON OF µCD AND NCD STRIPPER FOILS

Abstract

Carbon foils are regularly used for charge exchange injection in beamline accelerators. As beamlines increase the power in their beam, the thermal durability and longevity of the stripper foils become critically important to maintaining larger beamline operating times. In this study we examine the current Spallation Neutron Source nanocrystalline diamond stripper foils and compare them to microcrystalline alternatives. To do this, an electron beam mimic is used to emulate the thermal load of the SNS beam on the test stripper foils. The tested foils are analyzed based on the resultant temperature of the film and the percentage of electron beam collected by the Faraday Cup during beam exposure. Additionally, postmortem testing was conducted to determine the emissivity, vibrational structure via Raman spectroscopy, and surface morphology data on the foils.

Introduction

Stripper foil lifetimes have become increasingly important as beamlines reach for higher operating powers. In cases such as the Spallation Neutron Source (SNS), where a power upgrade is currently being scheduled, thermal robustness of charge exchange injection foils is of critical importance. Extending foil lifetimes will improve the limiting factor in beamline operating time and reduce the need for increased exposure to hot areas in the beamline. Currently, carbon is the most commonly used material for stripper foils due to its low atomic number and its desirable thermal properties, although alternative materials are

used. Many beamlines use graphitic or amorphous carbon stripper foils, whereas SNS currently uses a nanocrystalline diamond (NCD) stripper foil. It has improved mechanical stability when compared to standard carbon stripper foils, which usually require wires to hold them in place. However, the SNS NCD foils currently reach temperatures in the 1700 K range during normal operations. It is of concern that the increased beam power from the Proton Power Upgrade project could push these foils above 2000 K, where sublimation starts to limit the lifetime and stripping efficiency of the foils. In order to increase the thermal load these foils can take, a new type of polycrystalline foil is examined in this study and compared against the standard FTS foils.

Microcrystalline diamond foils were chosen due to their increased thermal conductivity over NCD. While this could have limited effect on continuous wave beamlines due to thermal radiation being dominant in the high temperature regime, the SNS beamline is pulsed with a 6% duty cycle. This leaves the SNS beamline with a ~15.6 ms cooldown time between pulses. Increased thermal conductivity should become increasingly important in this cool down regime, due to the foil not reaching an equilibrium temperature during the 1 ms dwell time.

Examinations of stripper foils have been conducted for multiple different materials. These materials include liquid Li [9], helium gas [8], graphene [6,69], carbon foils [70,91], and polymer coated carbon foils [92]. In this study we examine polycrystalline diamond foils for charge exchange injection. We have previously examined the SNS nanocrystalline diamond films [68] and will expand

upon the previous research by examining three additional types of polycrystalline diamond films.

Methods

μCD and NCD foils were fabricated at the Center for Nanophase Material Sciences using a DiamoTek 700-6 microwave plasma CVD system for testing in the FTS. Three different types of μCD foils were tested along with the NCD foil currently used in SNS. A mixture of CH_4, H_2, and Ar were used in foil growth to produce different growth conditions and grain structure. The SNS standard NCD foil is grown with 2.45% CH_4, 90% Ar, and 7.55% H_2 at a pressure of 105 Torr and power of 1330 Watts. μCD-1 was grown with 1% CH_4 and 99% H_2 at a pressure of 40 Torr and power of 1620 Watts. μCD-2 was grown with 20% Ar, 1% CH_4, and 79% H_2 at a pressure of 45 Torr and a power of 1200 Watts. The last sample, μCD-3 was grown with 40% Ar, 1% CH_4, and 59% H_2 at a pressure of 40 Torr and a power of 1200 Watts. A table of the growth conditions for each sample is presented in table 3.

The μCD film recipes were chosen to vary both grain size and grain boundary composition. μCD-1 has no Ar and a high proportion of H_2 during growth. The high H_2 composition encourages etching of graphite and amorphous carbon during growth, leaving large grains with intergranular voids in the grain boundaries [51]. μCD-2 and μCD-3 were used in an attempt to keep larger diamond grains, while allowing non-diamond carbon deposition between grains. This is an attempt to fill the intergranular voids present in the μCD-1 sample and

Table 3: MPCVD growth conditions for the various samples.

Sample	MPCVD Conditions					Areal Density ($\mu g/cm^2$)
	Pressure (Torr)	Power (Watts)	Ar%	H_2%	CH_4%	
NCD	105	1330	90	2.45	7.55	401
µCD-1	40	1620	-	1	99	391
µCD-2	45	1200	20	79	1	387
µCD-3	55	1200	40	59	1	400

enhance the in-plane thermal conductivity of the samples. The as deposited Raman spectra can be seen in fig. 26. The NCD spectra shows a peaks around 1332 and 1574 cm^{-1}. The 1332 cm^{-1} is broad and is attributed to the diamond phase [64]. Additionally, the 1332 cm^{-1} peak could also be from the disordered D peak in graphite [93]. The 1574 cm^{-1} is from a shifted graphite D peak which is usually at 1583 cm^{-1} [94]. This suggests a mixture of graphite and diamond in the sample. µCD-1, µCD-2, and µCD-3 all show signs photoluminescence from C:H bonding causing their background intensity to increase with increasing cm^{-1} [65]. Each of the µCD samples shows a peak at 521 cm^{-1} that is attributed to the Si substrate [95]. Unfortunately, photoluminescence makes the µCD data harder to interpret, however, slight peaks are observed at 1338 cm^{-1} in all 3 samples suggesting either diamond or disordered graphite phase. The 1338 cm^{-1} is less prominent in the µCD-3 sample suggesting a lower fraction of diamond or disordered graphite in the sample. All 3 µCD samples also show a broad peak from 1500 to 1600 cm^{-1}, which is similar to previous literature that was attributed to a combination of graphite and distorted sp^3 carbon [64].

SEM images of the as-deposited samples are shown in fig. 27. Small grain sizes are seen in the NCD sample. The grains in the µCD-1 sample are larger and in a columnar structure. This contrasts with the µCD-2 and µCD-3 samples which show larger grains than the NCD sample, but have no ordering and do not seem to be columnarly grown. The random crystallites shown in the µCD-2 and

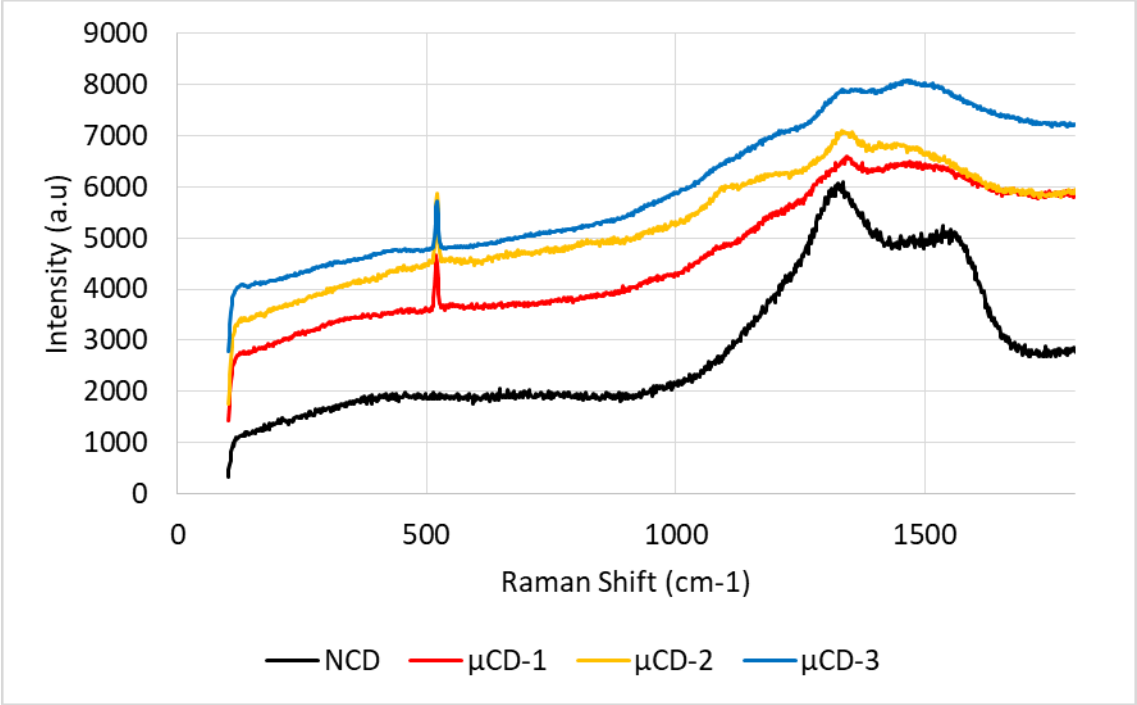


Figure 26: Raman spectra for un-graphitized portions on the samples.

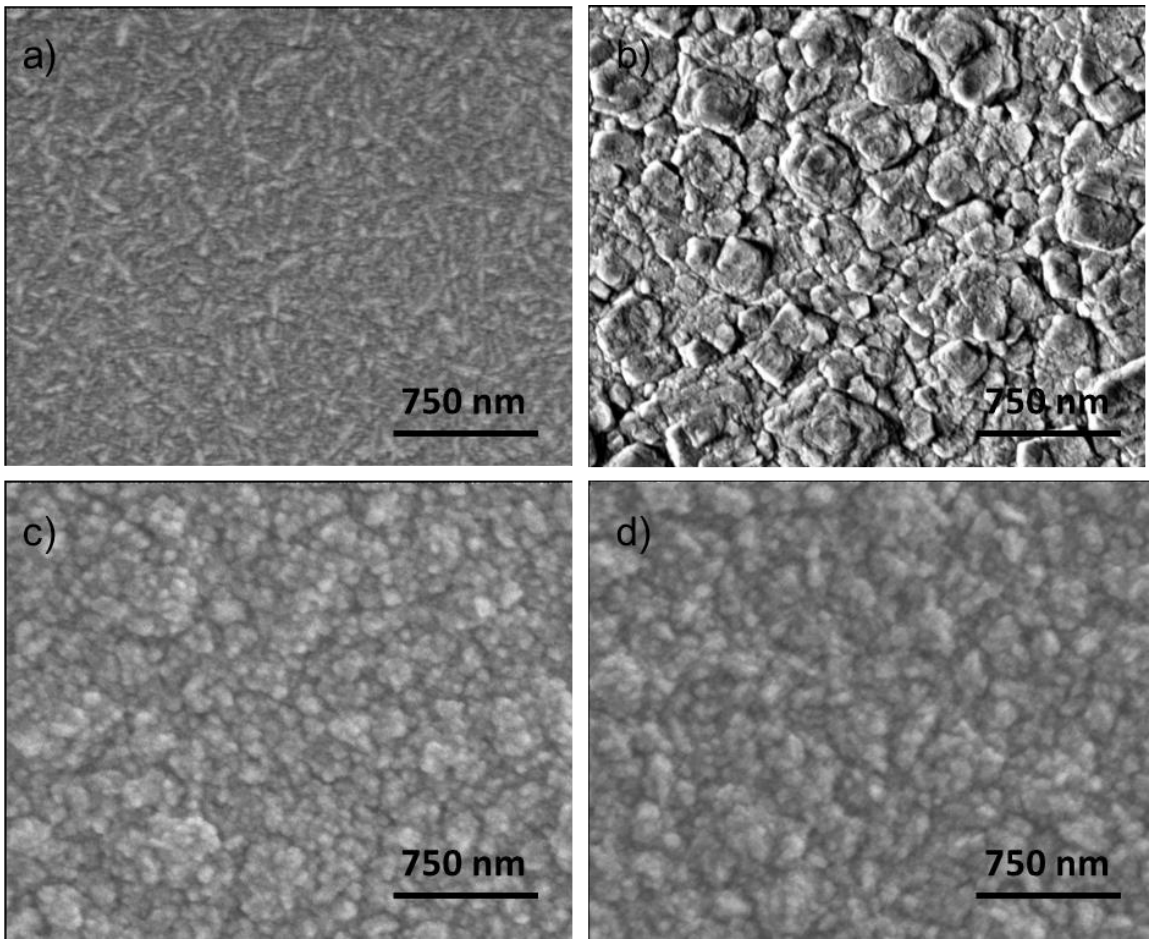


Figure 27: SEM images of the samples NCD (a), µCD-1 (b), µCD-2 (c), and µCD-3 (d).

μCD-3 samples are due to the re-nucleation encourage by the Ar present during growth.

The sample foils were deposited to an areal density of approximately 360 μg/cm^2. From a previous study, μCD-1 was shown to have an approximately 6 times higher thermal conductivity than the NCD sample at room temperature[51]. There is no data for the thermal conductivity of samples μCD-2 and μCD-3 for comparison. The foils consist of a 17 mm by 45 mm foil deposited onto a Si chip with corrugations along the outside edge for improved mechanical stability. 17 mm by 30 mm of the foil is free standing after the bottom 30 mm of Si is etched away. Both sets of foils are mounted inside of the foil test stand (FTS) for comparative testing on a multi-motion feed through.

Measurements

The FTS consists of an electron gun, multi-motion feedthrough, residual gas analyzer, faraday cup with a limiting aperture, FLIR camera, pressure gauge, and a video camera. In depth descriptions of the instruments and their orientation can be found in previous literature [68]. Foils mounted inside of the FTS are irradiated by the electron gun with the vacuum pressure staying in the 10^{-8} torr range. The foil scatters the beam and a portion of the remaining beam strikes the limiting aperture and is measured. The amount of beam that strikes the limiting aperture is dependent on the areal density of the foil it is interacting with. This means that as a foil sublimes and the areal density decreases, the beam dispersion decreases and a larger portion of electrons strike the limiting aperture.

G4 beam line is used to model the beam dispersion and can be compared against experimentally measured currents to approximate the change in the foils areal density and thickness [96]. Similar to the limiting aperture current, the FLIR temperature measurements will also scale with areal density. As the foil thins, the electron beam interacts less with the foil and deposits less energy, resulting in a reduced temperature on the foil. Due to the limiting aperture and FLIR measurements scaling with the foil's areal density, they are the key indicators of sublimation or foil failure during irradiation.

After irradiation, foils are tested for their emissivity by using a black body source. The black body source is set to temperatures of 673, 873, 1073, 1273, and 1473 K with the foil is placed as a filter between it and the FLIR camera. A transmission value is then determined at multiple temperatures for the graphitized and ungraphitized areas of each foil. This process has been described previously [35]. Additionally, Raman spectra of the graphitized and ungraphitized areas were conducted. Lastly SEM images were taken of the foils irradiated portions.

Simulation

Simulations of the NCD and µCD-1 foils were conducted using COMSOL Multiphysics in order to match the experimental results and give insight into potential future improvements to the foils. A stopping power value for a 30 keV electron beam was used in the estar database to determine the energy deposition into the foil. The beam profile is one of the most important factors in

determining the current density of the electron beam. The electron beam was focused into the faraday cup and the edge of the foil was lowered in 50 μm increments into the beam. This gave the beam current percentage as a function of the beams y coordinate. This was matched to a Gaussian ring profile, which has been described previously[68], in order to obtain an accurate beam profile.

The thermal conductivity and specific heat of the foils were fit to functions that varied with temperature. The specific heat for both the μCD and NCD were fit to previous research for the range from 0 to 3000 K. For the thermal conductivities the NCD was set to 10 W/(m K) from room temperature to 1300 K. From 1300 to 1700 K the thermal conductivity was linearly linked to POCO graphite's thermal conductivity. Above 1700 K the thermal conductivity was linked to previous research on graphite. μCD's thermal conductivity was similarly modeled with a piecewise function. From room temperature to 1300 K the thermal conductivity was set to 60 W/(m K). From 1300 to 1700 K the thermal conductivity is linearly linked to the 1700 K graphite temperature. Above 1700 K the thermal conductivity is fit to graphite data the NCD sample was fit with. Additionally, the proportion of deposited energy that goes to heating, ε, was determined through matching simulation to experimental data.

Results and Discussion

FTS measurements were taken for the μCD and NCD samples with an electron beam pulsed at 60 Hz and 1 ms dwell time for a 6% duty cycle. This temporal profile was used to emulate the SNS beamline. The foils were

preconditioned by slowly ramping the irradiated spot from 130 μA to 330 μA in steps every 10 seconds over the course of 20 minutes. This was done to ensure a slowly conditioned spot, similar to the conditioning performed in the SNS beamline. After conditioning, the spots were exposed to a set of common currents (520 μA, 690 μA, 870 μA) to be compared with the other sample.

G4 beamline was used to get a gauge the relationship between the percentages of emitted beam that reaches the limiting aperture current with the thickness of the foil. The percentage of emitted beam versus foil thickness for graphite is shown in fig. 28. For this simulation, a simplified model of the test stand was used. An amorphous carbon foil was situated at a 30^{o} angle to and incoming electron beam with a flat distribution and +/- 1 mm full width. A Faraday Cup with a limiting aperture was situated 65 mm from the foil in line with the beam. The limiting aperture had inner and outer diameters of 1.5 and 11 mm, respectively. It is important to note that due to differences between the amorphous carbon used in the G4 simulation and the unknown makeup of the graphitized material in the irradiated spots, this data cannot be used to extract specific foil thicknesses. Instead, this data is used to examine and approximate relative changes in the foil thickness. As expected, the data demonstrates that as the thickness of the foil decreases the percent emission to reaching the limiting aperture increases.

The NCD sample data for the spots exposed to a 520, 690, and 870 μA beam are shown in fig. 29. Peak temperature plots include both the lower and

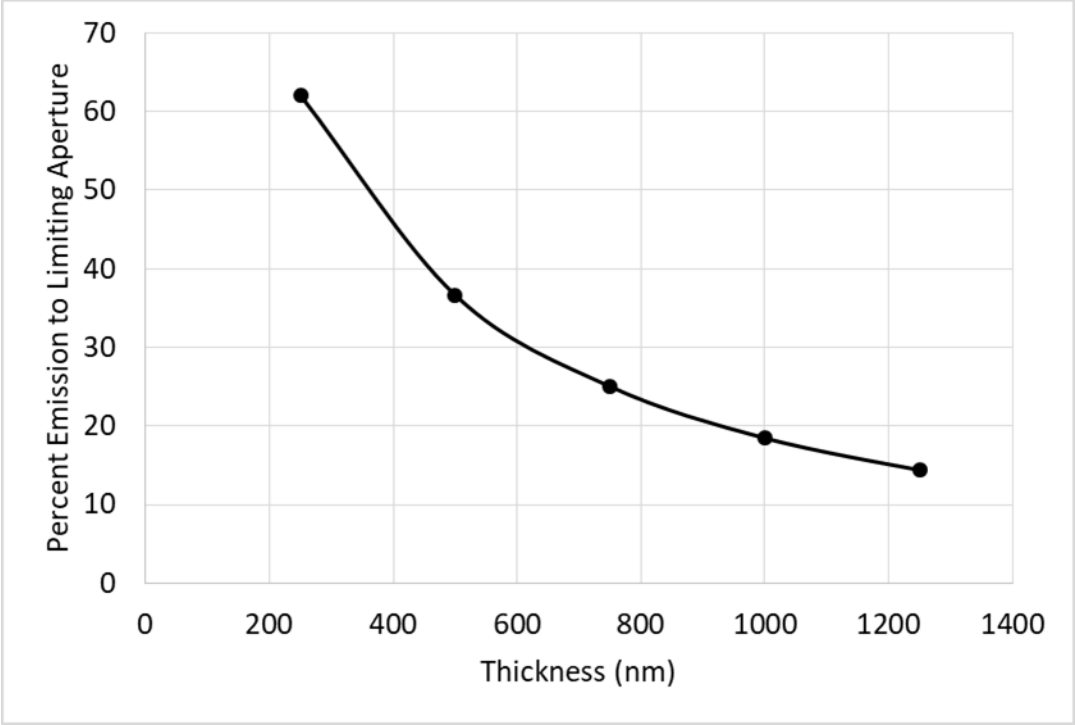


Figure 28: The percent of emitted beam captured by the limiting aperture after penetrating a foil versus foil thickness. This simulation was conducted with G4 Beamline for a graphite material tilted at 30^{o}.

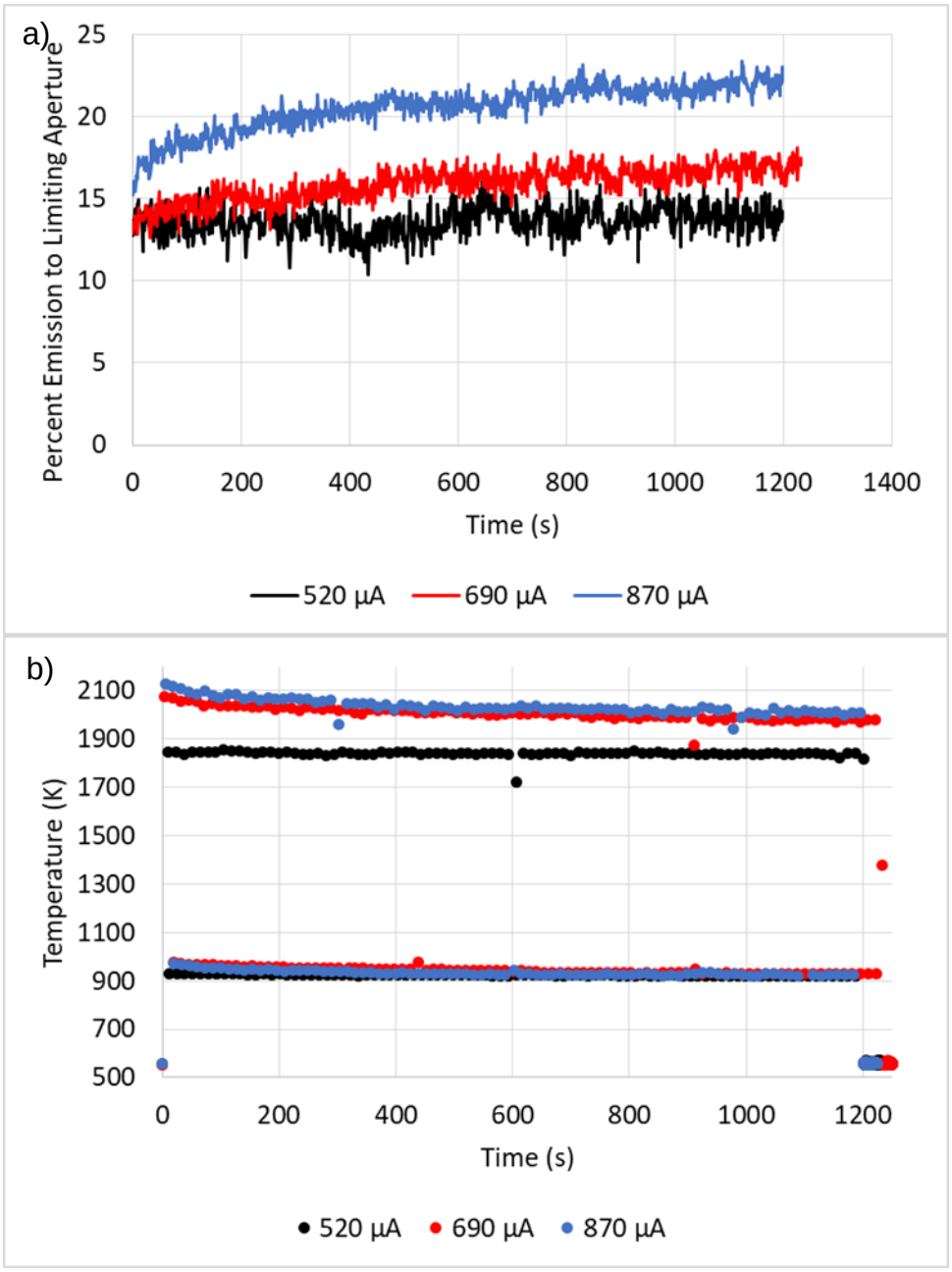


Figure 29: The NCD Faraday Cup (a) and temperature (b) measurements versus time for the 520, 690, and 870 µA exposed spots.

upper bound of the temperature envelope. This means the peak temperature is captured at the end of the pulse as well as the end of the cool down period. The 520 µA pulsed beam had a resultant peak temperature of 1854 K. This peak temperature increases to 2076 and 2119 K for the 690 and 870 µA exposures, respectively. The 690 and 870 µA exposures show signs of sublimation in the temperature readings. In both exposures, the peak temperature decreases over the course of the run until an equilibrium temperature of 1980 – 2000 K is obtained. The percent emission to limiting aperture data for the NCD sample showed similar sublimation signs. In the 520 µA exposure, the percent emission collected varied from 13 to 15% with no upward trend noticed during the 20-minute exposure. The 690 µA exposure increases slightly in the percent emission collected from 13 to 17%. The 870 µA exposure displays a very noticeable increase in the emission current collected increasing from 15 to 23% over the course of the exposure. For the NCD sample the 30 µA sample showed no signs of sublimation or foil failure, while both the 690 and 870 µA exposures indicate sublimation throughout the run.

The µCD-1 sample data for the exposures at 520, 690, and 870 µA are shown in fig. 30. The peak temperatures are 1707, 1887, and 2020 K for the 520, 690, and 870 µA exposures respectively. The 870 µA exposure was the only one to show a noticeable decrease in temperature during the run. The temperature dropped from 2020 K to roughly 1990 K, showing a similar trend as the NCD sample for decreasing temperature once the sample is heated to over 2000 K.

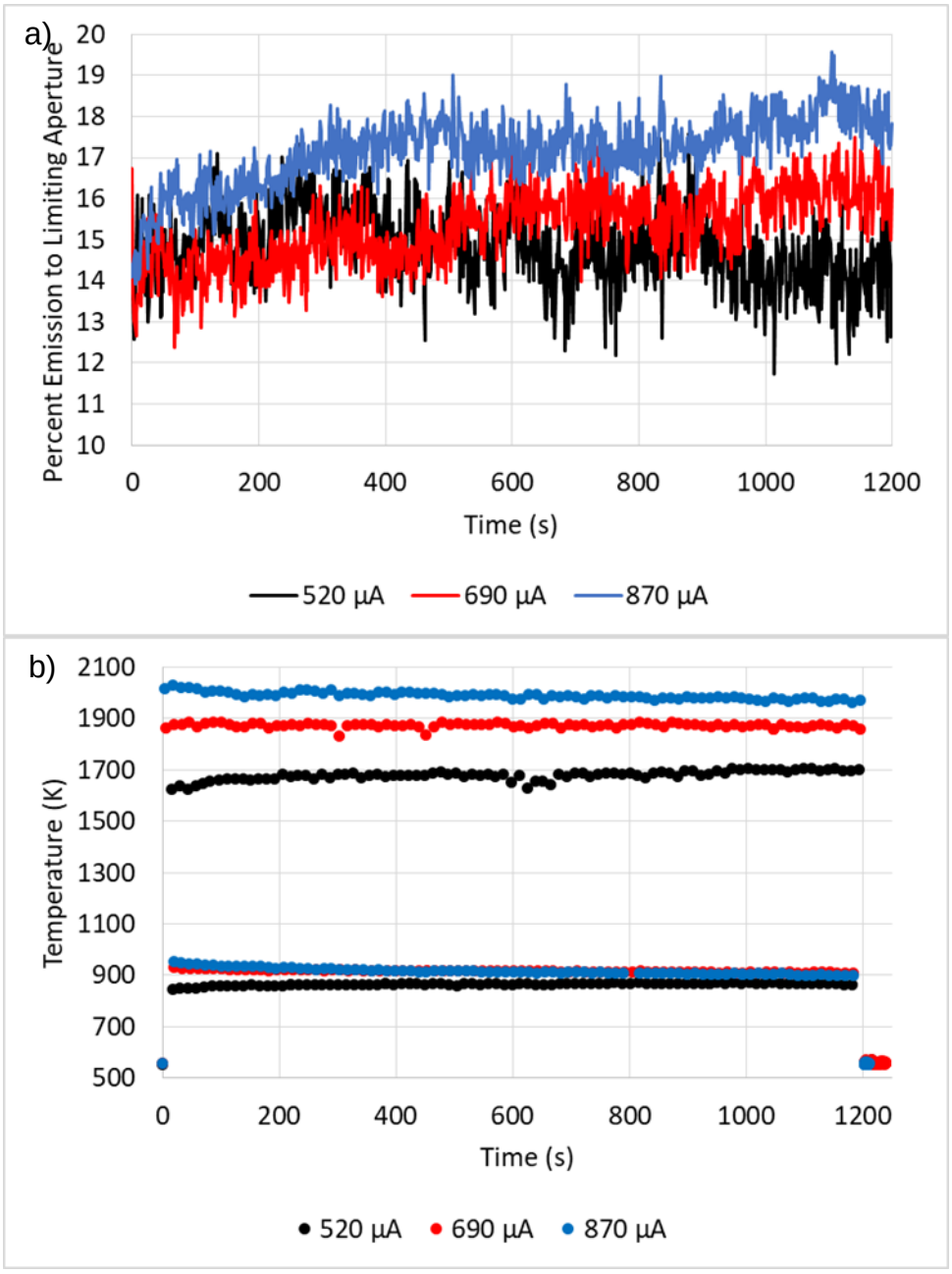


Figure 30: The µCD-1 Faraday Cup (a) and temperature (b) measurements versus time for the 520, 690, and 870 µA exposed spots.

The percent transmitted emission graph shows no noticeable signs of increase during exposure for the 520 μA test. The 670 μA test shows a slight increase throughout the course of the run from 13 to 16%. The increase in percent emission suggests a slight change occurred to the foil throughout the exposure, while the temperature data shows no indication of change. This could be due to a mechanical change to the foil, such as twisting, but does not seem to indicate sublimation. The 890 μA exposure shows a noticeable increase from 14 to 18% throughout the run. The increased percent emission coupled with the decrease in peak temperature suggest slight sublimation occurring throughout the run.

Figure 31 shows the data for the various exposures to the μCD-2 film. It is important to note that the μCD-2 sample was not consistently flat and showed signs of stress in the curl of the released foil. This caused the foil to oscillate heavily during exposure and can be a source of error and noise in the measurements. During the 520 μA exposure the maximum temperature observed was 1820 K with a slight increase in temperature over the first minute of exposure. This is likely due to increased oscillations of the foil during initial irradiation that settled further into the run. The percent emission for the 520 μA run showed no signs of sublimation and fluctuated between 10-13% throughout the run. The 690 μA exposure produced a peak temperature of 2010 K with a slight decrease in temperature observed at the beginning of the exposure. The percent emission also demonstrates a small rise throughout the run. This indicates slight sublimation occurring. There is an abrupt shift in both the

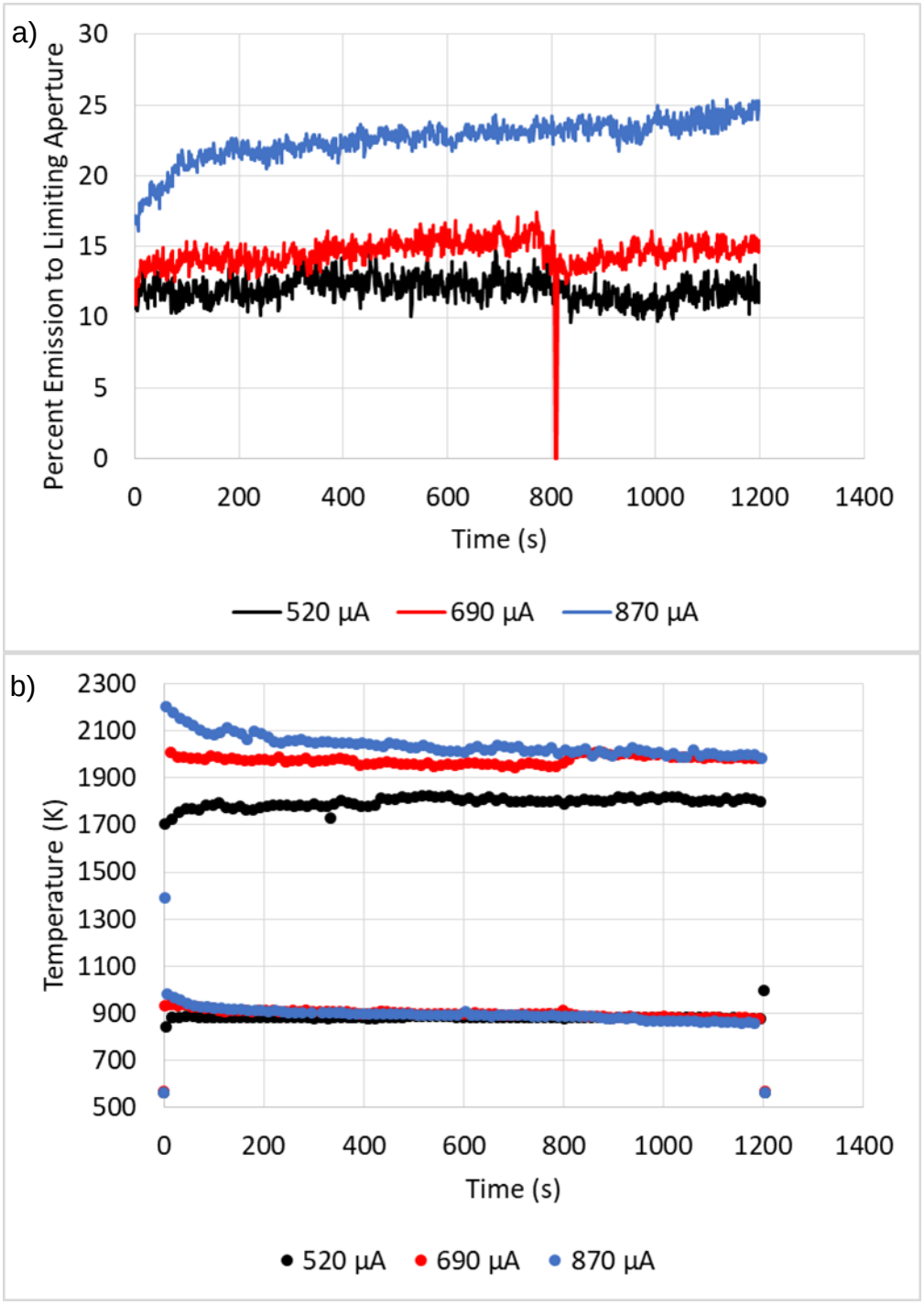


Figure 31: The µCD-2 samples' Faraday Cup (a) and temperature (b) measurements versus time for the 520, 690, and 870 µA exposed spots.

temperature and percent emission approximately 800 s into the run that is attributed to the foil shifting during exposure. Heavy sublimation can be seen in the 870 µA run with the max temperature dropping from 2200 K to ~ 1990 K throughout the 20-minute run. The percent emission also sees a heavy increase going from 16-25%.

The exposure data for µCD-2 is shown in fig. 32. This sample sheared off during loading and pump down of the vacuum chamber. Due to this, limited surface area was available to be exposed. Therefore the 520, 690, and 870 µA exposures were performed on the same location from lowest current to highest. This means that any sublimation occurring in the 520 or 690 µA exposures will lower the resultant peak temperature for the 820 µA exposure and it cannot be directly compared to the previous samples. No signs of sublimation are observed in the 520 µA run with the peak temperature reaching 1860 K and remaining fairly constant. The percent emission also remained between 18-20%. The 690 µA shows small signs of sublimation with the temperature dropping from 1995 to 1930 K by the end of the run. The percent emission does not show a noticeable increase throughout the run. Noticeable signs of sublimation are observed in the 870 µA exposure, with the peak temperature dropping from 2030 to 1900 K and the percent emission rising from 19-23%. However, the measurements for the 870 µA were affected by the previous runs on this spot and could produce higher shifts in peak temperature and percent emission on a regularly conditioned spot.

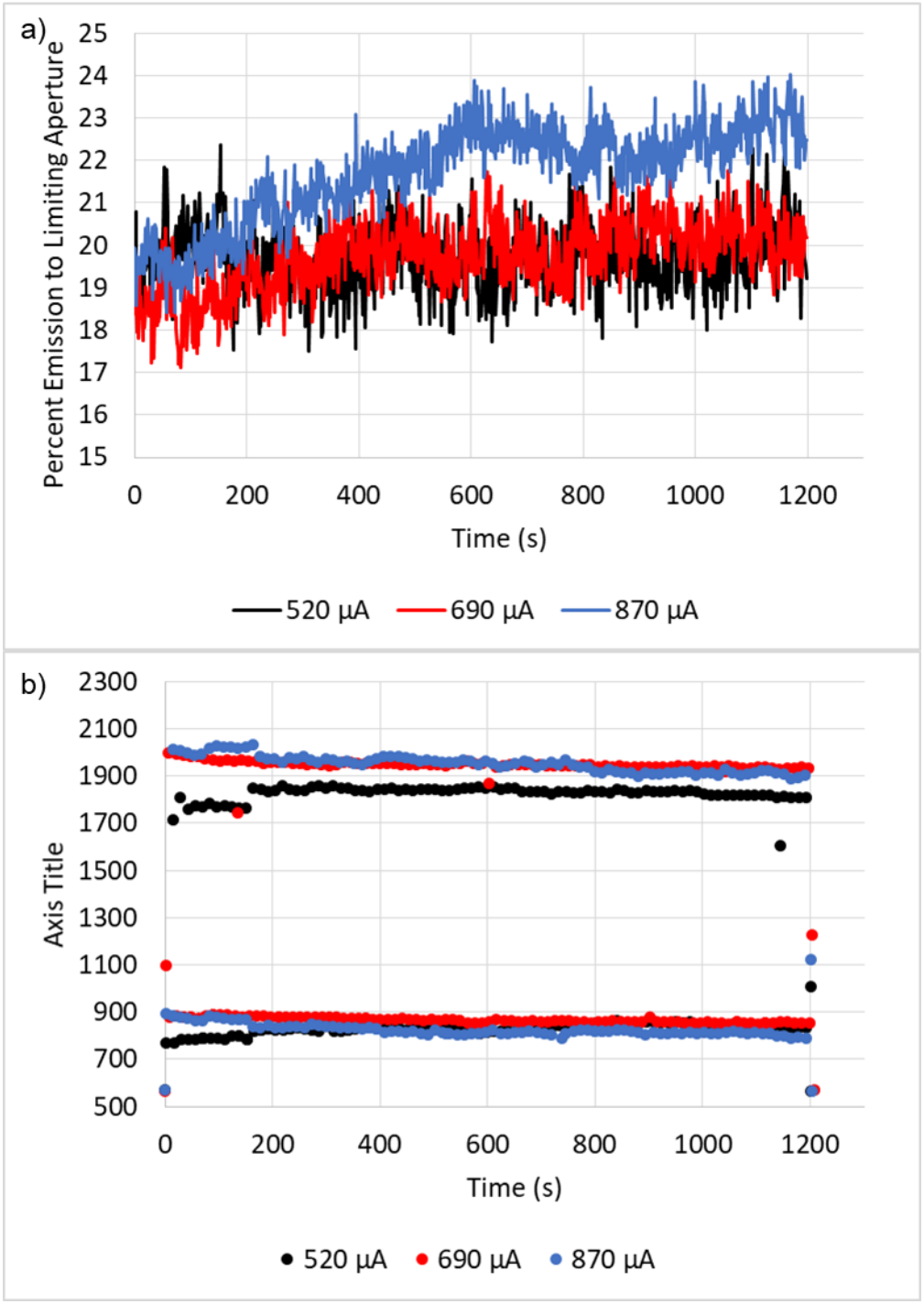


Figure 32 : The µCD-3 samples' Faraday Cup (a) and temperature (b) measurements versus time for the 520, 690, and 870 µA exposed spots.

The beam profile was taken as described above by incrementally moving the foil into the line of the beam. The FTS was vented to atmosphere after the NCD and μCD-1 exposures in order to load μCD-2 and μCD-3 samples. This caused separate measurements to be taken for the μCD-2 and μCD-3 tests. By comparing the experimental data to the Gaussian ring equation we previously determined, a ring radius of 170 μm and a sigma value of 65 μm was determined for the NCD and μCD-1 exposures. Similarly, the μCD-2 and μCD-3 samples were determined to have a beam with a ring radius of 170 μm and a sigma value of 65 μm. It is important to note that this measurement was taken by hand, so the beam profile has intrinsically high error. Additionally, the foils have strong oscillations during this procedure, which creates additional error.

After exposure all samples were tested for their emissivity values with a black body source set at 673, 873, 1073, 1273, and 1473 K to ensure the values remain consistent across multiple temperatures. The emissivity data are plotted in fig. 33. The emissivity values varied slightly and were determined to be on average 0.82, 0.86, 0.84, and 0.86 for the graphitized NCD, μCD-1, μCD-2, and μCD-3 samples, respectively. These values are consistent with other reported graphite and carbon emissivity values [97,98]. The un-graphitized values were determined to be 0.34, 0.47, 0.35, and 0.4 for the NCD, μCD-1, μCD-2, and μCD-3 samples, respectively. These emissivities are important as the FLIR IR camera uses these values to estimate foil temperatures.

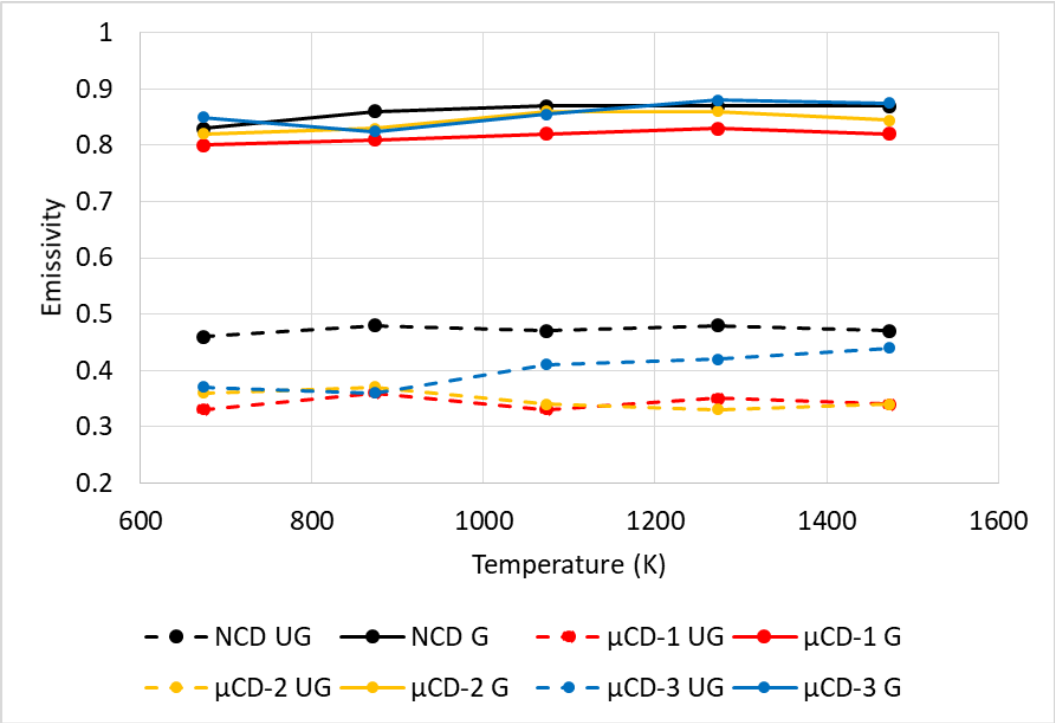


Figure 33 : Emissivity vs Temperature data for the various samples.

The Raman spectra for the graphitized portions of each sample is shown in fig. 34. All of the samples show distinct peaks at 1330, 1590, and 2660 cm^{-1}. The 1330 cm^{-1} peak is attributed to either diamond or disordered graphite. The 1590 cm^{-1} peak is associated with the graphite G peak while the 2660 cm^{-1} peak is the G' band [99]. In the 1590 cm^{-1} peak, a small ledge is observed around 1620 cm^{-1} that corresponds with the D' band in graphite [99]. This suggests that the 1330 cm^{-1} peak corresponds to the D peak in graphite rather than the 1334 cm^{-1} peak associated with diamond. The lack of photoluminescence in the µCD samples suggest the C:H has been reduced during the high temperature graphitization. Additionally, the observed peaks are much narrower in the graphitized sample, suggesting less disorder in the bond structure of the samples. The ratio of D to G peaks in each sample suggest that NCD has the most disordered graphite while µCD-1 has the least.

Scanning Electron Microscope images were taken of all samples. Images of the graphitized and un-graphitized microstructure are shown in figs. 35, 36, 37, and 38 for the NCD, µCD-1, µCD-2, and µCD-3 samples, respectively. The NCD SEM images show small grains on the order of 130 to 150 nm in size. The NCD graphitized sample doesn't exhibit any apparent grain structure and seems to be a more amorphous and porous graphite network. This corresponds well with the higher D to G peak ratio in the graphitized NCD Raman spectra. The µCD-1 film shows larger diamond crystals in the un-graphitized SEM image with grain sizes in the 300 to 400 nm range. The µCD-1 graphitized SEM image also appears to

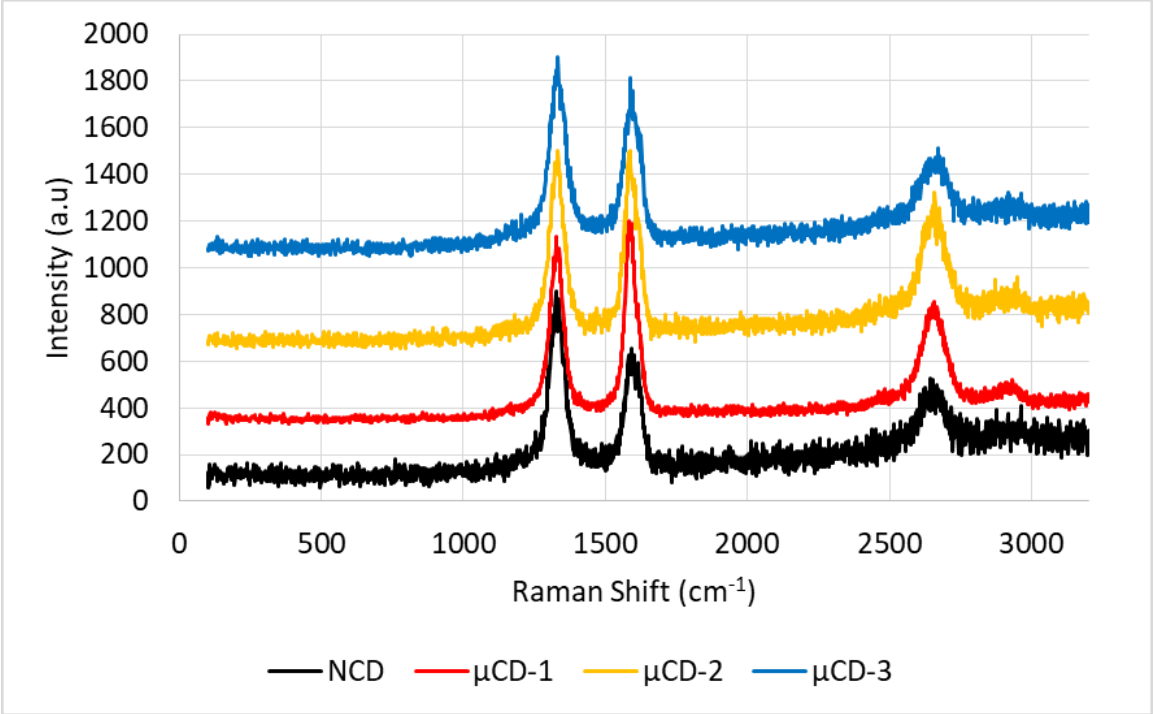


Figure 34: Raman spectra of the graphitized portions of each sample.

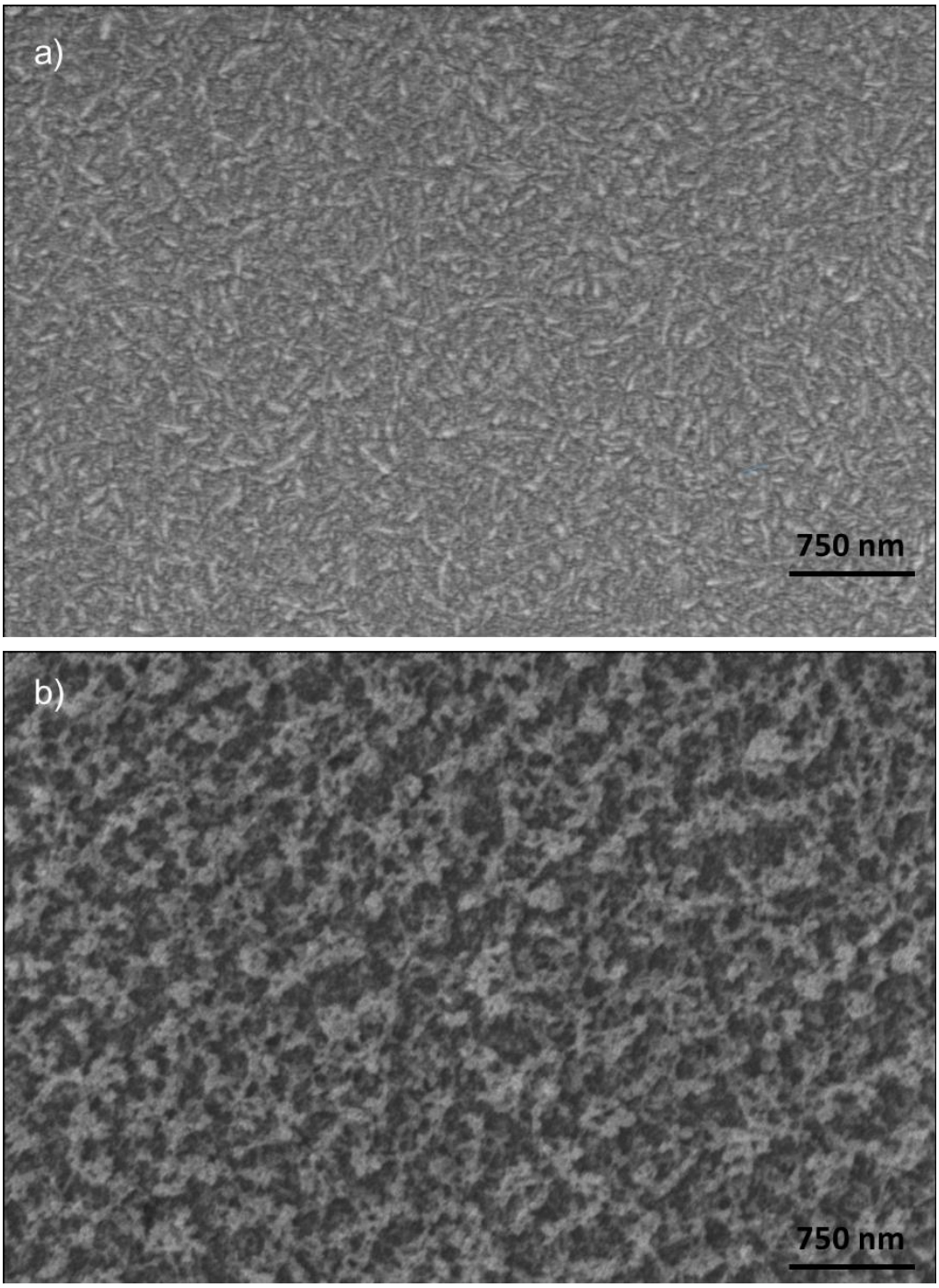


Figure 35: SEM images of the NCD sample's un-graphitized (a) and graphitized (b) regions.

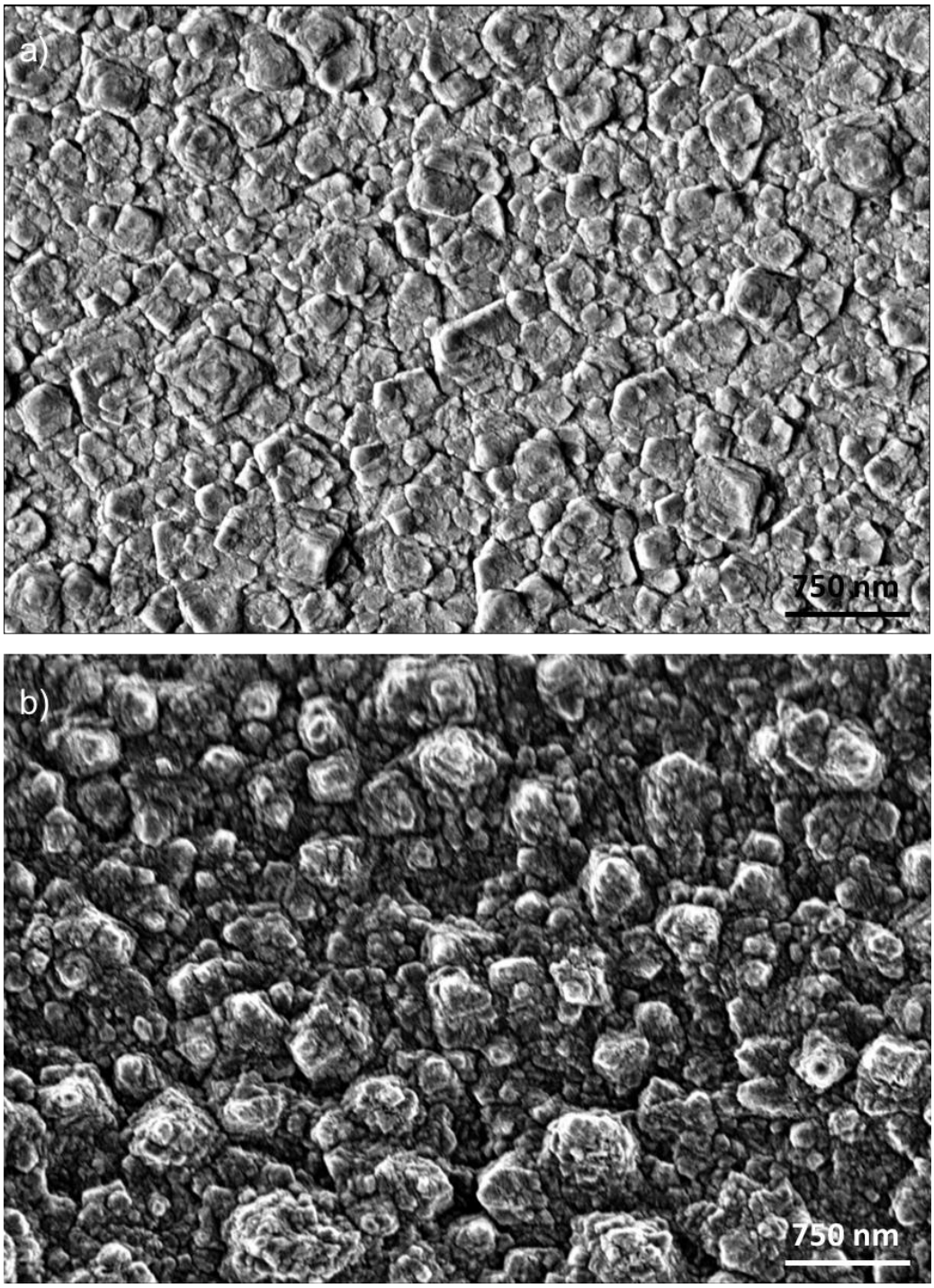


Figure 36: SEM images of the μCD-1 sample's un-graphitized (a) and graphitized (b) regions.

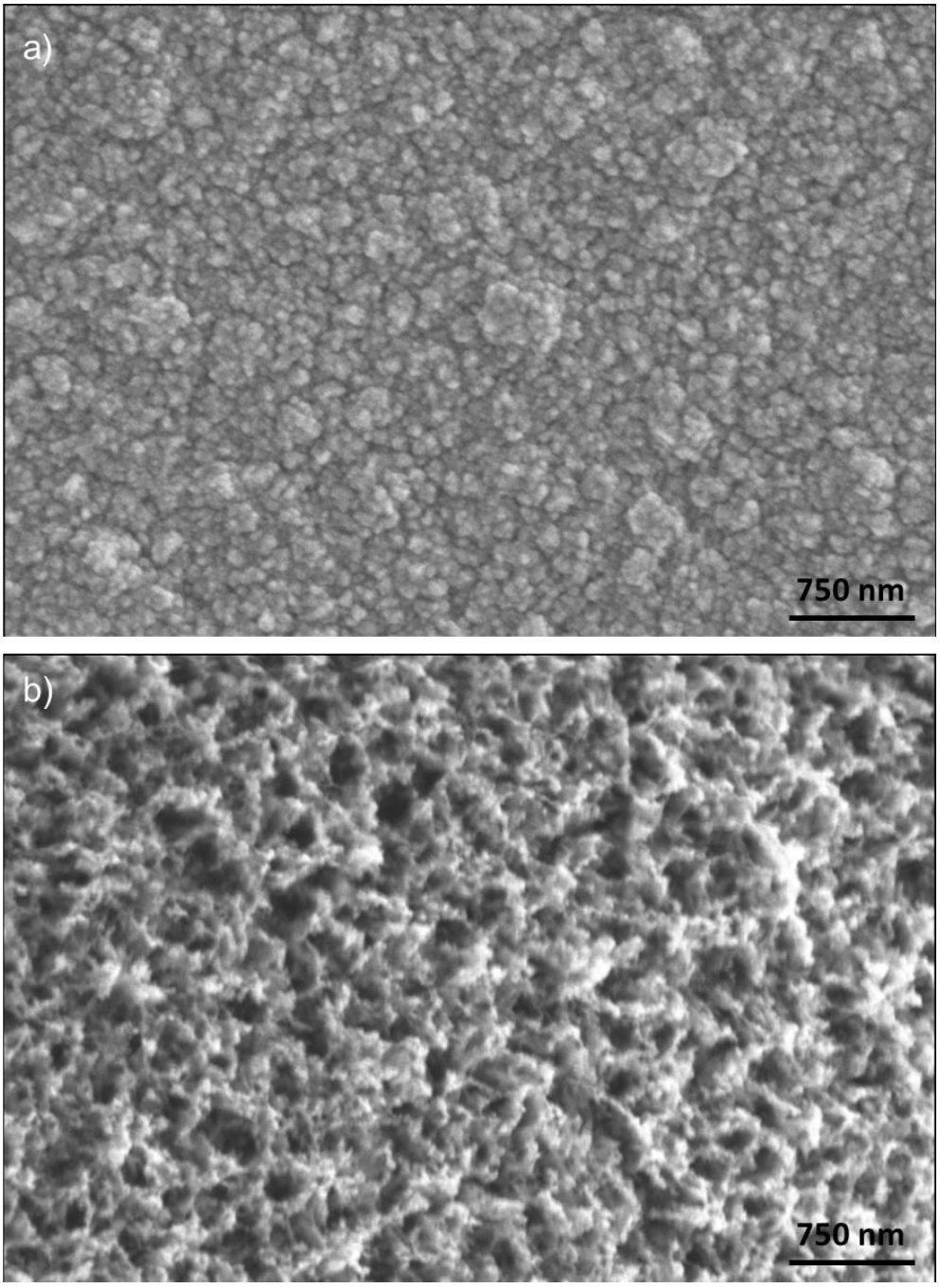


Figure 37: SEM images of the µCD-2 sample's un-graphitized (a) and graphitized (b) regions.

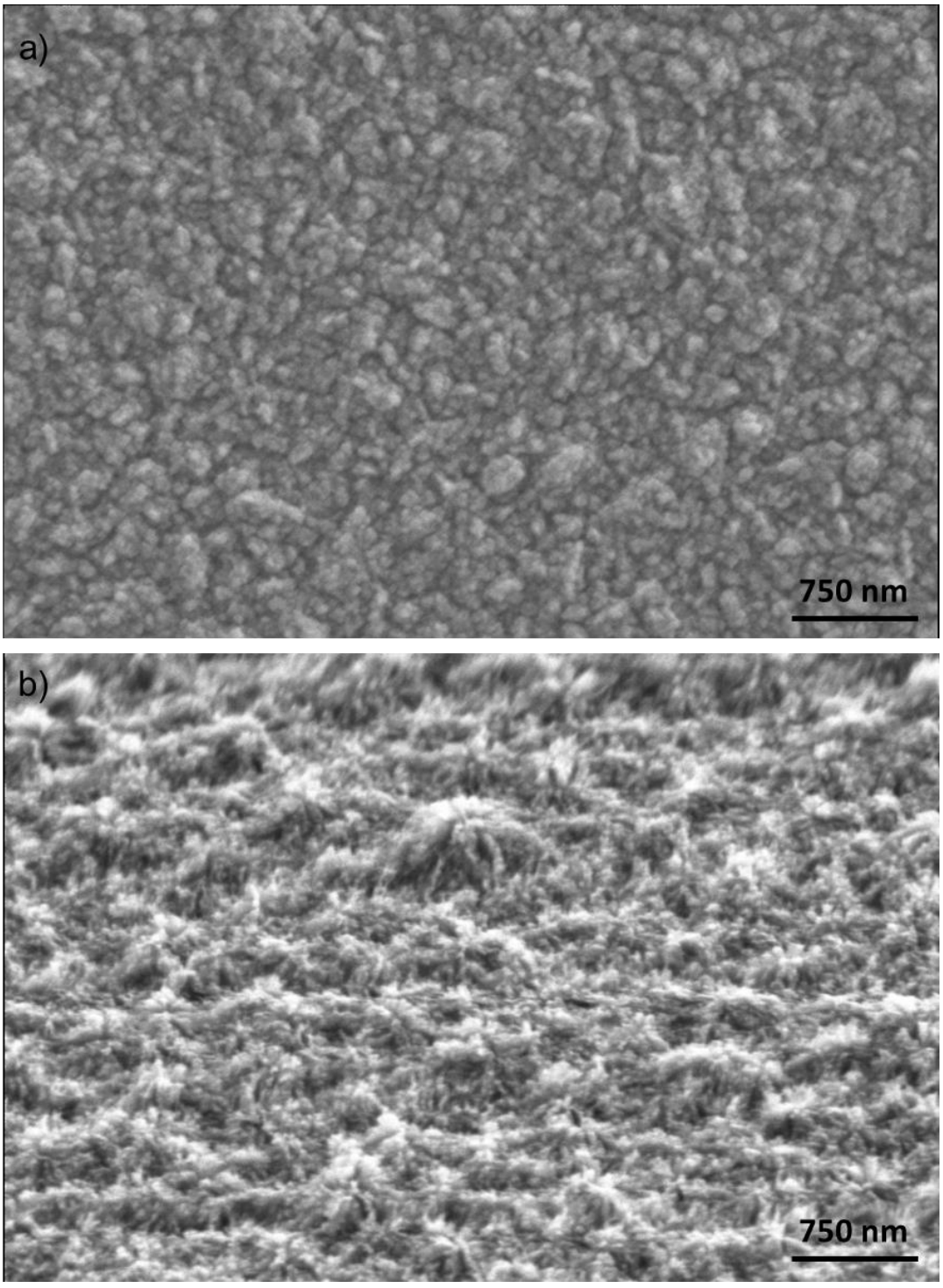


Figure 38: SEM images of the μCD-3 sample's un-graphitized (a) and graphitized (b) regions.

have larger grains with a rougher texture compared to the un- graphitized image. It is also worth mentioning the grain size appears to shift from 300 to 400 nm in the un-graphitized SEM to 400 to 500 nm in the graphitized region. The µCD-2 and µCD-3 samples appear to have largely varying crystallite sizes in the un-graphitized images and a more amorphous rough surface in the graphitized images. The variance in sizes in these un-graphitized SEM images are likely due to the Ar included during growth, which encourages re-nucleation.

COMSOL simulations were performed of the NCD and µCD-1 samples. These two samples were chosen due to NCD being the current SNS foil and µCD-1 having the lowest peak temperature during FTS exposures. For the NCD simulation, the material and simulation parameters were used from a previous study [68]. The graphitized µCD was modeled after POCO graphite's thermal conductivity and specific heat [81]. In order to see the effect of graphitization on near room temperature thermal conductivity, 120 µA pulsed runs were performed on the NCD and µCD-1 samples on graphitized and un-graphitized areas. The NCD diamond sample had a peak temperature of 775 K and 1011 K for the un-graphitized and graphitized portions respectively. For the µCD sample, the peak temperature goes from 428 K on the un-graphitized are to 654 K on the graphitized area. This suggests that for both samples graphitization lowers the thermal conductivity of the sample in a lower temperature regime, resulting in a higher peak temperature for graphitized regions.

Continuous wave beam irradiations were used for NCD and µCD-1 in order to match the COMSOL simulations to the experimental data. A 200 µA CW beam was used to get experimental data for the COMSOL matching, the resultant experimental and simulated data is presented in fig. 39. The NCD sample simulation matches well with the ramp up curve having small deviations from the experimental. The steady state temperature does diverge between the experimental and simulation, however, that should have minimal effect on the pulsed simulations as there will only be 1 ms of beam exposure for each pulse. The µCD-1 data does not match as well as the NCD, with noticeable divergence in the ramp up period. Potential causes for this are mismatch between the simulated thermal conductivity or specific heat and the actual values. For both samples an ε of .8 was found to give the best results.

NCD pulsed simulated and experimental peak temperatures are displayed in fig. 40. The 520 µA simulation and experimental data match very well with the simulation showing a peak temperature of 1842 K which is close to the experimentally observed peak temperature of 1854 K. The 870 µA simulation predicts a peak temperature of 2548 K which is significantly higher than the observed peak temperature of 2119 K. This difference is attributed to the sublimation occurring in the experimental portion that in not accounted for in the simulation.

The µCD-1 pulsed simulated and experimental data are shown in fig. 41. For the 520 µA beam the simulation has a peak temperature of 1678 K, relatively

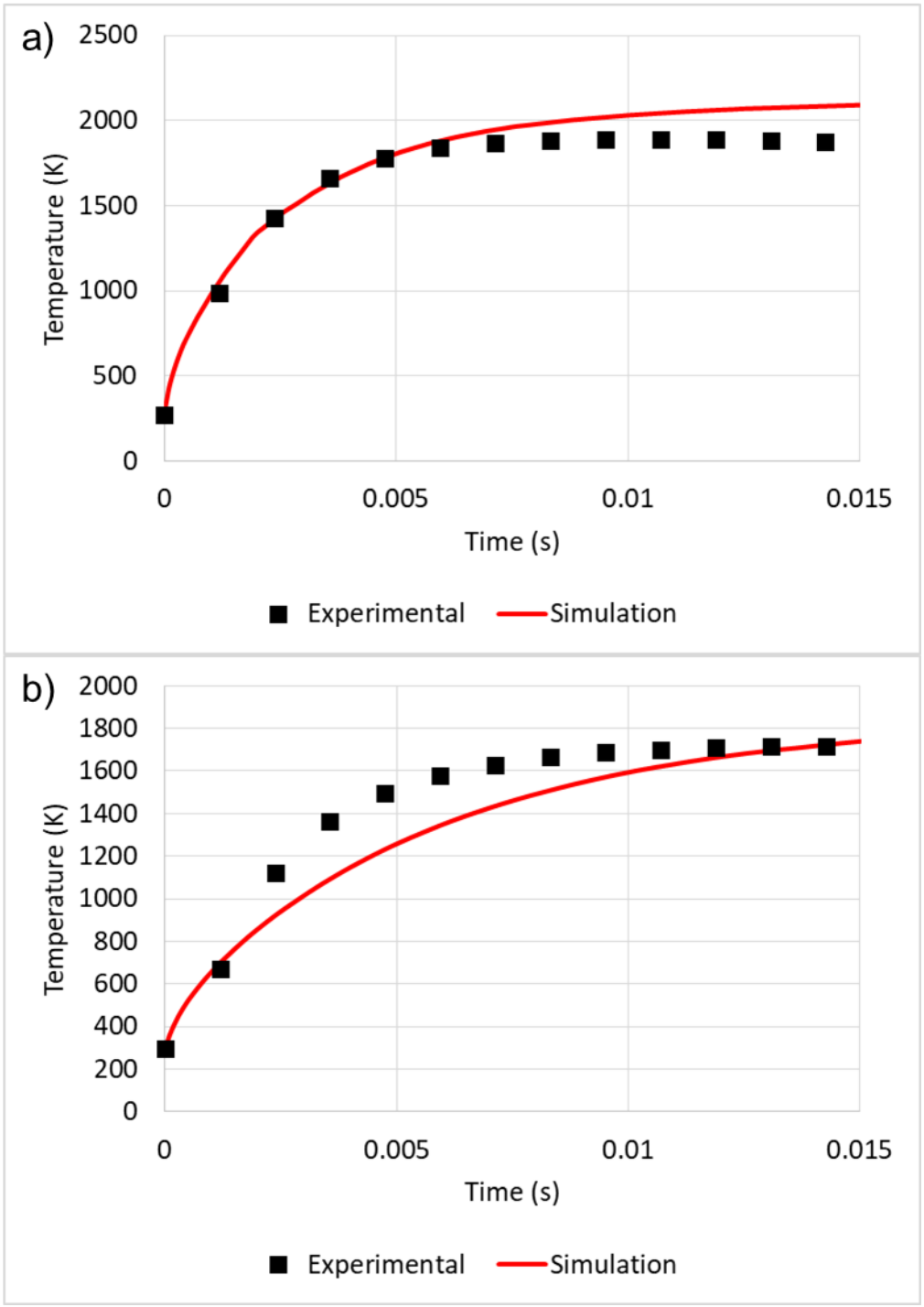


Figure 39: Continuous wave 200 µA experimental and simulated curves for NCD (a) and µCD-1 (b).

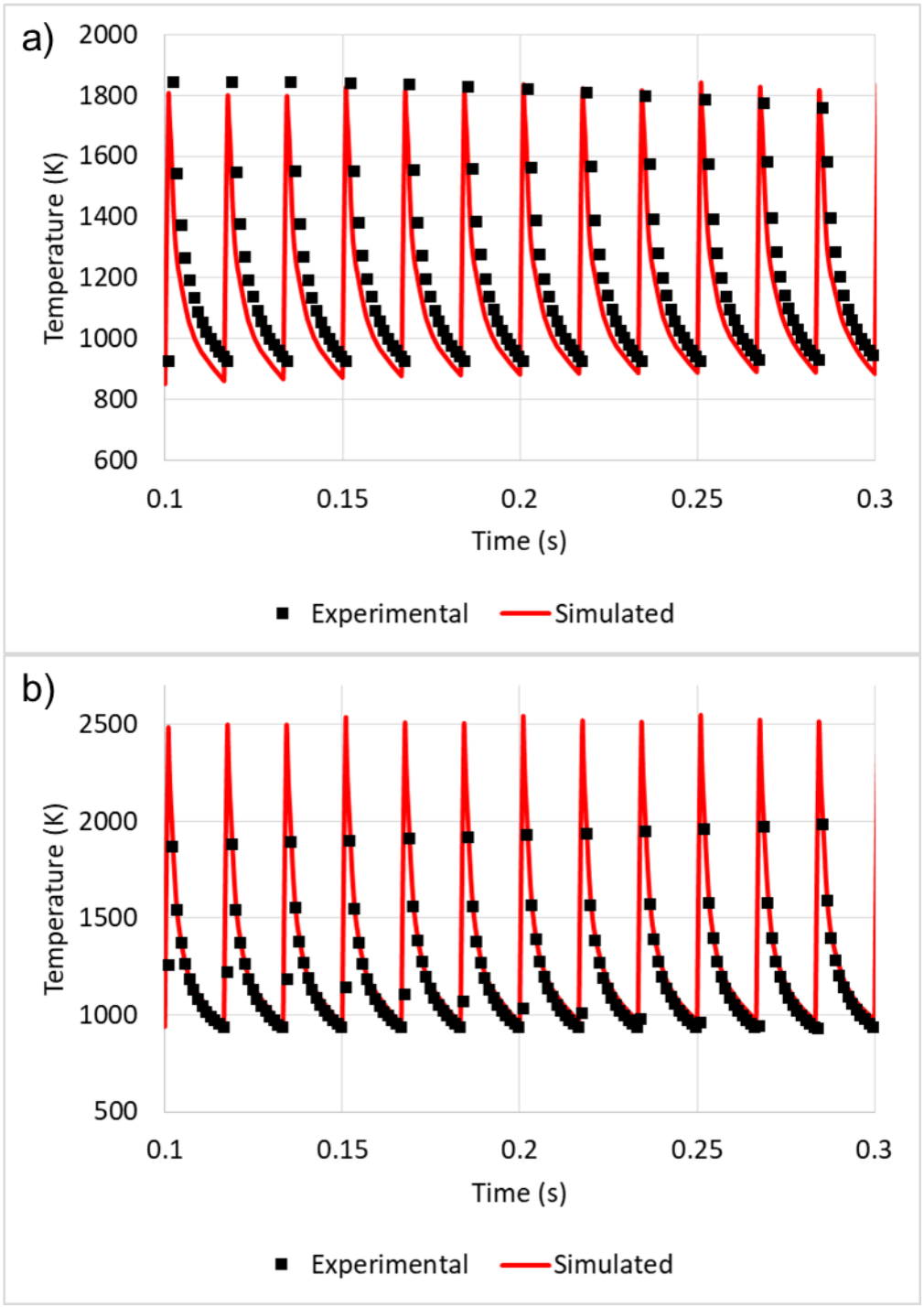


Figure 40: NCD experimental and simulated temperature vs time for 520 μA (a) and 870 μA (b) electron beams.

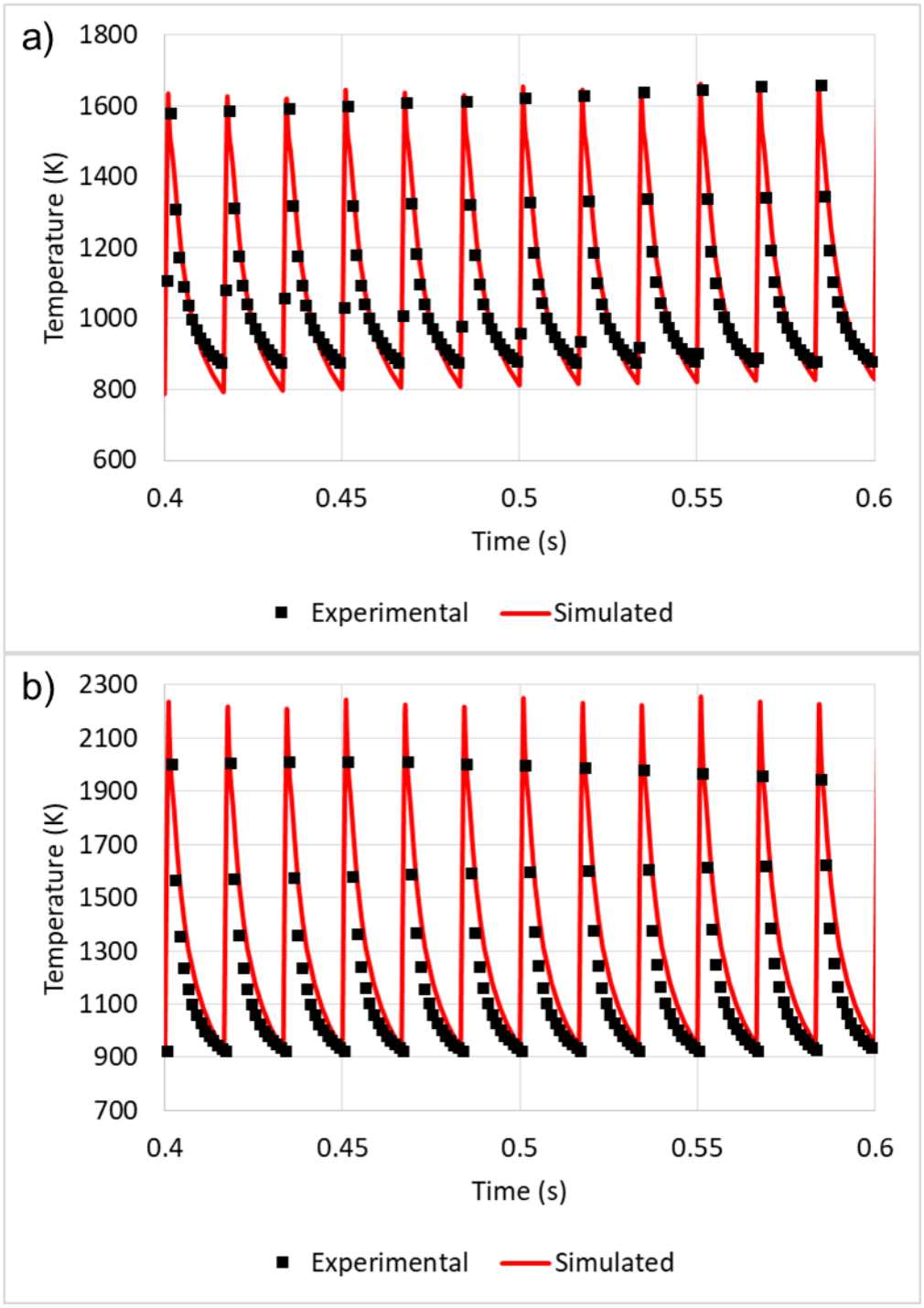


Figure 41: μCD-1 experimental and simulated temperature vs time for 520 μA (a) and 870 μA (b) electron beams.

close to the experimentally observed peak temperature of 1707 K. The 870 μA simulation shows a peak temperature of 2270 K which is significantly higher than the observed 2020 K. This difference is again attributed to sublimation occurring in the sample for which the simulation doesn't account. COMSOL simulations can act as another indicator of sublimation when multiple beam and material parameters are known.

Conclusion

In this study multiple polycrystalline diamond films were irradiated using an electron beam to mimic the energy deposition in the SNS beam line. Four different samples were tested under similar beam conditions and compared with each other to test their relative thermal robustness. Of the four samples, one was the standard SNS NCD recipe, the other 3 recipes were various forms of MPCVD grown μCD foils differing in the proportion of Ar, H_2, CH_4, pressure, and power used during growth. We expect the differing growth parameters to influence the size of the diamond grains in addition to the composition of their grain boundaries. The μCD-1 foil showed considerably lower temperatures when exposed to the same beam as the other foils and is expected to handle a higher beam density than the other foils before sublimation occurs. Postmortem testing was also conducted in order to obtain Raman spectra, SEM imaging, and emissivity measurements for both the graphitized and un-graphitized section of each sample. Lastly COMSOL simulations were performed for NCD and μCD-1 and compared to experimental data. The results of this experiment suggest that

μCD-1 is more thermally robust when compared to the other tested foils. Further testing of the mechanical stability of these foils could be pertinent to determining the overall relative suitability of these foils for charge exchange injection purposes.

Acknowledgements

This work was supported by the DOE office of Science User Facilities. LS, LW, and NE are supported through funding for the Spallation Neutron Source. SNS is managed by UT-Battelle, LLC, under contract DE- AC05-00OR22725 for the U.S. Department of Energy. Foil synthesis, certain post-mortem testing, and modeling were conducted at the Center for Nanophase Materials Sciences, which is also a DOE Office of Science User Facility.

REFERENCES

[1] R.B. Saethre, M.A. Plum, SNS PROTON POWER UPGRADE REQUIREMENTS FOR MAGNET AND KICKER SYSTEMS, in: IEEE 21st Int. Conf. Pulsed Power, IEEE, Brighton, UK, 2017. https://doi.org/10.1109/PPC.2017.8291208.
[2] M. Howell, B. Degraff, J. Galambos, S. Kim, SNS proton power upgrade, IOP Conf. Ser. Mater. Sci. Eng. 278 (2017). https://doi.org/10.1088/1757-899X/278/1/012185.
[3] C. Hojvat, M. Joy, R. Webber, Stripping Foils for Multiturn Charge Exchange, IEEE Trans. Nucl. Sci. NS-26 (1979) 4009–4011.
[4] G.I. Dimov, Use of hydrogen negative ions in particle accelerators, Rev. Sci. Instrum. 67 (1996) 3393–3404. https://doi.org/10.1063/1.1147513.
[5] H. V. Smith, D.J. Adams, B. Jones, C.M. Warsop, Stripping foil simulations for ISIS injection upgrades, IPAC 2011 - 2nd Int. Part. Accel. Conf. (2011) 3556–3558.
[6] I. Pavlovsky, R.L. Fink, Graphene stripper foils, J. Vac. Sci. Technol. B, Nanotechnol. Microelectron. Mater. Process. Meas. Phenom. 30 (2012) 03D106. https://doi.org/10.1116/1.3693594.
[7] M.A. Plum, J. Holmes, R.W. Shaw, C.S. Feigerle, SNS stripper foil development program, Nucl. Instruments Methods Phys. Res. Sect. A Accel. Spectrometers, Detect. Assoc. Equip. 590 (2008) 43–46. https://doi.org/10.1016/j.nima.2008.02.065.
[8] H. Imao, H. Okuno, H. Kuboki, S. Yokouchi, N. Fukunishi, O. Kamigaito, H. Hasebe, T. Watanabe, Y. Watanabe, M. Kase, Y. Yano, Charge stripping of U238 ion beam by helium gas stripper, Phys. Rev. Spec. Top. - Accel. Beams. 15 (2012) 1–9. https://doi.org/10.1103/PhysRevSTAB.15.123501.
[9] F. Marti, P. Guetschow, E. Lansing, Y. Momozaki, J.A. Nolen, C.B. Reed, DEVELOPMENT OF A LIQUID LITHIUM CHARGE STRIPPER FOR FRIB*, in: Heavy Ion Accel. Technol., Yokohama, 2015: pp. 134–138.
[10] V. Danilov, S. Aleksandrov, S. Assadi, W. Blokland, S. Cousineau, C. Deibele, W. Grice, S. Henderson, J. Holmes, Y. Liu, M. Plum, A. Shishlo, A. Webster, I.N. Nesterenko, L. Waxer, Laser stripping of H- beams: Theory and experiments, Proc. IEEE Part. Accel. Conf. (2007) 2582–2586. https://doi.org/10.1109/PAC.2007.4440732.
[11] R.B. Simon, J. Anaya, F. Faili, R. Balmer, G.T. Williams, D.J. Twitchen, D.M. Kuball, Effect of grain size of polycrystalline diamond on its heat spreading properties, Appl. Phys. Express. 9 (2016). https://doi.org/10.7567/APEX.9.061302.
[12] C.E. Nebel, C.R. Miskys, J. a Garrido, M. Hermann, O. Ambacher, M. Eickhoff, M. Stutzmann, Structure and properties of high-temperature annealed CVD diamond, Diam. Relat. Mater. 12 (2003) 1873–1876. https://doi.org/10.1016/S0925-9635.
[13] N. Nunn, M. Torelli, G. McGuire, O. Shenderova, Nanodiamond: A high impact nanomaterial, Curr. Opin. Solid State Mater. Sci. 21 (2017) 1–9. https://doi.org/10.1016/j.cossms.2016.06.008.

[14] S. Kumar, M. Nehra, D. Kedia, N. Dilbaghi, K. Tankeshwar, K.H. Kim, Nanodiamonds: Emerging face of future nanotechnology, Carbon N. Y. 143 (2019) 678–699. https://doi.org/10.1016/j.carbon.2018.11.060.
[15] V. V. Danilenko, On the history of the discovery of nanodiamond synthesis, Phys. Solid State. 46 (2004) 595–599. https://doi.org/10.1134/1.1711431.
[16] O. Auciello, D.M. Aslam, Review on advances in microcrystalline, nanocrystalline and ultrananocrystalline diamond films-based micro/nano-electromechanical systems technologies, J. Mater. Sci. 56 (2021) 7171–7230. https://doi.org/10.1007/s10853-020-05699-9.
[17] Y.A. Mankelevich, P.W. May, New insights into the mechanism of CVD diamond growth: Single crystal diamond in MW PECVD reactors, Diam. Relat. Mater. 17 (2008) 1021–1028. https://doi.org/10.1016/j.diamond.2008.03.022.
[18] M. Mohr, L. Daccache, S. Horvat, K. Brühne, T. Jacob, H.J. Fecht, Influence of grain boundaries on elasticity and thermal conductivity of nanocrystalline diamond films, Acta Mater. 122 (2017) 92–98. https://doi.org/10.1016/j.actamat.2016.09.042.
[19] W.S. Huang, D.T. Tran, J. Asmussen, T.A. Grotjohn, D. Reinhard, Synthesis of thick, uniform, smooth ultrananocrystalline diamond films by microwave plasma-assisted chemical vapor deposition, Diam. Relat. Mater. 15 (2006) 341–344. https://doi.org/10.1016/j.diamond.2005.09.027.
[20] D. Zhou, D.M. Gruen, L.C. Qin, T.G. McCauley, A.R. Krauss, Control of diamond film microstructure by Ar additions to CH4/H2 microwave plasmas, J. Appl. Phys. 84 (1998) 1981–1989. https://doi.org/10.1063/1.368331.
[21] H. Yoshikawa, C. Morel, Y. Koga, Synthesis of nanocrystalline diamond films using microwave plasma CVD, Diam. Relat. Mater. 10 (2001) 1588–1591. https://doi.org/10.1016/S0925-9635(01)00414-9.
[22] M. Miyake, A. Ogino, M. Nagatsu, Characteristics of nano-crystalline diamond films prepared in Ar/H2/CH4 microwave plasma, Thin Solid Films. 515 (2007) 4258–4261. https://doi.org/10.1016/j.tsf.2006.02.048.
[23] R. Abbaschian, H. Zhu, C. Clarke, High pressure-high temperature growth of diamond crystals using split sphere apparatus, Diam. Relat. Mater. 14 (2005) 1916–1919. https://doi.org/10.1016/j.diamond.2005.09.007.
[24] Y. Hu, O.A. Shenderova, Z. Hu, C.W. Padgett, D.W. Brenner, Carbon nanostructures for advanced composites, Reports Prog. Phys. 69 (2006) 1847–1895. https://doi.org/10.1088/0034-4885/69/6/R05.
[25] R.S. Balmer, J.R. Brandon, S.L. Clewes, H.K. Dhillon, J.M. Dodson, I. Friel, P.N. Inglis, T.D. Madgwick, M.L. Markham, T.P. Mollart, N. Perkins, G.A. Scarsbrook, D.J. Twitchen, A.J. Whitehead, J.J. Wilman, S.M. Woollard, Chemical vapour deposition synthetic diamond: Materials, technology and applications, J. Phys. Condens. Matter. 21 (2009). https://doi.org/10.1088/0953-8984/21/36/364221.
[26] M. Schwander, K. Partes, A review of diamond synthesis by CVD

processes, Diam. Relat. Mater. 20 (2011) 1287–1301. https://doi.org/10.1016/j.diamond.2011.08.005.
[27] C. Popov, S. Bliznakov, W. Kulisch, Influence of the substrate nature on the properties of nanocrystalline diamond films, Diam. Relat. Mater. 16 (2007) 740–743. https://doi.org/10.1016/j.diamond.2007.01.003.
[28] J.C. Arnault, L. Demuynck, C. Speisser, F. Le Normand, Mechanisms of CVD diamond nucleation and growth on mechanically scratched Si(100) surfaces, Eur. Phys. J. B. 11 (1999) 327–343. https://doi.org/10.1007/s100510050943.
[29] D. Das, R.N. Singh, A review of nucleation, growth and low temperature synthesis of diamond thin films, Int. Mater. Rev. 52 (2007) 29–64. https://doi.org/10.1179/174328007X160245.
[30] G.S. Ristić, Ž.D. Bogdanov, S. Zec, N. Romčević, Z. Dohčević-Mitrović, Š.S. Miljanić, Effect of the substrate material on diamond CVD coating properties, Mater. Chem. Phys. 80 (2003) 529–536. https://doi.org/10.1016/S0254-0584(03)00094-4.
[31] O. Auciello, A. V. Sumant, Status review of the science and technology of ultrananocrystalline diamond (UNCD^{TM}) films and application to multifunctional devices, Diam. Relat. Mater. 19 (2010) 699–718. https://doi.org/10.1016/j.diamond.2010.03.015.
[32] S. Bhattacharyya, O. Auciello, J. Birrell, J.A. Carlisle, L.A. Curtiss, A.N. Goyette, D.M. Gruen, A.R. Krauss, J. Schlueter, A. Sumant, P. Zapol, Synthesis and characterization of highly-conducting nitrogen-doped ultrananocrystalline diamond films, Appl. Phys. Lett. 79 (2001) 1441–1443. https://doi.org/10.1063/1.1400761.
[33] D.M. Gruen, Nanocrystalline Diamond Films, Annu. Rev. Mater. Sci. 29 (1999) 211–259. https://doi.org/10.1146/annurev.matsci.29.1.211.
[34] R.W. Shaw, M.A. Plum, L.L. Wilson, C.F. Luck, A.G. McDermott, Y.J. Chen, R.L. Coleman, D.M. Gardner, C.S. Feigerle, T. Spickermann, M.J. Borden, Diamond stripper foil experience at SNS and PSR, EPAC 2008 - Contrib. to Proc. (2008) 3563–3565.
[35] E.P. Barrowclough, Analysis of primary stripper foils at SNS by an electron beam foil test stand, University of Tennessee, Knoxville, 2017.
[36] J. Filik, J.N. Harvey, N.L. Allan, P.W. May, J.E.P. Dahl, S. Liu, R.M.K. Carlson, Raman spectroscopy of nanocrystalline diamond: An ab initio approach, Phys. Rev. B - Condens. Matter Mater. Phys. 74 (2006) 1–10. https://doi.org/10.1103/PhysRevB.74.035423.
[37] A. V. Khomich, V.G. Ralchenko, A. V. Vlasov, R.A. Khmelnitskiy, I.I. Vlasov, V.I. Konov, Effect of high temperature annealing on optical and thermal properties of CVD diamond, Diam. Relat. Mater. 10 (2001) 546–551. https://doi.org/10.1016/S0925-9635(00)00517-3.
[38] H.B. Chae, K.H. Park, D.J. Seong, J.C. Kim, Y.J. Baik, Thermal conductivity of CVD diamond films, Int. J. Thermophys. 17 (1996) 695–703. https://doi.org/10.1007/BF01441515.

[39] J. Philip, P. Hess, T. Feygelson, J.E. Butler, S. Chattopadhyay, K.H. Chen, L.C. Chen, Elastic, mechanical, and thermal properties of nanocrystalline diamond films, J. Appl. Phys. 93 (2003) 2164–2171. https://doi.org/10.1063/1.1537465.
[40] O.A. Williams, Nanocrystalline diamond, Diam. Relat. Mater. 20 (2011) 621–640. https://doi.org/10.1016/j.diamond.2011.02.015.
[41] A. Sikora, H. Ftouni, J. Richard, C. Hébert, D. Eon, F. Omnès, O. Bourgeois, Highly sensitive thermal conductivity measurements of suspended membranes (SiN and diamond) using a 3ω-Völklein method, Rev. Sci. Instrum. 83 (2012). https://doi.org/10.1063/1.4704086.
[42] W.L. Liu, M. Shamsa, I. Calizo, A.A. Balandin, V. Ralchenko, A. Popovich, A. Saveliev, Thermal conduction in nanocrystalline diamond films: Effects of the grain boundary scattering and nitrogen doping, Appl. Phys. Lett. 89 (2006) 138–140. https://doi.org/10.1063/1.2364130.
[43] A. V. Sukhadolau, E. V. Ivakin, V.G. Ralchenko, A. V. Khomich, A. V. Vlasov, A.F. Popovich, Thermal conductivity of CVD diamond at elevated temperatures, Diam. Relat. Mater. 14 (2005) 589–593. https://doi.org/10.1016/j.diamond.2004.12.002.
[44] E. Jansen, O. Dorsch, E. Obermeier, W. Kulisch, Thermal conductivity measurements on diamond films based on micromechanical devices, Diam. Relat. Mater. 5 (1996) 644–648. https://doi.org/10.1016/0925-9635(95)00404-1.
[45] W.L. Liu, M. Shamsa, I. Calizo, A.A. Balandin, V. Ralchenko, A. Popovich, A. Saveliev, Thermal conduction in nanocrystalline diamond films: Effects of the grain boundary scattering and nitrogen doping, Appl. Phys. Lett. 89 (2006) 1–4. https://doi.org/10.1063/1.2364130.
[46] S.G. Lebedev, A.S. Lebedev, Calculation of the lifetimes of thin stripper targets under bombardment of intense pulsed ions, Phys. Rev. Spec. Top. - Accel. Beams. 11 (2008) 1–7. https://doi.org/10.1103/PhysRevSTAB.11.020401.
[47] Y. Takeda, M. Plum, O. Sns, O. Ridge, THERMAL SIMULATIONS OF CHARGE-EXCHANGE STRIPPER FOILS FOR HIGH-MELTING-POINT MATERIALS, in: IPAC 2013, 2013: pp. 3312–3314.
[48] C.J. Liaw, Y.Y. Lee, J. Alessi, J. Tuozzolo, Calculation of the maximum temperature on the carbon stripping foil of the spallation neutron source, in: IEEE Part. Accel. Conf., 1999: pp. 3300–3302. https://doi.org/10.1109/pac.1999.792283.
[49] A. Rakhman, W. Blokland, Non-contact surface temperature measurements of nanocrystalline diamond foil under intense ion beams, in: M. Strojnik (Ed.), Infrared Remote Sens. Instrum. XXVIII, SPIE, 2020: pp. 77–83. https://doi.org/10.1117/12.2568927.
[50] W. Blokland, N. Evans, C. Luck, A. Rakhman, Injection foil temperature measurements at the SNS accelerator, HB2018 - Proc. 61st ICFA Adv. Beam Dyn. Work. High-Intensity High-Brightness Hadron Beams. (2018)

104–109. https://doi.org/10.18429/JACoW-HB2018-TUP2WE01.
[51] L. Saturday, L. Wilson, S. Retterer, N.J. Evans, D. Briggs, P.D. Rack, N. Lavrik, Thermal conductivity of nano- and micro-crystalline diamond films studied by photothermal excitation of cantilever structures, Diam. Relat. Mater. 113 (2021) 108279. https://doi.org/10.1016/j.diamond.2021.108279.
[52] R.D. Vispute, H.K. Ermer, P. Sinsky, A. Seiser, R.W. Shaw, L.L. Wilson, G. Harris, F. Piazza, Nanodiamond foils for H--stripping to support the Spallation Neutron Source (SNS) and related applications, Mater. Res. Soc. Symp. Proc. 1634 (2014) 19–24. https://doi.org/10.15S7/opl.2014.704.
[53] R.A. Campos, V.J. Trava-Airoldi, O.R. Bagnato, J.R. Moro, E.J. Corat, Development of nanocrystalline diamond windows for application in synchrotron beamlines, Vacuum. 89 (2013) 21–25. https://doi.org/10.1016/j.vacuum.2012.09.007.
[54] V.K. Liechtenstein, T.M. Ivkova, E.D. Olshanski, R. Repnow, J. Levin, R. Hellborg, P. Persson, T. Schenkel, Advances in targetry with thin diamond-like carbon foils, Nucl. Instruments Methods Phys. Res. Sect. A Accel. Spectrometers, Detect. Assoc. Equip. 480 (2002) 185–190. https://doi.org/10.1016/S0168-9002(01)02089-7.
[55] D. Grbovic, N. V. Lavrik, P.G. Datskos, D. Forrai, E. Nelson, J. Devitt, B. McIntyre, Uncooled infrared imaging using bimaterial microcantilever arrays, Appl. Phys. Lett. 89 (2006). https://doi.org/10.1063/1.2337083.
[56] A.R. Krauss, O. Auciello, D.M. Gruen, A. Jayatissa, A. Sumant, Ultrananocrystalline diamond thin films for MEMS and moving mechanical assembly devices, Diam. Relat. Mater. 10 (2001) 1952–1961.
[57] M. Kamo, Y. Sato, S. Matsumoto, N. Setaka, Diamond synthesis from gas phase in microwave plasma, J. Cryst. Growth. 62 (1983) 642–644. https://doi.org/10.1016/0022-0248(83)90411-6.
[58] J.E. Graebner, V.G. Ralchenko, A.A. Smolin, E.D. Obraztsova, K.G. Korotushenko, V.I. Konov, Thermal conductivity of thin diamond films grown from d.c. discharge, Diam. Relat. Mater. 5 (1996) 693–698. https://doi.org/10.1016/0925-9635(95)00370-3.
[59] M.A. Nitti, G. Cicala, R. Brescia, A. Romeo, J.B. Guion, G. Perna, V. Capozzi, Mechanical properties of MWPECVD diamond coatings on Si substrate via nanoindentation, Diam. Relat. Mater. 20 (2011) 221–226. https://doi.org/10.1016/j.diamond.2010.12.002.
[60] D. Grbovic, N. V. Lavrik, S. Rajic, P.G. Datskos, Arrays of SiO2 substrate-free micromechanical uncooled infrared and terahertz detectors, J. Appl. Phys. 104 (2008) 1–7. https://doi.org/10.1063/1.2959574.
[61] M. Toda, N. Inomata, T. Ono, I. Voiculescu, Cantilever beam temperature sensors for biological applications, IEEJ Trans. Electr. Electron. Eng. 12 (2017) 153–160. https://doi.org/10.1002/tee.22360.
[62] J.M. Lugo, A.I. Oliva, Thermal properties of metallic films at room conditions by the heating slope, J. Thermophys. Heat Transf. 30 (2016)

452–460. https://doi.org/10.2514/1.T4605.
[63] C. Moelle, M. Werner, F. Szücs, D. Wittorf, M. Sellschopp, J. Von Borany, H.J. Fecht, C. Johnston, Specific heat of single-, poly- and nanocrystalline diamond, Diam. Relat. Mater. 7 (1998) 499–503. https://doi.org/10.1016/s0925-9635(97)00202-1.
[64] L.C. Nistor, J. Van Landuyt, V.G. Ralchenko, E.D. Obraztsova, A.A. Smolin, Nanocrystalline diamond films: Transmission electron microscopy and Raman spectroscopy characterization, Diam. Relat. Mater. 6 (1997) 159–168. https://doi.org/10.1016/S0925-9635(96)00743-1.
[65] A. Ferrari, J. Robertson, Raman spectroscopy of amorphous, nanostructured, diamond-like carbon, and nanodiamond, Philos. Trans. Math. Phys. Eng. Sci. 362 (2004) 2477–2512.
[66] J. Anaya, S. Rossi, M. Alomari, E. Kohn, L. Tóth, B. Pécz, K.D. Hobart, T.J. Anderson, T.I. Feygelson, B.B. Pate, M. Kuball, Control of the in-plane thermal conductivity of ultra-thin nanocrystalline diamond films through the grain and grain boundary properties, Acta Mater. 103 (2016) 141–152. https://doi.org/10.1016/j.actamat.2015.09.045.
[67] M.A. Plum, S.M. Cousineau, J. Galambos, S.H. Kim, P. Ladd, C.F. Luck, C.C. Peters, Y. Polsky, R.W. Shaw, R.J. MacEk, D. Raparia, Stripper foil failure modes and cures at the Oak Ridge Spallation Neutron Source, Phys. Rev. Spec. Top. - Accel. Beams. 14 (2011) 1–6. https://doi.org/10.1103/PhysRevSTAB.14.030102.
[68] L. Saturday, C. Luck, L. Wilson, J.D. Fowlkes, P.D. Rack, N.J. Evans, Experimental and simulated heating in nanocrystalline diamond charge exchange injection films using an electron beam to mimic SNS conditions, Nucl. Instruments Methods Phys. Res. Sect. A Accel. Spectrometers, Detect. Assoc. Equip. 1027 (2021) 166226. https://doi.org/10.1016/j.nima.2021.166226.
[69] S. Korenev, R. Dishman, A. Yebra, N. Meshcheryakov, I. Smirnov, I. Pavlovsky, R. Fink, Characterization of Graphene Stripper Foils in 11-MeV Cyclotrons, Phys. Procedia. 90 (2017) 369–373. https://doi.org/10.1016/j.phpro.2017.09.034.
[70] J.H. Kim, S.G. Hong, J.W. Kim, Y.G. Choi, Y.S. Kim, Investigation of cyclotron carbon foil lifetime in relation to its thickness, CYCLOTRONS 2013 - Proc. 20th Int. Conf. Cyclotrons Their Appl. (2014) 227–229.
[71] W. Chou, M. Kostin, Z. Tang, Stripping efficiency and lifetime of carbon foils, Nucl. Instruments Methods Phys. Res. Sect. A Accel. Spectrometers, Detect. Assoc. Equip. 590 (2008) 1–12. https://doi.org/10.1016/j.nima.2008.02.060.
[72] E.P. Barrowclough, C.S. Feigerle, C.F. Luck, L.L. Wilson, R.W. Shaw, M.A. Plum, Analysis of primary stripper foils at SNS by an electron beam foil test stand, 6th Int. Part. Accel. Conf. IPAC 2015. (2015) 1230–1233.
[73] P.K. Saha, M. Yoshimoto, S. Hatakeyama, H. Hotchi, H. Harada, F. Tamura, K. Yamamoto, Y. Yamazaki, M. Kinsho, Y. Irie, First measurement

and online monitoring of the stripper foil thinning and pinhole formation to achieve a longer foil lifetime in high-intensity accelerators, Phys. Rev. Accel. Beams. 23 (2020) 82801. https://doi.org/10.1103/PhysRevAccelBeams.23.082801.
[74] R.W. Shaw, D.P. Bontrager, L.L. Wilson, O. Ridge, C.S. Feigerle, C.F. Luck, M.A. Plum, S.N. Source, O. Ridge, An Electron Beam Sns Foil Test Stand, in: Part. Accel. Conf., 2009: pp. 1638–1640.
[75] A. Shishlo, S. Cousineau, V. Danilov, J. Galambos, S. Henderson, J. Holmes, M. Plum, O. Ridge, The ORBIT simulation code: Benchmarking and applications, Proc ICAP 2006. (2006) 53–58.
[76] S. Prawer, R.J. Nemanich, Raman spectroscopy of diamond and doped diamond, Philos. Trans. R. Soc. A Math. Phys. Eng. Sci. 362 (2004) 2537–2565. https://doi.org/10.1098/rsta.2004.1451.
[77] J.D. Fowlkes, R. Winkler, B.B. Lewis, M.G. Stanford, H. Plank, P.D. Rack, Simulation-Guided 3D Nanomanufacturing via Focused Electron Beam Induced Deposition, ACS Nano. 10 (2016) 6163–6172. https://doi.org/10.1021/acsnano.6b02108.
[78] D.C. Joy, An introduction to Monte Carlo methods, Scanning Microsc. 5 (1991) 329–337. https://doi.org/10.1016/j.physa.2014.06.014.
[79] M.J. Berger, J.S. Coursey, M.. Zucker, J. Chang, Stopping-Power & Range Tables for Electrons, Protons, and Helium Ions, NIST Stand. Ref. Database 124. (2017). https://doi.org/10.18434/T4NC7P.
[80] COMSOL Multiphysics®, (2021). www.comsol.com.
[81] E.P. Roth, R.D. Watson, M. Moss, W.D. Drotning, Thermophysical Properties of Advanced Carbon Materials For Tokamak Limiters, Albuquerque, New Mextico, 1989.
[82] A.C. Victor, Heat capacity of diamond at high temperatures, J. Chem. Phys. 36 (1962) 1903–1911. https://doi.org/10.1063/1.1701288.
[83] R.R. Reeber, K. Wang, Thermal expansion, molar volume and specific heat of diamond from 0 to 3000K, J. Electron. Mater. 25 (1996) 63–67. https://doi.org/10.1007/BF02666175.
[84] A.A. Balandin, Thermal properties of graphene and nanostructured carbon materials, Nat. Mater. 10 (2011) 569–581. https://doi.org/10.1038/nmat3064.
[85] R. Taylor, K.E. Gilchrist, L.J. Poston, Thermal conductivity of polycrystalline graphite, Carbon N. Y. 6 (1968) 537–544. https://doi.org/10.1016/0008-6223(68)90093-6.
[86] A.J. Bullen, K.E. O'Hara, D.G. Cahill, O. Monteiro, A. Von Keudell, Thermal conductivity of amorphous carbon thin films, J. Appl. Phys. 88 (2000) 6317–6320. https://doi.org/10.1063/1.1314301.
[87] K. Bogdanov, A. Fedorov, V. Osipov, T. Enoki, K. Takai, T. Hayashi, V. Ermakov, S. Moshkalev, A. Baranov, Annealing-induced structural changes of carbon onions: High-resolution transmission electron microscopy and Raman studies, Carbon N. Y. 73 (2014) 78–86.

https://doi.org/10.1016/j.carbon.2014.02.041.
[88] G. Gouadec, P. Colomban, Raman Spectroscopy of nanomaterials: How spectra relate to disorder, particle size and mechanical properties, Prog. Cryst. Growth Charact. Mater. 53 (2007) 1–56. https://doi.org/10.1016/j.pcrysgrow.2007.01.001.
[89] J. Park, K. Bae, T.R. Kim, C. Perez, A. Sood, M. Asheghi, K. Goodson, W. Park, Direct Quantification of Heat Generation Due to Inelastic Scattering of Electrons Using a Nanocalorimeter, Adv. Sci. 8 (2021). https://doi.org/https://doi.org/10.1002/advs.202002876.
[90] P. Goldfinger, The vapor pressure and heat of sublimation of carbon, Symp. Combust. Flame Explos. Phenom. 3 (1948) 618–620. https://doi.org/10.1016/S1062-2896(49)80084-5.
[91] P.K. Saha, M. Yoshimoto, H. Hotchi, H. Harada, K. Okabe, Y. Yamazaki, M. Kinsho, Y. Irie, Measurement of continuous degradation of a stripper foil during ths operation with 300 kW beam power in the 3-GeV RCS of J-PARC, J. Radioanal. Nucl. Chem. 305 (2015) 851–857. https://doi.org/10.1007/s10967-015-4023-7.
[92] H. Hasebe, H. Ryuto, N. Fukunishi, A. Goto, M. Kase, Y. Yano, Polymer coating method developed for carbon stripper foils, Nucl. Instruments Methods Phys. Res. Sect. A Accel. Spectrometers, Detect. Assoc. Equip. 590 (2008) 13–17. https://doi.org/10.1016/j.nima.2008.02.059.
[93] J. Birrell, J.E. Gerbi, O. Auciello, J.M. Gibson, J. Johnson, J.A. Carlisle, Interpretation of the Raman spectra of ultrananocrystalline diamond, Diam. Relat. Mater. 14 (2005) 86–92. https://doi.org/10.1016/j.diamond.2004.07.012.
[94] S. Reich, C. Thomsen, Raman spectroscopy of graphite, Philos. Trans. R. Soc. A Math. Phys. Eng. Sci. 362 (2004) 2271–2288. https://doi.org/10.1098/rsta.2004.1454.
[95] J. Wagner, M. Ramsteiner, C. Wild, P. Koidl, Resonant Raman scattering of amorphous carbon and polycrystalline diamond films, Phys. Rev. B. 40 (1989) 1817–1824. https://doi.org/10.1103/PhysRevB.40.1817.
[96] Muons, G4beamline, (2019). http://www.muonsinternal.com/muons3/G4beamline.
[97] L. Biasetto, M. Manzolaro, A. Andrighetto, Emissivity measurements of opaque gray bodies up to 2000 °c by a dual-frequency pyrometer, Eur. Phys. J. A. 38 (2008) 167–171. https://doi.org/10.1140/epja/i2008-10666-6.
[98] R.J. Thorn, O.C. Simpson, Spectral emissivities of graphite and carbon, J. Appl. Phys. 24 (1953) 633–639. https://doi.org/10.1063/1.1721341.
[99] M.A. Pimenta, G. Dresselhaus, M.S. Dresselhaus, L.G. Cançado, A. Jorio, R. Saito, Studying disorder in graphite-based systems by Raman spectroscopy, Phys. Chem. Chem. Phys. 9 (2007) 1276–1291. https://doi.org/10.1039/b613962k.

CONCLUSION

Throughout this work, different types of PCD foils were grown and examined for their material properties and viability as stripper foils for charge exchange injection. The motivation for this work was to assess the current SNS stripper foil's ability to hold up to the increased beam power, as well synthesize and test potential alternatives. In pursuit of this motivation multiple studies were completed.

The current SNS foil recipe was first tested, along with a μCD sample, for different material parameters. These include their Young's Modulus, thermal conductivity, and density. The primary purpose of this study was to find the baseline, room temperature in-plane thermal conductivity of the foils. A higher thermal conductivity can enhance a stripper foils ability to dissipate heat under a pulsed load. To find the thermal conductivity, the two samples were fabricated into cantilevers using multistep etching processes and coated in a thin layer of gold. These cantilever were then photothermally excited using a laser and deflection curves were taken using a position sensitive detector. Comparing the deflection curves to COMSOL simulations allowed for thermal conductivities of the samples to be extracted. From this, the μCD sample showed a six times higher thermal conductivity than the NCD sample. This suggested the μCD sample should be able to transfer heat throughout the foil faster than the NCD sample.

The second study developed a method to test the NCD foil for failure by mimicking the energy deposited into the foil by the SNS beam with an electron beam. The FTS was used to irradiate the stripper foil with a 30 keV electron beam under various current loads. Data was taken in situ using a FLIR camera, RGA, faraday cup, and high definition camera. By examining the temperature and Faraday cup at increasing currents, it was observed that as the foil thinned throughout a run, the temperature on the foil would decrease and the current that passed through the foil and was collected by the faraday cup increased. These two observations were taken as the primary indicators of foil failure and a value of 5.43 MW was determined for the SNS beam at 1.3 GeV where foil failure was seen. This study was able to determine reliable indicators that can provide in situ testing for foil failure. Additionally, the limit of the current SNS foils were examined and correlations were drawn to the effective SNS beam conditions.

The final study compared the NCD foils against three different types of µCD foils. In this study, the FTS was used to irradiate each foil under the same conditions and compare them to determine which foil is the most thermally stable. Through comparison, the µCD-1 sample was determined to have the lowest peak temperatures of all the samples when exposed to the same beam. Additionally, post mortem was performed to obtain the Raman spectra, emissivity, and SEM images of the exposed and unexposed regions of each foil. This allowed insight into the changes that beam exposure caused in each of the

samples. Lastly, this study included COMSOL simulations for the NCD and µCD-1 samples and compared them to experimental data.

This work examined and developed methods to determine both the material parameters, and the beam density that stripper foils for CEI can withstand. This work will hopefully lead to improved stripper foil lifetimes in high energy beam lines. Additional studies on the mechanical stability of different graphitized foils could also provide insight into potential upgrades for current stripper foils.

VITA

Born on February 15 1992 in Fairbanks, Alaska, Leo Saturday grew up in Clarksville Tennessee. After graduating from Northwest High School, he went on to complete his undergraduate degrees from Austin Peay State University in General Business and Physics. After completing his undergraduate, he went on to pursue graduate school at the University of Tennessee at Knoxville in Materials Science and Engineering.